UNIVERSITY OF CALIFORNIA,
IRVINE

Resolving the end: multi-level regulation of telomere homeostasis

DISSERTATION

submitted in partial satisfaction of the requirements
for the degree of

DOCTOR OF PHILOSOPHY

in Biomedical Sciences

by

Jinqiang Liu

Dissertation Committee:
Associate Professor Feng Qiao, Chair
Professor Peter Kaiser
Professor Suzanne Sandmeyer
Professor Eva Lee
Professor Lan Huang

2017

DEDICATION

To

Linna Wang

my dear wife and only love

who shares the best in her life and accompanies me through the worst storm

and my parents

for their unconditional love and support since the day I were born

TABLE OF CONTENTS

LIST OF FIGURES

CHAPTER 5

CHAPTER 6

LIST OF TABLES

ACKNOWLEDGMENTS

First and foremost I would like to thank my advisor Dr. Feng Qiao. He has been supportive from my first day joined the lab. It is such a privilege for me to have him teach me every single experiment hand by hand and learn how to design project step by step from him. Moreover, his elegant style in presentation and teaching, neat written English, enthusiasm for science and clear logic in project design will be my precious treasure toward future career. Besides these academic advices, Dr. Qiao also helped me a lot adapt to American culture as a senior international scientist. Without those, I can hardly imagine that I would have so many achievements. I sincerely appreciate his guidance and support.

I would like to thank my committee members, Dr. Peter Kaiser, Dr. Suzanne Sandmeyer, Dr. Eva Lee and Dr. Lan Huang, for their kind encouragement and insightful comments toward my Ph.D. training. Without their help and support, I could not progress this far.

I also want to express my appreciation to Member in Qiao lab. I would like to thank Dr. Xichan Hu for his valuable advices and I do enjoy all the discussion with him during the lunch. I also want to thank Betsy Meyers and other undergraduate students for their dedicate help in my projects. In addition, I would like to thank Dr. Jin Kwang Kim, Dr. Hyunik Jun, Dr. Clinton Yu and Dr. Songtao Jia for our fruitful collaboration in projects.

I would like to thank Elsevier for permission to include Chapter 3 of my dissertation, which was originally published in Cell Reports. The text of Chapter 3 is a reprint of the material as it appears in Dissecting Fission Yeast Shelterin Interactions via MICro-MS Links Disruption of Shelterin Bridge to Tumorigenesis. I also thank ELife Sciences Publications, Ltd for permission to include Chapter 4 of my dissertation, which was originally published in Elife. The text of Chapter 4 is a reprint of the material as it appears in Multi-step coordination of telomerase recruitment in fission yeast through two coupled telomere-telomerase interfaces. The co-author listed in this publication directed and supervised research which forms the basis for Chapter 4. Moreover, I would like to thank Elsevier for permission to include Chapter 5 of my dissertation, which was originally published in Molecular Cell. The text of Chapter 5 is a reprint of the material as it appears in Structural Basis for Shelterin Bridge Assembly. The co-author listed in this publication directed and supervised research which forms the basis for Chapter 5.

At last but not least, I would like to thank everyone from the Department of Biological Chemistry, University of California-Irvine for their supports. I am grateful for the financial support from School of Medicine and the Stanley Behrens Family Foundation.

CURRICULUM VITAE

Jinqiang Liu

EDUCATION

- **2012 – 2017** ***University of California, Irvine***
  Ph. D. Student Biological Chemistry
- **2011 – 2012** **Texas A&M University**
  Ph. D. Student Biochemistry and Biophysics
- **2007 - 2011** **Nankai University, China**
  B.S. Biological Science

RESEARCH EXPERINCE

- **08/2012 – 12/2017** Department of Biological Chemistry
  University of California-Irvine
  Graduate Student
  Advisor: Dr. Feng Qiao
- **9/2011 – 08/2012** Department of Biochemistry and Biophysics
  Texas A&M University
  Graduate Student
  Advisor: Dr. Feng Qiao
- **05/2009 – 07/2011** Department of Plant Molecular Biology
  Nankai University, China
  Undergraduate Researcher
  Advisor: Dr. Shuzhen Men

ACADAMIC AWARDS AND FELLOWSHIPS

- School of Medicine Outstanding Student Award, University of California-Irvine, 2016
- Outstanding Undergraduate Student Fellowship, Nankai University, Tianjin, China, 2008-2011
- First price for the Tianjin College Student Biological Skill Competition, Tianjin, China, 2009

Publication

1. Kim J.K.*, **Liu J.***, Hu X., Yu C., Roskamp K., Sankaran B., Huang L., Komives E.A., Qiao F. (2017) Structural Basis for Shelterin Bridge Assembly. **Mol. Cell** *68*:698-714
   *Co-first author
2. Hu X.*, **Liu J.***, Jun H. I. , Qiao F. (2016) Multi-step coordination of telomerase recruitment in fission yeast through two coupled telomere-telomerase interfaces. **Elife**. *5*:e15470

*Co-first author

3. Wang J., Cohen A.L., Letian A., Tadeo X., Moresco J.J., **Liu J.**, Yates J.R. 3rd, Qiao F., Jia S. (2016) The proper connection between shelterin components is required for telomeric heterochromatin assembly. **Genes Dev.** *30*:827-39

4. **Liu J.**, Yu C., Hu X., Kim J.K., Bierma J.C., Jun H.I., Rychnovsky S.D., Huang L., Qiao F. (2015) Dissecting Fission Yeast Shelterin Interactions via MICro-MS Links Disruption of Shelterin Bridge to Tumorigenesis. **Cell Rep.** *12*:2169-80

5. Jun H. I., **Liu J.**, Jeong H., Kim J. K., Qiao F. (2013) Tpz1 Controls a Telomerase-nonextendible Telomeric State and Coordinate Switching to an Extendible State via Ccq1. **Genes Dev.** 27: 1917-1931

6. Tadeo X, Wang J, Kallgren SP, **Liu J,** Reddy BD, Qiao F, Jia S. (2013) Elimination of shelterin components bypasses RNAi for pericentric heterochromatin assembly. **Genes Dev.** 27:2489-99.

TALKS/POSTERS

1. Jun H. I., Jeong H., **Liu J.**, Qiao F. (2013) Shelterin-regulated telomerase nonextendible state is activated by Ccq1 in fission yeast. Cold Spring Harbor Laboratory Meeting on Telomeres & Telomerase, New York, USA
2. **Liu J.**, Jun H. I., Meyers C., Qiao F. (2014) Recognition of budding yeast telomerase RNA by TERT and its role in template boundary definition**.** The Nineteenth Annual Meeting of the RNA society, Québec, Canada
3. Kim J.K., **Liu J.**, Hu X., Jun H. I., Qiao F. (2017) Structural Basis for Telomere Length Regulation by Hierarchical Assembly of Shelterin Bridge. Cold Spring Harbor Laboratory Meeting on Telomeres & Telomerase, New York, USA

ABSTRACT OF THE DISSERTATION

Title: **Resolving the end: multi-level regulation of telomere homeostasis**

By

Jinqiang Liu

Doctor of Philosophy in Biomedical Sciences

University of California, Irvine, 2017

Associate Professor Feng Qiao, Chair

In most eukaryotes, telomeres are the natural chromosome ends that are essentially involved in stable maintenance of chromosomes by facilitating chromosomes end replication and preventing them from degradation or end fusion. Hyper-activated telomere-extension activity, including both upregulation of positive regulators and downregulation of the negative regulators, potentially leads to uncontrolled proliferation that is required in cancer cells; inversely, degenerative disorders and premature aging are often accompanied with impaired or lost telomere extension. Similar to human, in fission yeast *Schizosaccharomyces pombe*, telomere structure is achieved by association of shelterin with both double-stranded and single-stranded telomeric DNA forming a nucleoprotein complex. Despite vital roles of shelterin components and telomere structure in telomere length regulation, structural characterizations of assembly and disassembly of shelterin are still limited, which in turn impedes our understanding of the mechanism in which the telomere length homeostasis is maintained.

To this end, we solved the crystal structure of the core part of fission yeast shelterin that reveals essential atomic-level information for cooperative assembly of shelterin bridge. Intriguingly, this cooperativity is also utilized in the human shelterin counterparts, suggesting a highly conserved driving force for shelterin formation. Moreover, this hierarchical formation not only exists within shelterin components, but also occurs in telomerase recruitment to telomere via a bivalent binding event between shelterin and telomerase.

CHAPTER 1

INTRODUCTION

Chromosome integrity and telomere

The genetic materials used for the majority of organisms are DNA molecules that contain most or all genes, termed as chromosome. In the process of heritage of life, the very first and most essential step is DNA replication. The discoveries of DNA structure (Watson and Crick, 1953) and DNA polymerases (Bessman et al., 1958) have significantly broadened our understanding in this biological process; however, another interesting question has also been raised, which is known as "end replication problem" (Figure 1). DNA polymerases are able to synthesize DNA from deoxyribonucleotides, but only in the presence of a short RNA fragment as primer. The replication machinery works fine with most prokaryotes and viruses, since their circular chromosomes don't have an "end". But in Eukaryotic genomes, which are arranged in multiple linear DNA molecules, the gap caused by RNA primer degradation at the very end of chromosomes can't be filled-in by conventional semiconservative DNA replication. Without a feasible solution, the chromosomes would be shortening along the time and eventually result in cell senescence or even death. On the other hand, the physical ends of chromosomes have to be distinguished from DNA double-strand breaks, one of the most deadly types of DNA damage; repairing chromosomes' ends by non-homologous end joining will lead to dicentric chromosomes and eventually cause unbalanced gene distribution and severe genetic disorders (Palm and de Lange, 2008).

Telomere, derived from Greek word "end" + "part", is the natural end of linear

chromosome and serves as the common solution to solve these problems. Telomere consists of a tandem species-specific nucleotide repeats (Blackburn and Gall, 1978). In vertebrates, the sequence is TTAGGG (Moyzis et al., 1988; Meyne et al., 1990); in Ciliated protozoa Tetrahymena, the sequence is TTGGGG (Greider and Blackburn, 1985); budding yeast *Saccharomyces cerevisiae* and fission yeast *Schizosaccharomyces pombe* have a degenerated sequence of G(2-3)(TG)(1-6)T and TTAC(A)(C)G(1-8), respectively (Shampay et al., 1984; McEachern and Blackburn, 1994; Joseph et al., 2007; Murray et al., 1986). Despite the variation of primary sequence and repeat copy numbers, the structure and function of telomeres are highly conserved. Telomeres contain a single-stranded overhang in its G-rich strand (called as G-strand) over the complementary strand (called as C-strand). The single-stranded overhang with 3' -OH group serves as substrate and primer for telomere elongation by telomerase - a reverse transcriptase holoenzyme to counter telomere ablation (Nakamura et al., 1997). Moreover, a protein complex called shelterin binds to the telomeric DNA and induces a higher order architecture formation called T-loop (Griffith et al., 1999), which is suggested a protective role from DNA damage repair by capping the chromosome ends.

Telomerase and its intrinsic RNA components

In most eukaryotes, telomerase is the major source to counter telomere loss, which could directly affect chromosome integrity. Interruption of telomerase assembly or activity would cause severe defects for cell survival and proliferation. As a ribonucleoprotein, telomerase consists of an RNA unit (Telomerase RNA or TER) and a catalytic unit

(Telomerase Reverse Transcriptase or TERT) as the major catalytic core, as well as multiple accessory proteins that serve essential roles in holoenzyme assembly and transportation (Autexier and Lue, 2006; Collins, 2006; Greider and Blackburn, 1985, 1987). During the telomere elongation process, telomerase will repetitively add a short sequence from the template region of TER to telomere.

Intriguingly, the telomerase RNAs vary dramatically in the primary sequence and size from ciliates (~160 nucleotides (nt)), vertebrates (~500 nt) and yeast (above 1000 nt) as the essential component for cell survival; however, TERs from different species shows great conservation in terms of function and domains arrangement. Within decades of extensive study on yeast TER, as well as aided by the structure of ciliate and vertebrate TERs, the structural features with same functions have been revealed in yeast TERs. As one of the most studied non-coding RNA, TER, which is called TLC1 in the budding yeast *S. cerevisiae*, contains three long helical arms tethered to the central core region. Three functional structure elements are located at the distant ends of these three flexible arms, respectively. Each structure element interacts with an accessory protein and has its own role in telomerase function in vivo. One binds to Est1p, which is essential for telomerase recruitment and activation (Seto et al., 2002); another binds to Yku80p, which is important for TLC1 nucleus transportation and Est2p (TERT in S. cerevisiae) recruitment in G1 phase; the third binds to Sm7p, which is dispensable for telomerase activity but important for telomerase assembly via accumulation of TLC1 (Raymund et al., 2012). The flexible arms are not essential for telomerase activity. Previous studies have shown that reposition of the structure elements, or deletion of the flexible arms, would still reconstitute functional telomerase in vivo, or even gain better activity in vitro (Zappulla et al., 2005; Zappulla and

Cech, 2004; Qiao and Cech, 2008).

As another unit of the telomerase catalytic core, Est2p (TERT) was shown to interact with TLC1 central core region (~170 nt) in 2004. However, with more detailed structure-function study, especially aided by two versions of TLC1 miniature - the Mini-T (deletion of the flexible sequence on all three arms) and μT (deletion of all three arms, only central core is retained) (Zappulla and Cech, 2004; Qiao and Cech, 2008), this core region is more complicated than just a reverse transcriptase interaction region. First, a small region is served as the template for reverse transcription. On the flanking region of the template, a stem loop has been shown to act as template boundary region to define the template. Second, a special pseudoknot domain is found in the central core, which functions both structurally and catalytically. In this region, a triple-helix has been identified and has shown the direct participation in catalysis. Third, Est2p can interact with multiple sites including the template boundary region.

Shelterin complex and telomere length homeostasis

Shelterin varies likewise in the protein components from different species. *O. nova* has only two proteins, TEBPα and TEBPβ, to directly bind single-stranded telomeric DNA; *S. cerevisiae* separates the double-stranded (ds) and single-stranded (ss) telomeric DNA binding with Rap1-Rif1-Rif2 complex and Cdc13-Stn1-Ten1 (CST) complex, respectively. On the other hand, human and *S. pombe* share substantial similarities in each individual components and the architecture/structure of whole shelterin complex. The *S. pombe* Taz1 (TRF1/2 in human) and Pot1 (POT1 in human) specifically and avidly bind telomeric

dsDNA and ssDNA, respectively (Palm and de Lange, 2008). A 'protein bridge', consisting of Rap1, Poz1 and Tpz1 in *S. pombe* (TIN2 and TPP1 in human), connects the telomeric dsDNA and ssDNA through their direct protein-protein interaction (Cooper et al., 1997; Baumann and Cech, 2001; de Lange, 2005; Miyoshi et al., 2008). One difference between them is that the shelterin components of *S. pombe* are independently located on telomere, which makes it a better model to investigate how shelterin regulates telomere length homeostasis without the complications caused by dissociation of shelterin components from the telomere due to the loss of interaction (Miyoshi et al., 2008; Jun et al., 2013; Liu te al., 2015). Among the six proteins, Taz1, Rap1 and Poz1 are considered as negative regulator, since deleting any of them leads to unregulated telomere elongation; exactly the opposite applies to the rest three components: perturbation of Tpz1, Pot1 or Ccq1 results in telomere shortening or even a complete loss.

One key role for telomeres is to provide substrate for telomerase-dependent telomere elongation. This nucleotide addition by telomerase is rigorously limited at late S/G2 phase. Moreover, only a small portion of telomeres can be extended in one cell cycle, which is referred to as extendible-state of telomeres and the others as non-extendible state (Teixeira et al., 2004). Recent studies show that the complete linkage, rather than individual components, from telomeric dsDNA and ssDNA mediated by the core of fission yeast shelterin, which is formed by a three-protein complex of Tpz1, Poz1 and Rap1, defines the telomerase-nonextendible state; and Tpz1 is also involved in activating telomeres to extendible state through its interaction with Ccq1 to allow the access of telomerase to telomeres (Jun et al., 2013; Liu te al., 2015). Therefore, a rapid and accurate formation of shelterin is essential for the timely switch between telomere extendible- and

non-extendible- states, which eventually maintains the telomere length homeostasis.

Telomere length and human health

Despite variation in the length of individual telomeres within a cell or an organism, the average telomere length is kept within a narrow species-specific range. In budding yeast and fission yeast, the telomere length is around 300-350 base pair (bp); mouse telomere length can be up to 150 kilobase pair (kb). In human cells, such as stem cells and germ cells, the average telomere length is between 5-15 kb. Disturbation of telomere length homeostasis could cause dramatic cell proliferation defects; therefore, the "telomeropathies" (Holohan et al., 2014) or "telomere syndromes" (Armanios and Blackburn, 2012), which are the genetic diseases that resulted from telomere maintenance disruption, have been continuously identified. Shortly after the discovery of human telomerase, it was shown that about 85% of cancer cells have abnormally increased telomerase activity (Kim et al., 1994; Steward et al., 1996). In addition, recent studies also suggested that mutations on human shelterin complex could be the causative factor in almost 4% familial malignant melanoma cases (Robles-Espinoza et al., 2014). On the other hand, abnormal telomere shortening can reduce the replication capacity of cells and accelerate aging process of the entire organism, which could lead to premature aging disease including dyskeratosis congenital and aplastic anemia. Moreover, in the past few years, it has become evident that an important component of the global pathobiology of heart-related disease lies in the existence of short telomeres (Fitzpatrick et al., 2007, 2011; Fuster and Andres, 2006; Fyhrquist et al., 2011). Older adults with increased levels of

cardiovascular disease risk factors and subclinical cardiovascular diseases have relatively shorter leukocyte telomeres (Saliques et al., 2010; Spyridopoulos and Dimmeler, 2007).

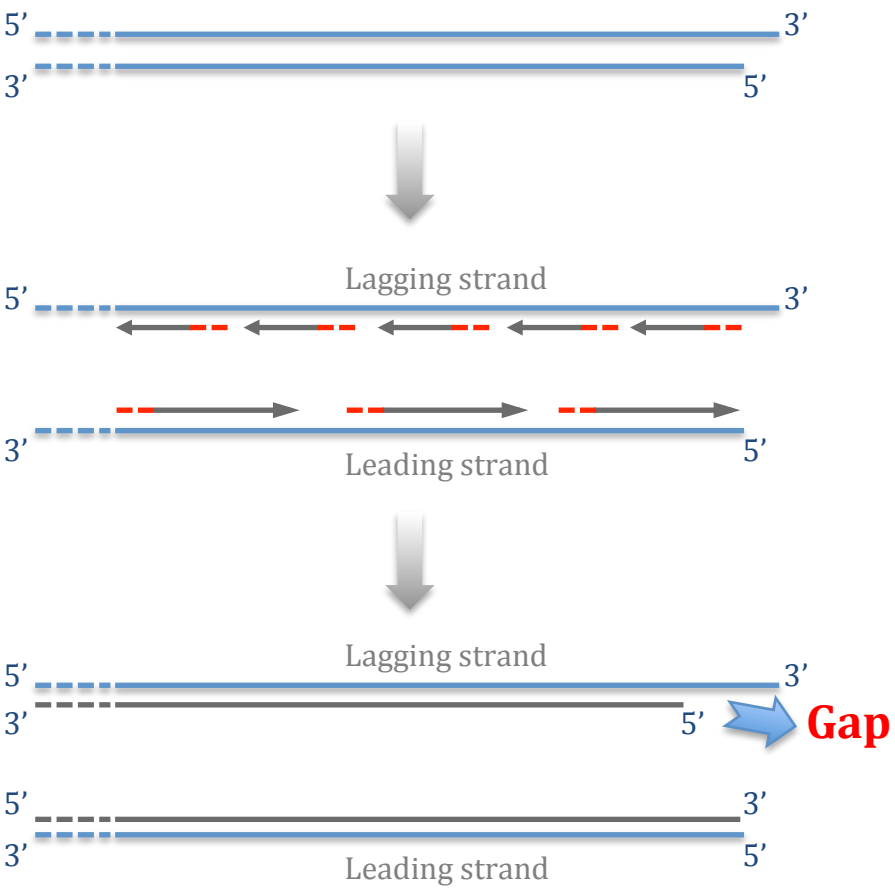

Figure 1. Schematic diagram of DNA "end replication problem". *Top:* Double stranded DNA in linear chromosome. The blue line represents parental DNA. *Middle:* During semiconservative replication of DNA, DNA polymerase requires RNA primer (red dashed line) to initiate DNA elongation (black arrow). Leading strand and lagging strand have different replication pattern. *Bottom:* Newly synthesized DNA (black line) is ligated after RNA primer degradation and gap fill-up. There will be an unfilled gap at 3' end of lagging strand.

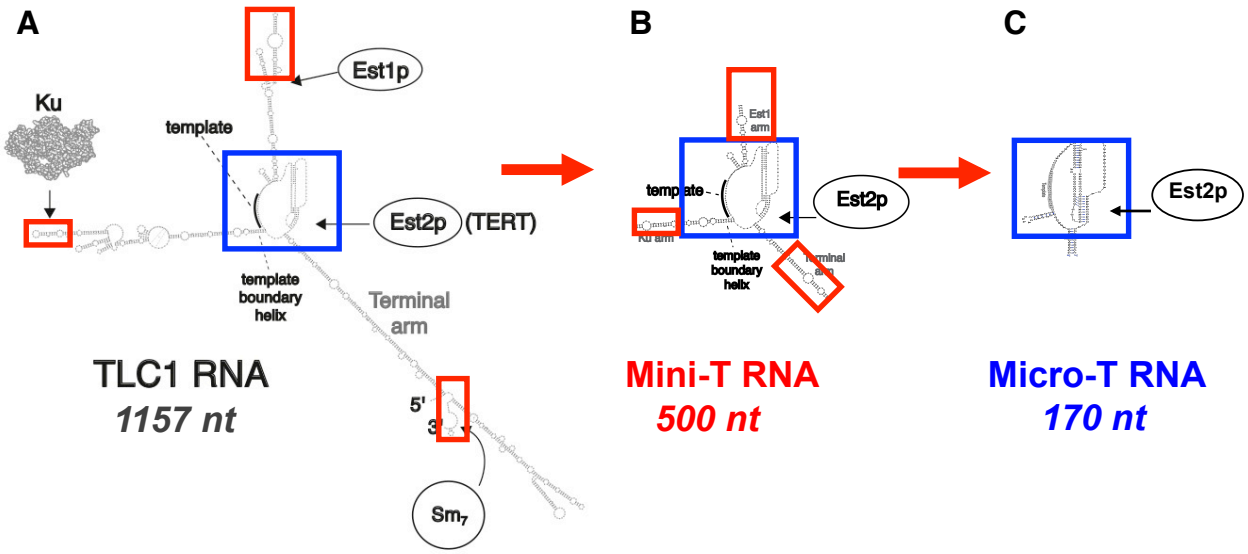

Figure 2. The "beads on the string" model for budding yeast telomerase RNA TLC1. **(A)** 2nd structure prediction of full length TLC1 with functional domain highlighted. **(B)** Mini-T 500 and **(C)** Micro-T 170 are two functional and compact TLC1 constructs for in vitro studies. TLC1 region in blue box represents pseudoknot domain; regions in red box are functional interface for accessory proteins, which are listed in (A). This figure is cited and modified from the paper: Zappulla et al., 2004, PNAS; Zappulla et al., 2005, Nature Structural Molecular Biology; Qiao et al., 2008, Nature Structural Molecular Biology.

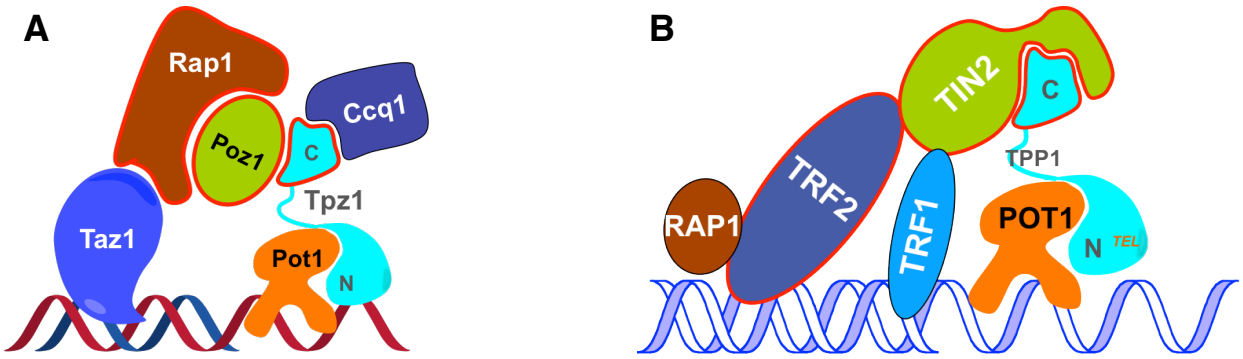

Figure 3. Schematic diagrams of fission yeast *S. pombe* shelterin (A) and human shelterin (B) show great similarity in individual components as well as whole architecture. For clarity, the stoichiometry of each individual component is not indicated in the figure; only one copy of each component is shown.

CHAPTER 2

MATERIALS AND METHODS

Yeast Strains, Gene Tagging, and Mutagenesis

For fission yeast *S. pombe*, single mutant strains were constructed by one-step gene replacement of the entire ORF with the selectable marker. Double and triple mutant strains were produced by mating, sporulation, dissection, and selection followed by PCR verification of genotypes. Genes were fused to specific epitope-tags at the C-terminus by homologous recombination; the pFA6a plasmid modules were used as templates for PCR (Bahler et al., 1998; Sato et al., 2005). Point mutations were made by site-directed mutagenesis PCR using the high fidelity polymerase Pfu (Agilent). All mutations were confirmed by DNA sequencing (Eton, San Diego, CA). The Trt1-Tpz1 fusion strains were constructed based on previously published strains (Armstrong et al., 2014).

For budding yeast *S. cerevisiae*, the RNA mutations were introduced into the CEN plasmids (pRS314) that harbor telomerase RNA TLC1, or the miniature Mini-T (500) through QuikChange Site-Directed Mutagenesis. The plasmids were then transformed into yeast and the colonies that contain RNA mutations were selected out as previous described (Qiao and Cech, 2008). Briefly, after the transformants grew on selective media, the parental plasmid that harbors wild type TLC1 was shuffled out by growing on 5-fluoroorotic acid (5-FOA) plates. As to the dominant negative mutants, the RNA mutations

were introduced into TLC1 or Mini-T (500) on the 2μ plasmids (pRS424). And the transformants were only selected on selective media.

Telomere Length Analysis

For fission yeast *S. pombe*, the telomere length of each strain was analyzed as previously described (Liu et al., 2015). Briefly, genomic DNA was prepared from 5 ml liquid culture in YEAU. For most strains, the telomeric fragments were released by EcoRI (NEB) digestion and separated on 1% agarose gels. Southern blots with both telomeric and *pol1*$^{+}$ probe were visualized using Typhoon scanner (GE Healthcare).

For budding yeast *S. cerevisiae*, the genomic DNA was extracted like fission yeast cells. Then, EcoRI (NEB) digested gDNA was resolved on a 1.2% agarose gel and transferred to Hybond N+ membrane (GE healthcare). The telomeric fragments were visualized with randomly primed radiolabeled telomeric probes and chromosome IV fragment probe.

Co-Immunoprecipitation

Cells were cultured in 50 ml YEAU and harvested till log phase. Cell pellets were cryogenically disrupted with FastPrep MP with two pulses (60 sec) of bead-beating in ice-cold lysis buffer [50 mM HEPES at pH 7.5, 140 mM NaCl, 15 mM EGTA, 15 mM MgCl2, 0.1% NP40, 0.5 mM Na3VO4, 1 U/ml DNase, 1 mM NaF, 2 mM PMSF, 2 mM benzamidine, Complete proteinase inhibitor (Roche)]. Whole cell extract was cleared by centrifugation

twice, 10 min each. Then, the concentration of the supernatant was measured using Bradford protein assay (Bio-Rad) and was adjusted to 12 mg/ml with lysis buffer. 300 µl cell extracts were incubated with anti-Flag M2 affinity gel (Sigma), anti-Myc (9E10 from Santa Cruz Biotechnology) or anti-Ccq1 rabbit serum or anti-Rap1 rabbit serum plus IgG beads (Roche) for 2 h at 4 °C. The proteins were eluted with 30µl 0.1 M glycine (pH2.0) at room temperature for 10 min with gentle shaking followed by Tris-HCl (pH8.0) neutralization. Eluted proteins were resolved by 8% SDS-PAGE and then subjected to Western Blotting. Western blot analysis was performed using monoclonal anti-Flag (M2-F1804, from Sigma), monoclonal anti-Myc (from Covance), anti-Ccq1 rabbit serum (Hu et al., 2016), anti-Rap1 rabbit serum, or anti-Cdc2 (y100.4, from Abcam).

Chromatin immunoprecipitation

Fresh S*. pombe* cells in liquid culture were fixed with 1/10 (vol/vol) ratio of an 11% formaldehyde solution (11% formaldehyde, 100 mM NaCl, 1 mM EDTA at pH 8.0, 0.5 mM EGTA, 50 mM Tris-HCl at pH 8.0) for 20 min, followed by the termination with 125 mM glycine for 5 min. Cell pellets were disrupted in 400 µL of lysis buffer (50 mM Hepes at pH 7.5, 140 mM NaCl, 1 mM EDTA, 1% Trition X-100, 0.1% sodium deoxycholate, Complete proteinase inhibitor [Roche], 1 mM PMSF, 1 mM benzamidine, 1 mM Na3VO4, 1 mM NaF) with FastPrep MP. After three pulse (1 min) of beads-beating, at least 90% cells were broken. Cell extracts were sonicated one time for 30 s in 45 cycles using a Bioruptor (Diagenode). Clarified cell extracts were incubated with anti-Myc resin (9E10, Santa Cruz), anti-Flag M2 affinity gel (Sigma) or anti-Ccq1 rabbit serum followed by protein G-agarose

(Roche, Indianapolis, IN) for 3 hr at 4°C. Then, the beads were washed sequentially, each twice, with lysis buffer, lysis buffer with 500 mM NaCl, wash buffer, and 1x TE buffer. Each sample was added with 100 µl of 10% Chelex100 resin and boiled for 15 min, followed by 20 µg proteinase K treatment for 30 min at 55°C. The recovered DNA were denatured with 0.4 M NaOH and transferred to a Hybond-XL membrane by using a slot module. The blots were hybridized with telomeric probe; the same blot was then re-probed with rDNA probe after stripping off the telomere probe.

Protein expression and purification

Plasmids containing designed protein constructs, either wild type or mutant, were transformed into Rosetta-BL21 (DE3) cells. IPTG was added to log-phase cell culture to induce protein expression. For S. pombe proteins, 0.4 mM IPTG was used and the proteins were expressed for 4 h at 30 °C. for H. sapiens proteins, 0.2 mM IPTG was used and the proteins were expressed overnight at 16 °C. Cells were harvested at 5000 rpm for 10 min and disrupted by sonication in lysis buffer (25mM Tris-HCl at pH 8.0, 350 mM NaCl, 15 mM imidazole, 5 mM β-mercaptoethanol, 1 mM PMSF, 2 mM benzamidine). The supernatant was incubated with Ni-NTA (Qiagen) resin for 1 h. After washing, the bound protein was eluted from the beads with elution buffer containing 300 mM imidazole. Eluted proteins were then cleaved to remove the tag and further purified by ion exchange and/or gel filtration chromatography.

For biotinylated proteins, all target proteins were subcloned into a modified pET28a vector containing the Avi-6His-SUMO tag (Zhao et al., 2016). The biotinylated Avi-6his-

SUMO-proteins were expressed in Rosetta BL21 (DE3), which were co-transformed with the modified pET28a vector (Kanamycin) and the pBirAcm vector containing the BirA gene (Chloramphenicol). Protein expression was induced with 0.4 mM IPTG in presence of 50uM biotin (Oxchem) at 16 °C overnight. The expressed proteins were first purified using Ni-NTA column and further purified using Superdex75, eluted with 20 mM Tris-HCl pH 8.0, 350 mM NaCl.

For *in vitro* protein translation, hPOT1 in a pET28 vector was mutated by site-directed mutagenesis PCR. WT and all mutants were *in vitro* expressed using TnT coupled reticulocyte lysate kit (Promega) following the manual. Briefly, a 25-µl reaction containing 20 µl rabbit reticulocyte lysate, 0.5 µg plasmid, 1 µl 1mM methionine, and 1 µl [35S]methionine was incubated at 30°C for 90 min. 22 µl of each in vitro translation reaction was directly applied to GST pull-down assay, but with 7 µg of GST fusion protein.

GST Pull-Down Assay

GST-pulldown assays were performed after protein purification. Briefly, 15 µg GST fusion protein was incubated with 20 µl glutathione sepharose resin (Qiagen) in 30 µl GST pulldown buffer [50 mM Tris-HCl at pH 8.0, 200 mM NaCl, 10mM b-ME, 0.1% Tween-20]. Then the resin was washed and incubated with the target protein (20 µg in 120 µl GST pulldown buffer) for 1 h. The bound proteins were resolved by 10% SDS-PAGE and visualized by Coomassie blue staining.

Crosslinking Mass Spectrometry Analysis

45 µl purified protein complex (4.5 mg/ml for Tpz1-Ccq1; 4 mg/ml for Tpz1-Poz1; 1.25 mg/ml for Tpz1-Pot1) was mixed with 5 µl DSSO (dissolved in DMSO) to the final concentration as indicated in results. Crosslinking was performed for 30 min and quenched with 2 µl 1 M Tris-HCl (pH 8.0) for 15 min. The cysteine residues were reduced with 4 mM TCEP and alkylated with 20 mM iodoacetamide in dark, followed by terminating alkylation reaction with 20 mM cysteine for 30 min. The crosslinked proteins were digested overnight at 37°C with trypsin (2%, w/w) and chymotrypsin (5%, w/w), separately. Crosslinked peptides were analyzed by LC MS^n utilizing an LTQ-Orbitrap XL MS (Thermo Fisher Scientific) coupled online with an Easy-nLC 1000 (Thermo Fisher Scientific) as described (Kao et al., 2011). Each MS^n experiment consists of one MS scan in FT mode (350–1,400 m/z, resolution of 60,000 at m/z 400) followed by two data-dependent MS2 scans in FT mode (resolution of 7,500) with normalized collision energy at 20% on the top two MS peaks with charges 3+ or up, and three MS3 scans in the LTQ with normalized collision energy at 35% on the top three peaks from each MS2.

Identification of DSSO Crosslinked Peptides by LC-MS^n

MS3 data were subjected to a developmental version of Protein Prospector (v.5.10.10) for database searching, using Batch-Tag with mass tolerances for parent ions and fragment ions set as ±20 ppm and 0.6 Da, respectively. Trypsin was set as the enzyme with five maximum missed cleavages allowed. A maximum of five variable modifications were also allowed, including protein N-terminal acetylation, methionine oxidation, N-

terminal conversion of glutamine to pyroglutamic acid, asparagine deamidation, and cysteine carbamidomethylation. In addition, three defined modifications on uncleaved lysines and free protein N termini were also selected: alkene (A: C3H2O, +54 Da); sulfenic acid (S: C3H4O2S, +104 Da), and unsaturated thiol (T: C3H2OS, +86 Da) modifications, due to remnant moieties of DSSO. Initial acceptance criteria for peptide identification required a reported expectation value ≤0.1.

Integration of MS^n data was carried out using the in-house program LinkHunter, a revised version of the previously written Link-Finder program, to validate and summarize crosslinked peptides as previously described (Kao et al., 2011, 2012).

Crystallization, data collection and structure determination

Initially, crystals of Tpz1$^{475-508}$-Poz1-Rap1$^{470-494}$ complex were grown by hanging drop vapor diffusion at 18°C, with 15∼20% PEG-3350 and 0.175-0.225 M potassium citrate tribasic monohydrate, pH8.3 in the well. To improve the crystal quality, additive screen was carried out. The best crystals were produced with 16-17% PEG-3350, 0.2-0.25 M potassium citrate tribasic monohydrate pH 8.3, with 3% 1,5-Diaminopentane dihydrochloride as an additive. The crystals were stepwise transferred into dehydration solutions with 5% increase of PEG-3350 for each step, up to 35% for 3-8 hr. Dehydrated crystals were then gradually transferred into cryo-protectant solution containing additional 18% glycerol and flash-frozen in liquid nitrogen for data collection under 100K. Diffraction date was collected to 2.5 Å resolution at the ALS beamline 501 and processed using Mosflm (Battye et al.). The crystals belong to space group P212121 with unit cell

parameters of a=83.36, b=95.39, c=109.17 and α=β=γ=90°. Each asymmetric unit contains a dimer of the Tpz1$^{475-508}$-Poz1-Rap1$^{470-494}$ complex. Unfortunately, the Se-Met version of Tpz1$^{475-508}$-Poz1-Rap1$^{470-494}$ is rather insoluble. To overcome this difficulty, we mutated some Met residues in Poz1 to other hydrophobic residues and obtained Se-Met derivative crystals of Tpz1$^{475-508}$-Poz13M-Rap1$^{470-494}$ (Poz13M: M26A, M57L, M62A, M114I, M182A and M243A with only three Met residues left) in a similar condition to the native Tpz1$^{475-508}$-Poz1-Rap1$^{470-494}$ complex. These Se-Met derivative crystals belong to space group P3121 with unit cell parameters of a=b=108.59, c=132.59; α=β=90°, γ=120°. Diffraction data were collected to 3.7 Å resolution at the ALS beamline 821 and processed using Mosflm (Battye et al.). With these Se-Met crystals, we obtained initial phases and initial electron density map using program Phenix (Afonine et al.). We then built a partial model for Tpz1$^{475-508}$-Poz13M-Rap1$^{470-494}$ with mainly backbone traced using Coot (Emsley et al.). The model was then used as a template for for the molecular replacement program to search against the native dataset of Tpz1$^{475-508}$-Poz1-Rap1$^{470-494}$ crystals. The final model for native Tpz1$^{475-508}$-Poz1-Rap1$^{470-494}$ was built and refined using Coot (Emsley et al.) and Phenix (Afonine et al.), respectively (PDB: 5WE2). While most regions of Tpz1 and Poz1 are unambiguously assigned in the model, only 3 to 4 residues of Rap1 were identified in the electron density map. In addition, two flexible loops, spanning residues 73-86 and 117-126, were identified in Poz1 with no clear density.

In order to achieve a higher resolution of the overall structure and distinct electron density map for Rap1, we replaced those two flexible regions with shorter linker sequences (Poz1 73-86 and 117-126 with GGA and GGGSA, respectively) and fused the N-terminus of Rap1 to the C-terminus to Poz1 with a linker sequence G. Crystals from the improved

construct, Tpz1$^{475-508}$-Poz1-Rap1$^{467-496}$, grew and were handled with the same procedure as described above for the native Tpz1$^{475-508}$-Poz1-Rap1$^{470-494}$ complex except for using 1,5-Diaminopentane dihydrochlorideadditive as an additive. The crystals diffracted to 2.3 Å at the ALS beamline 821 and belong to space group P1 with unit cell parameters of a=56.72, b=86.01, c=103.51 and α=89.99°, β=89.98°, γ=73.96°. The data was processed using Mosflm (Battye et al.). Each asymmetric unit contains a tetramer of Tpz1-Poz1-Rap1 complex. The native model (PDB: 5WE2) was used as a template for molecular replacement. With the high-confidence solution, the final model with clear Rap1 density was further built and refined (PDB: 5WE0).

To solve the structure of Tpz1-Poz1ΔN complex, crystals of Tpz1$^{475-508}$-Poz1$^{29-249}$ (loop 73-86 was replaced with GGA) were grown under the condition of 3.5-4.5% reagent alcohol, 0.2-0.3 M magnesium chloride, and 0.1 M Tris-HCl pH 8.0. Diffraction data were collected to 3.2Å resolution at the ALS beamline 501 and processed using Mosflm (Battye et al.). The crystals belong to space group P31 with unit cell parameter s of a=b=66.11, c=123.16 and α=β=90°, γ=120°. The crystal structure was determined by molecular replacement using the structure of Tpz1$^{475-508}$-Poz1-Rap1$^{470-494}$ (PDB: 5WE0) as a template. All structure figures were generated by using program PyMol (http://pymol.sourceforge.net).

Isothermal Calorimetry (ITC)

All ITC experiments were carried out in buffer B350 (25 mM Tris-HCl pH 8.0, 350 mM NaCl, and 0.5 mM TCEP) using a MicroCal iTC 200 (Malvern Instruments, Malvern UK) at 25°C. Data were analyzed using Origin 7.0 (OriginLab, Northhampton, MA) software.

Biolayer Interferometry (BLI) and K_d Calculation

BLI were performed in black 96-well plates (Greinerbio-one, Germany) on OctetRED96 instrument (ForteBio, USA). Prior to use, biosensors were soaked in binding assay (BA) buffer (20 mM Tris-HCl, pH 8.0, 350 mM NaCl, 0.2% NP-40, 0.5 mM DTT, 0.1 % BSA) for at least 10 min. BLI assays consisted of six steps, all performed in BA buffer: initial base line (30 s), loading (120 s), Quenching (120 s), base line (60 s), association (30 s) and dissociation (90 s). Each biotinylated protein was immobilized on each Streptavidin biosensor tip. For the loading step, protein concentrations were adjusted to yield signal intensity in the range of 2 to 3 nm. To quench free streptavidin, 4 μg/ml of biotin analogue, biocytin (Sigma), was used in BA buffer. Biotinylated protein-loaded sensors itself was measured as a control to subtract from experimental values before data processing. Sensorgrams were fit using global/1:1 binding model by ForteBio Data analysis version 9.0, from which the equilibrium dissociation constant (K_d) and association (k_{on}) and dissociation (k_{off}) rate constants were calculated.

Size-Exclusion Chromatograph-Multi-Angle Light Scattering (SEC-MALS)

SEC-MALS experiments were performed at 30°C with a P2500 and P3000 silica-based columns and Viskotek GPCmax/RI/DLS/MALS detection system (Malvern Instruments, Malvern, UK). Columns were equilibrated with buffer containing 25 mM Tris-HCl pH 8.0, 350 mM NaCl), followed by analytical grade bovine serum albumin (BSA) (Sigma-Aldrich, St. Louis, Mo.) injection for detector calibration and reference. All three protein complexes, the constructs used for solving the crystal structures, were injected into the same column for molar mass determination, respectively. The flow rate during experimental was maintained at 1 ml/min, with 100 mL injection volumes per trial.

Hydrogen/deuterium exchange mass spectrometry (HXMS)

HXMS was performed using a Waters Synapt G2Si equipped with nanoACQUITY UPLC system with H/DX technology and a LEAP autosampler essentially as described previously (Ramsey et al., 2017). The final concentrations of proteins and complexes in each sample were 5 μM. For each deuteration time, 4 μL complex was equilibrated to 25 °C for 5 min and then mixed with 56 μL D2O buffer (25mM Tris-HCl at pH 8.0, 350 mM NaCl, 15 mM imidazole, 0.5 mM TCEP) for 0, 0.5, 1, 2, or 5 min. The exchange was quenched with an equal volume of quench solution (3 M guanidine, 0.1% formic acid, pH 2.66). The quenched sample was injected into the 50 μL sample loop, followed by digestion on an in-line pepsin column (immobilized pepsin, Pierce, Inc.) at 15°C. The resulting peptides were captured on a BEH C18 Vanguard pre-column, separated by analytical chromatography (Acquity UPLC BEH C18, 1.7 μM, 1.0 X 50 mm, Waters Corporation) using a 7-85% acetonitrile in 0.1% formic acid over 7.5 min, and electrosprayed into the Waters SYNAPT

G2Si quadrupole time-of-flight mass spectrometer. The mass spectrometer was set to collect data in the Mobility, ESI+ mode; mass acquisition range of 200–2,000 (m/z); scan time 0.4 s. Continuous lock mass correction was accomplished with infusion of leu-enkephalin (m/z = 556.277) every 30 s (mass accuracy of 1 ppm for calibration standard). For peptide identification, the mass spectrometer was set to collect data in MSE, ESI+ mode instead.

The peptides were identified from triplicate MSE analyses of 10 μM protein, and data were analyzed using PLGS 2.5 (Waters Corporation). Peptide masses were identified using a minimum number of 250 ion counts for low energy peptides and 50 ion counts for their fragment ions. The peptides identified in PLGS were then analyzed in DynamX 3.0 (Waters Corporation). The following cut-offs were used to filter peptide sequence matches: minimum products per amino acid of 0.2, minimum score of 7, maximum MH+ error of 5 ppm, a retention time standard deviation of 5%, and the peptides were present in two of the three ID runs. After back-exchange correction (~30%), the relative deuterium uptake for each peptide was calculated by comparing the centroids of the mass envelopes of the deuterated samples with the undeuterated controls following previously published methods (Wales et al., 2008). The experiments were performed in triplicate, and independent replicates of the triplicate experiment were performed to verify the results. The back-exchange corrected data were plotted in Kaleidagraph and fitted with a double exponential curve.

Electrophoretic Mobility Shift Assay

20 nM 5′ end ^{32}P-labeled ssDNA (GTTACGGTTACAGGTTACG) was mixed with Pot1 proteins of specified concentrations in 20 μl reaction buffer (20 mM Tris-HCl [pH 8.0], 100 mM NaCl, 5 mM DTT, 2 mM MgCl2, 10% glycerol). The mixtures were then incubated at 4°C for 30 min. The protein-ssDNA complex were resolved by 7% non-denaturing polyacrylamide gel and imaged with a Bio-Rad phosphorimager.

Iodine Cleavage Protection Assay

Partially AMPαS, CMPαS, CMPαS or UMPαS substituted, 5' end labeled μT170 were prepared as mentioned above. 1 μM mixed unlabeled and 5' end labeled μT170 were incubated with GST-Est2-RBD, which was bound on GSH HiCap Matrix (Qiagen). Unbound RNA was washed out after 1 h incubation at 4°C. Iodine was dissolved in 100% EtOH and 2 μl iodine solution was added to RNA-bound beads. Iodine cleavage was performed at room temperature for 10 min. After reaction, RNA-protein was eluted with SDS extraction buffer (0.5% SDS, 0.3 M NaOAc) and the supernatant was collected, followed by phenol-chloroform extraction and EtOH precipitation. The result was resolved on a 9% denatured sequencing gel.

CHAPTER 3

Dissecting Fission Yeast Shelterin Interactions via MICro-MS Links Disruption of Shelterin Bridge to Tumorigenesis

Summary

Shelterin, a six-member complex, protects telomeres from nucleolytic attack and regulates their elongation by telomerase. Here, we have developed a strategy, called MICro-MS (Mapping Interfaces via Crosslinking-Mass Spectrometry), that combines crosslinking-mass spectrometry and phylogenetic analysis to identify contact sites within the complex. This strategy allowed identification of separation-of-function mutants of fission yeast Ccq1, Poz1, and Pot1 that selectively disrupt their respective interactions with Tpz1. The various telomere dysregulation phenotypes observed in these mutants further emphasize the critical regulatory roles of Tpz1-centered shelterin interactions in telomere homeostasis. Furthermore, the conservation between fission yeast Tpz1-Pot1 and human TPP1-POT1 interactions led us to map a human melanoma-associated POT1 mutation (A532P) to the TPP1-POT1 interface. Diminished TPP1-POT1 interaction caused by hPOT1-A532P may enable unregulated telomere extension, which, in turn, helps cancer cells to achieve replicative immortality. Therefore, our study reveals a connection between shelterin connectivity and tumorigenicity.

Introduction

The six-member telomere shelterin complex is vital for eukaryotic cells. It functions to regulate telomere elongation by telomerase, as well as to protect the ends of linear chromosomes from degradation and recognition as DNA damage sites (Artandi and Cooper, 2009; Jain and Cooper, 2010; Palm and de Lange, 2008). In human cells, the shelterin complex consists of double-stranded DNA (dsDNA) binders TRF1 and TRF2, single-stranded DNA (ssDNA) binder POT1, as well as RAP1, TIN2, and TPP1 (de Lange, 2005). The shelterin connects telomeric dsDNA with ssDNA by forming a proteinaceous bridge via protein interactions within the shelterin. Specifically, telomeric dsDNA binders TRF1 and TRF2 recruit TIN2 and RAP1 to the telomere; TIN2 then recruits TPP1-POT1 complex to the telomere (Takai et al., 2011). Since POT1 directly binds to the telomeric ssDNA, where telomere elongation by telomerase happens, TRF1-initiated POT1 loading to the telomere 3′ end via shelterin interactions is believed to directly block telomerase from elongating telomeres (Loayza and De Lange, 2003). Shelterin architecture in fission yeast, *Schizosaccharomyces pombe*, closely resembles that of mammals (Miyoshi et al., 2008) (Figure 1A). Either its dsDNA binder Taz1 (homolog of hTRF1/2) (Cooper et al., 1997) or its ssDNA binder Pot1 (Baumann and Cech, 2001) can independently recruit other shelterin components, Rap1, Poz1 (hTIN2 homolog), and Ccq1, to telomeres (Miyoshi et al., 2008). Using *S. pombe* as a model system, we recently discovered that the complete linkage within the shelterin complex, rather than individual shelterin components per se, regulates the extendibility of telomeres by telomerase (Jun et al., 2013). Disruption of this linkage leads to unregulated telomere elongation. These previous studies emphasized a critical role of shelterin complex assembly in telomere length regulation. Indeed, several human POT1

variants were found to predispose to the development of familial melanoma and carriers of some of these mutations have elongated telomeres (Robles-Espinoza et al., 2014; Shi et al., 2014). These mutations may allow cancer cells to achieve replicative immortality, and thus provide the same outcome as previously identified TERT (telomerase reverse transcriptase) promoter mutations (Horn et al., 2013; Huang et al., 2013) that lead to cancer-specific TERT activation (Borah et al., 2015). Most of melanoma-associated POT1 mutations reside in the highly conserved oligonucleotide and oligosaccharide-binding (OB) domains of POT1, thereby disrupting POT1-telomeric ssDNA interaction (Robles-Espinoza et al., 2014; Shi et al., 2014). In addition, one mutation, Ala532Pro (A532P), was found in the C terminus of POT1, which contains the TPP1-binding domain (Shi et al., 2014). However, the mechanism by which POT1-A532P facilitates melanoma formation is still unknown. To understand the role of shelterin complex in regulating telomere states, we need to have accurate information about protein-protein interfaces between shelterin components, and therefore a complete dissection of the individual interactions. However, obtaining structural information regarding this complex by X-ray crystallography or nuclear magnetic resonance (NMR) has proved challenging. Alternative approaches are needed to enable us to acquire protein interfaces information without the requirement for high-resolution structures.

In recent years, crosslinking mass spectrometry (XL-MS) has become an increasingly valuable tool for studying protein-protein interactions and structural interrogation of protein complexes due to technological advancement in mass spectrometry (MS) instrumentation, new development of crosslinking reagents and bioinformatics tools to facilitate MS analysis of crosslinked peptides (Erzberger et al., 2014; Kaake et al., 2014; Kao

et al., 2011, 2012; Politis et al., 2014; Walzthoeni et al., 2013; Yang et al., 2012), and an innovative algorithm developed for integrative structural biology utilizing distance restraints obtained from inter- subunit chemical crosslinking (Velázquez-Muriel et al., 2012). XL-MS studies involve protein crosslinking through a chemical linker simultaneously reacting with two amino acids that are in proximity to each other. Digestion of the crosslinked protein complex followed by peptide sequencing leads to the identification of crosslinked peptides, and consequently, proximal residue pairs. Because these crosslinked residues are constrained by the length of the linker used, the distribution of the crosslinked residue pairs helps probe protein-protein proximity. Unlike X-ray crystallography or NMR, XL-MS does not require samples with high concentration and purity. It also captures interactions from dynamic states, thus making it applicable to a broad range of protein complexes. However, XL-MS has proved challenging due to the complex fragmentation pattern of crosslinked peptides, which frequently prevents unambiguous identification of the crosslinked sequences. Recently, a new class of MS-cleavable crosslinker, disuccinimidyl sulfoxide (DSSO) was developed, which contains two symmetric MS-cleavable sites that preferentially cleave prior to the breakage of peptide backbones during collision-induced dissociation (CID) (Kao et al., 2011). In combination with multistage mass spectrometry (MS^n) and tailored bioinformatics tools, DSSO-based XL-MS workflow enables easy interpretation and unambiguous identification of crosslinked peptides and has proved effective in elucidating structures of protein complexes (Kao et al., 2011, 2012).

In this study, we have developed a strategy *MICro-MS* (Mapping Interfaces via Crosslinking-Mass Spectrometry) by combining DSSO-based XL-MS workflow, phylogenetic

sequence analysis, and in vitro binding assays to identify protein-interaction interfaces without the need of obtaining high-resolution 3D structure of the complex. With this strategy, we comprehensively probed protein-protein proximity in Tpz1-centered complex in fission yeast shelterin and identified separation-of-function mutants of Ccq1, Poz1, or Pot1 that selectively disrupt their respective interactions with Tpz1. The identified mutants further reveal the critical regulatory roles of Tpz1 in telomere maintenance. We also found that POT1-A532P, a melanoma-associated POT1 mutation (Shi et al., 2014), lies in the POT1-TPP1 interface and causes weakened TPP1-POT1 interaction. Just as disrupting POT1-telomeric ssDNA interaction in other POT1 mutants predisposed to melanoma, such as Y89C, Q94E, R273L, and S270N (Robles-Espinoza et al., 2014; Shi et al., 2014), defective TPP1-POT1 interaction by hPOT1-A532P mutation equivalently breaks the complete shelterin linkage between telomeric dsDNA and ssDNA. Therefore, our work links shelterin connectivity to tumorigenesis. In addition, our *MICro-MS* strategy of identifying separation-of-function mutants to dissect protein complexes for functional examinations will be generally applicable to other important multi-component protein complexes in the cell.

RESULTS

Identifying Contact Residues in Protein-Protein Interaction Interfaces by MICro-MS

We set out to utilize chemical crosslinking coupled with mass spectrometry (XL-MS) to identify contact residues located in the interfaces of interacting telomere shelterin components. Since mutations of the contact residues can selectively disrupt defined interactions within shelterin components, this strategy will allow us to identify separation-of-function mutants of shelterin components. Separation-of-function mutants can selectively block specific interactions without disrupting overall protein complex architecture. Thus, they should poise us to elucidate the roles of specific shelterin interactions in telomere maintenance without perturbing their roles in chromosome end protection.

The general workflow is depicted in Figure 1B, in which DSSO crosslinking of purified protein complexes was first carried out to covalently connect residues within certain three-dimensional distance in the protein pairs that are specifically reactive to the crosslinker. Although the crosslinked residues in the protein complex might not be directly involved in mediating protein-protein interactions, they should at least be close to each other surrounding the interface. Therefore, the locations of the crosslinked residues point out where the binding interface is likely to be. The optimal crosslinking conditions were used to yield sufficient amounts of crosslinked products as evaluated by SDS-PAGE. The resulting crosslinked protein complexes were digested either in-solution or in-gel with trypsin and/or chymotrypsin to obtain the maximum coverage of detectable crosslinked peptides for LC-MS^n analysis. The mass to charge ratios of DSSO-crosslinked peptides were first measured during MS^1 analysis, and they were then subjected to collision induced dissociation (CID) during MS^2. Due to the presence of the robust sulfoxide C-S cleavage sites in the linker region, MS^2 analysis of a DSSO inter-linked

peptide would lead to physical separation of the two crosslinked peptide constituents, thus allowing for MS^3 sequencing of single peptide chains and subsequent identification using conventional database searching tools (Kao et al., 2011). Integration of the MS^n data (i.e., MS^1, MS^2, and MS^3) results in simplified and unambiguous identification of DSSO-crosslinked peptides (Kao et al., 2011). After identifying the crosslinked peptides and localizing lysine residues conjugated by DSSO, we mapped these residues to the phylogenetically compiled sequence alignment. We reasoned that functionally important residues (such as those for enzymatic activity, structural-fold determination, and protein complex assembly) should be evolutionarily conserved, and therefore represent leading candidates that contribute to protein-protein interactions. We introduced mutations to the conserved residues, especially the hydrophobic residues among them (as they constitute the hydrophobic core of protein-protein interactions), within approximately 8 to 15 amino acids from the crosslinked lysines, particularly in the regions where multiple lysine residues were identified as crosslinking points. In vitro GST pull-down and in vivo co-immunoprecipitation assays were subsequently performed to evaluate the degree that the introduced mutations can disrupt the targeted protein-protein interaction. Mutations of the contact residues in the protein-protein interaction interface should efficiently disrupt the protein interaction. We termed this integrated strategy to identify separation-of-function mutants disrupting specific protein interaction interfaces MICro-MS—Mapping Interfaces via Crosslinking-Mass Spectrometry.

Benchmarking *MICro-MS* with 3D Structure of Proteasome Subunits Rpn8-Rpn11 Complex

Next, we assessed the applicability of MICro-MS to a protein complex with determined high-resolution 3D structure. In 2012, DSSO-based XL-MS strategy was employed to unravel the structural topology of *Saccharomyces cerevisiae* 19S proteasome regulatory particle (Kao et al., 2012). Five inter-subunit, DSSO-mediated crosslinks were identified between Rpn8 and Rpn11 subunits, suggesting their spatial proximity as well as potential direct protein interaction interfaces between Rpn8 and Rpn11. In 2014, two groups independently solved the crystal structure of heterodimer of the MPN (Mpr1–Pad1–N-terminal) domains of Rpn8 (1–179) and Rpn11 (2–239) (Pathare et al., 2014; Worden et al., 2014). These two subunits primarily interact with each other through α helices forming two distinct interfaces. Interestingly, two pairs of DSSO-crosslinked lysines, Rpn8-K7:Rpn11-K218 and Rpn8-K28:Rpn11-K96, appear to be close to interface A and interface B, respectively, as shown in Figures 2A–2C. The rest three identified lysine-crosslinks locate in the residues beyond the MPN domains and thus are not covered in the crystal structure. From the 3D structure, we calculated distances between the crosslinked lysine pairs to be 19.4 and 18.3Å, respectively, falling in the range of DSSO effective reaction distance (~20 Å). In *Interface A* (shown in Figure 2B), the hydrophobic core of the interface is formed by four-helix bundle between α1, α4 of Rpn8 and α1, α4 of Rpn11. Specifically, side chains from residues L15, L16, and L19 in α1 of Rpn8 and residues M212, L216 and L213 in α4 of Rpn11 are the essential constituents of the hydrophobic interface. Remarkably, these interface residues are adjacent (within 15 amino acids) in primary sequence to the crosslinked lysines—K7 in Rpn8 and K218 in

Rpn11, respectively. Moreover, they belong to the most phylogenetically conserved residues around the crosslinking sites (Figures S1A and S1B). *Interface B* (shown in Figure 2C) is located between α2 of Rpn8 and α2 of Rpn11. A cluster of four methionines: M76 and M79 from Rpn8 as well as M91 and M94 from Rpn11 build the core of the interface, which is flanked by salt bridges between Rpn8-R24 and Rpn11-T98 and between Rpn8-D20 and Rpn11-R100. Identified DSSO-crosslinked lysine pair Rpn8-K28:Rpn11-K96 lies at the edge of the interface, very close to the interface residues in primary sequence. Evidently, our benchmarking results demonstrate a strong correlation between DSSO-crosslinked lysine pairs and contact residues in protein-interaction interfaces in the primary sequence. Thus, we are set out to utilize MICro-MS to identify contact residues in interaction interfaces of protein complexes with no existing high-resolution 3D structure.

Dissecting the Ccq1-Tpz1 Interacting Interface via MICro-MS

Tpz1, the fission yeast homolog of the mammalian shelterin component TPP1 (Houghtaling et al., 2004; Liu et al., 2004; Sexton et al., 2014; Wang et al., 2007; Ye et al., 2004), is a linchpin molecule interacting with three other shelterin components—Ccq1, Poz1 via its C-terminal domain (Tpz1-CTD), and with Pot1 using its N-terminal domain (Tpz1-NTD) (Figure 1A) (Miyoshi et al., 2008). Our previous work identified Tpz1 mutants that selectively disrupt the ability of Tpz1 to interact with each of its interacting partners and revealed an interesting interplay among the positive and negative regulators of telomere length homeostasis (Jun et al., 2013). To achieve a complete dissection of the

protein-protein interactions between Tpz1 and its interacting shelterin components, and therefore to define the boundary between positive and negative telomere regulators, we decided to further map the Tpz1-interacting surfaces on Ccq1, Poz1, and Pot1, respectively.

Ccq1 is more than 700 amino acids long, and it is extremely labor intensive and tedious to identify its point mutations that disrupt Ccq1-Tpz1 interaction via mutating every phylogenetically conserved residue in Ccq1. We set out to gather interface information by utilizing MICro-MS strategy. As Ccq1 (130–439) interacts with Tpz1 (415–458), we co-expressed recombinant Ccq1 (130–439) with Tpz1 (415–458) in *E. coli* and purified the complex. We then subjected the complex to chemical crosslinking using an optimized concentration of DSSO—5.0 mM. As shown in Figure 3A, the crosslinked Ccq1 (130–439) and Tpz1 (415–458) complex was observed, while the free form of both Ccq1 (130–439) and Tpz1 (415–458) decreased concomitantly. The covalently crosslinked Ccq1 (130–439)/Tpz1 (415–458) shows molecular weight of ~72 kDa. This agrees with the Ccq1-Tpz1 complex forming a dimer of Ccq1-Tpz1 heterodimer, as we observed in gel filtration analysis, in which the protein complex was examined in its native form (Figure S2A). The tryptic digests of crosslinked Ccq1-Tpz1 complexes were then analyzed by LC-MS^n. Figure 3B illustrates a representative MS^n analysis for unambiguous identification of DSSO crosslinked peptides. As shown, MS^2 analysis of a selected peptide (m/z 554.0333^{4+}) yielded two peptide fragment pairs, i.e., α_A/β_T (m/z $420.75^{2+}/678.31^{2+}$) and α_A/β_T (m/z $432.20^{2+}/662.83^{2+}$), which is characteristic to a hetero-inter-linked peptide (α-β) (Kao et al., 2011). Each fragment (α_A, β_T, α_T, or β_A) represents one of the two crosslinked peptide constituents modified with the defined remnants of the linker after its cleavage, thus suggesting this peptide is a DSSO inter-linked peptide. The dominant fragment pair ions

(α_A/β_T) were subsequently subjected to MS^{3+} analysis, in which the series of b (b_2~b_5) and y (y_1~y_5) ions detected for the α_A fragment unambiguously identified it as ^{171}IQEK$_A$IR^{176} of Ccq1, while the series of b (b_2~b_7, b_9) and y (y_2~y_3, y_5, y_7~y_9) ions detected for β_T unambiguously identified the peptide as ^{434}K$_T$PIPDYDFM(Ox)K^{443} of Tpz1. Finally, integration of the MS^n data precisely identifies the inter-link between Tpz1-K434 and Ccq1-K174, suggesting their close proximity in three-dimensional space. Based on our previous study, Tpz1-L449A is able to disrupt Ccq1-Tpz1 interaction both in vitro and in fission yeast cells. The MS^n identification of Tpz1-K434 and Ccq1-K174 crosslinked by DSSO in the Tpz1-Ccq1 complex (Figure 3B) is remarkable, because Tpz1-K434 is only 15 amino acids away from the previously confirmed Ccq1-interacting site on Tpz1 (L449) (Jun et al., 2013). We therefore suspected that Ccq1 residues that mediate Ccq1-Tpz1 interaction should also be around K174 of Ccq1, the residue crosslinked to Tpz1-K434. Next, we introduced point mutations individually to several conserved residues around the K174 region of Ccq1 (Figure S2B), and then the purified recombinant Ccq1 mutants produced in *E. coli* were subjected to GST pull-down assays to evaluate their binding ability to GST-Tpz1-CTD. As shown in Figure 3C, among nine Ccq1 mutants, Ccq1-L151R and Ccq1-F157A/K174E completely abolished association between Ccq1 and Tpz1. In addition, Ccq1-L171R, Ccq1-K174E, Ccq1-I175R, and Ccq1-F178R all significantly diminished Ccq1-Tpz1 interaction, whereas Ccq1-V152R and Ccq1-L177R still retain wild-type binding to Tpz1. Furthermore, we also confirmed that Ccq1 mutations, which interfere with Ccq1-Tpz1 interaction in vitro, also affect full-length Ccq1-Tpz1 interaction to the similar degree in co-immunoprecipitation assays (Figure 3D); however, they still maintain their interactions with Clr3—the interaction partner of Ccq1 in the SHREC complex (Sugiyama et al., 2007)

(Figure S2C). In addition, chromatin immunoprecipitation (ChIP) analysis of these Ccq1 mutants indicates that they can localize to telomeres as well (Figure S2D). Therefore, we identified separation-of-function mutants of Ccq1, specifically disrupting Ccq1-Tpz1 interaction.

After obtaining Ccq1 mutants disrupting Ccq1-Tpz1 interaction, we further asked whether these Ccq1 mutants eliminate the function of Ccq1 as a positive regulator of telomere length. As predicted, telomere length in *ccq1-L151R* and *ccq1-F157A/K174E pombe* cells, in which Ccq1-Tpz1 interaction is completely abolished, is stable but ~150 bp shorter than that in the wild-type cells, reminiscent of *tpz1-L449A* cells (Figures S2E and 3E) (Armstrong et al., 2014; Jun et al., 2013). *S. pombe* cells bearing *ccq1⁺* mutations that significantly diminish Ccq1-Tpz1 interaction, such as *ccq1-L171R*, *ccq1-I175R*, and *ccq1-F178R*, also have similarly shorter telomeres as *tpz1-L449A* cells. However, cells bearing *ccq1⁺* mutations, *ccq1-V152R* and *ccq-L177R*, which have little effect on Ccq1-Tpz1 interaction, maintain wild-type telomere length. Furthermore, *tpz1-L449A/ccq1-F157A/K174E* double-mutant cells have an almost identical telomere phenotype as either *ccq1-F157A/K174E* or *tpz1-L449A* cells (Figure S2F), indicating the mutations, either in Tpz1 or in Ccq1, affect the same functionality in telomere maintenance pathway. Much like *tpz1-L449A* cells, which maintain their short telomeres via homologous recombination pathway involving *rad51⁺*, *ccq1-F157A/K174E* cells also require *rad51⁺* to maintain their telomeres as deletion of *rad51⁺* in *ccq1-F157A/K174E* immediately abrogates the stably maintained short telomeres in *ccq1-F157A/K174E* cells (Figure S2G). Taken together, utilizing MICro-MS, we were able to identify Ccq1 mutants that are defective in interacting

with Tpz1, and we found that these Ccq1 mutants are functionally equivalent to *tpz1-L449A* in telomere maintenance.

A Poz1 Mutation that Prevents Tpz1 Binding Results in Dramatic Telomere Elongation

Having successfully employed MICro-MS to dissect Ccq1-Tpz1 interaction, we next applied this approach to define the significance of the Poz1-Tpz1 interaction. Using the same procedure as described above for Ccq1-Tpz1 complex, we analyzed DSSO-crosslinked Poz1-Tpz1 complex (Figure 4A) to identify crosslinked peptides and the lysine pairs that make the linkages. Interestingly, Tpz1-K499, a residue adjacent to Tpz1-I501—a previously identified Poz1-interacting residue in Tpz1 (Jun et al., 2013), was found to crosslink to K180, K190, and K192 of Poz1 (Figures 4B, S3A, and S3B). In addition, Tpz1-K500 was also observed to crosslink to Poz1-K190 (Figure S3C). This result suggests that a region around K180 and K192 of Poz1 may contain Tpz1 contact sites (Figure S3D). We therefore introduced mutations individually to three conserved residues around this region, Poz1-W174R, R196E, and W209A, and performed GST pull-down assay to evaluate their Tpz1 binding ability. Among these three Poz1 mutants, only Poz1-R196E completely abrogated Poz1-Tpz1 interaction as shown in Figure 4C. Accordingly, we found that Poz1-R196E also caused loss of Poz1-Tpz1 interaction in the *S. pombe* cells as detected by co-immunoprecipitation assays (Figure 4D).

We generated a yeast strain carrying the *poz1-R196E* mutation to evaluate its importance for telomere length homeostasis. *poz1-R196E* mutant cells had dramatically

elongated telomeres (Figures 4E and S3E), consistent with the phenotype previously observed for *tpz1-I501R* mutant strain (Jun et al., 2013), which also fails to form the Poz1-Tpz1 complex. Moreover, when *poz1-R196E* was coupled with *tpz1-I501R*, the double mutant also showed elongated telomere, similar to *poz1-R196E* single mutant with no additional telomere elongation (Figure 4F). These results indicate that Poz1-R196 is indeed functionally equivalent to Tpz1-I501 in mediating Tpz1-Poz1 interaction, a key linkage point in the negative regulation force imposed by shelterin complex upon telomerase.

Pot1 Is a Negative Regulator of Telomere Length and Protects Telomeres Redundantly with Tpz1

In *S. pombe*, Pot1 is the direct single-stranded telomeric DNA binder and is responsible for telomere 3′ end protection by forming a complex with Tpz1 (Miyoshi et al., 2008). Deletion of either protein can result in chromosome circularization, whereas disruption of Tpz1-Pot1 interaction by the Tpz1-I200R mutation conversely leads to telomere elongation (Jun et al., 2013). Pot1 interacts with the N-terminal domain of Tpz1 (Tpz1-NTD), which is distinct from Ccq1 and Poz1 binding regions in the C-terminal domain of Tpz1 (Tpz1-CTD). To achieve the complete dissection of the interfaces in Tpz1-mediated negative regulation of telomere elongation, we aimed to identify regions in Pot1 that mediate its interaction with Tpz1-NTD. As shown in Figure 5A, efficient crosslinking by DSSO was achieved with the purified Pot1–Tpz1-NTD complex. Further MS^n analyses revealed that two lysine residues (K180 and K226) in proximity to I200 position of Tpz1 were crosslinked to Pot1 (K403, K535, and K553) (Figures 5B and S4A–S4C). To design

separation-of-function mutations in Pot1 for specific disruption of the Pot1-Tpz1 interaction, several conserved residues around the crosslinked lysines were mutated (Figure S4D), and the mutants were tested for their interactions with Tpz1 both in vitro (by GST pull-down) (Figure 5C) and in vivo (by co-immunoprecipitation) (Figure 5D). We found that Pot1-I453R and Pot1-F520A completely disrupt Pot1-Tpz1 binding both in vitro and in vivo. In addition, we examined the crystal structure of the *Oxytricha nova* homolog of Pot1-Tpz1 complex—TEBP-α/β (Horvath et al., 1998) and found that secondary structure prediction of Pot1 imposed onto its homologous TEBP-α/β structure placed I453 and F520 of Pot1 at the protein interaction interface (Figure S4D), consistent with our binding data. We performed ChIP analyses to evaluate telomeric localizations of Pot1 and Ccq1 in Pot1-Tpz1 interaction-defective Pot1 mutant strains (Figures S4E and S4F), demonstrating that these mutations only disrupt Pot1-Tpz1 interaction with minimum effect on Pot1 or Ccq1 telomere association. In agreement with this, we found that these Pot1 mutants can bind to telomeric ssDNA in gel-shift assays (Figure S4G). Reminiscent of *tpz1-I200R* cells, telomeres in both *pot1-I453R* and *pot1- F520A* mutant cells are elongated (Figures 5E and S4H) (Jun et al., 2013), indicating that Pot1 is also a negative regulator of telomere length. However, when we coupled *pot1-I453R* or *pot1-F520A* with *tpz1-I200R*, the double mutant showed no telomere signal, with part of the subtelomeric regions disappeared concomitantly (Figures 5F and S4I). These results strongly suggest that there is an alternative pathway that Tpz1 is involved in, in addition to the Pot1 pathway, to redundantly protect telomere erosion.

In summary, we have successfully employed MICro-MS to comprehensively map Tpz1-centered protein-protein interfaces in fission yeast shelterin. As a result, we

successfully identified mutants of Ccq1, Poz1, and Pot1 that selectively disrupt their respective interactions with Tpz1, the linchpin molecule that is functionally positioned between the positive and negative regulators of telomere elongation.

A Human POT1 Variant in Family Melanoma Patients Has Compromised hPOT1-hTPP1 Interaction

Replicative telomere attrition is one of the key restriction mechanisms that form a key barrier to infinite cell proliferation. As a result, a hallmark of cancer cells is their ability to circumvent multiple regulatory mechanisms that normally restrict cell proliferation (Hanahan and Weinberg, 2011). The integrity of telomere shelterin structure is essential for telomere length homeostasis, which, in turn, enables the anti-proliferative barrier set by short telomeres (Günes and Rudolph, 2013). Indeed, it has been shown that long telomeres can bypass the requirement of telomerase activation in the process of tumorigenesis (Taboski et al., 2012). Recently, two studies have linked 4%–6% of familial melanoma cases to germline variants in the gene encoding human POT1, the first shelterin component found to be mutated in cancer (Robles-Espinoza et al., 2014; Shi et al., 2014). Among these hPOT1 variants, many alter key residues in the N-terminal OB domains of POT1, causing the inability of hPOT1 to bind to telomeric ssDNA and leading to longer telomeres (Robles-Espinoza et al., 2014; Shi et al., 2014). However, one familial melanoma hPOT1 variant (hPOT1-A532P) contains a point mutation in the C terminus of hPOT1, and therefore is unlikely to disrupt POT1-ssDNA binding. Given our knowledge gained from fission yeast Pot1-I453R, which disrupts Pot1-Tpz1 interaction and aligns to where hPot1-

A532 locates (Figure S5), we suspected that the hPOT1-A532P mutation might reside in the TPP1 (human counterpart of fission yeast Tpz1) interaction surface. Thus, hPOT1-A532P might disrupt hPOT1-hTPP1 interaction, thereby facilitating tumorigenesis by causing inappropriate telomere elongation, similar to fission yeast Pot1-I453R. To test this possibility, we in vitro translated hPOT1 and its mutants and evaluated their binding abilities to GST-hTPP1-NTD. Notably, hPOT1-A532P, as well as two other mutants in the adjacent regions, hPOT1-V529R and L538R, has significantly weakened hPOT1-hTPP1 interaction (Figures 6A and 6B). This result emphasizes the importance of the intact "shelterin bridge" in telomere length regulation and explains how mutations in a shelterin component overcome the replicative telomere barrier, and thus lead to tumorigenesis.

Discussion

MICro-MS Is Effective in Identifying Functional Protein-Protein Contact Residues

Identifying interfaces between protein components, and generating separation-of-function mutants thereafter, is a prerequisite for elucidating the functional role of each component in the large multi-protein complex, such as the shelterin complex at the end of our chromosomes. For proteins that have multiple interaction partners, such as Tpz1 in fission yeast shelterin complex, its separation-of-function mutants are absolutely required to elucidate the specific roles of each of these protein interactions. However, X-ray crystallography and NMR spectroscopy have been the main experimental techniques that provide the structural details of protein-protein interfaces, and consequently, the

knowledge to design separation-of-function mutants. Both approaches are very time consuming, labor intensive, and extremely demanding on the chemical and biophysical behavior of the protein complex. Thus, only a limited number of protein complexes are suitable for these high-resolution techniques. Here, utilizing XL-MS with a recently developed MS-cleavable linker DSSO, coupled with phylogenetic and biochemical analyses, we present an integrated strategy (Figure 1B) that successfully identified contact residues in Tpz1-centered protein- protein interfaces of fission yeast shelterin. The DSSO-based XL-MS workflow greatly facilitates the identification of crosslinked peptides, which, in turn, provides essential information about regions that are very likely to mediate protein-protein interactions. Phylogenetic analysis further narrows down the candidate residues to be mutated in the regions close to crosslinked residues, and, thereafter, GST pull-down assays identify residues directly involved in and contribute to the protein-protein interaction. This strategy can be directly applied to other protein complexes due to its simplicity, sensitivity, efficiency, accuracy, and speed. In addition, recent studies suggested the existence of evolutionarily co-varied residues as good candidates for contact residues across protein interaction interface because compensatory mutations occur in the interfaces to maintain interaction stability during evolution (Marks et al., 2011; Ovchinnikov et al., 2014; Weigt et al., 2009). Therefore, evolutionary covariation analysis can be combined with MICro-MS to more accurately identify interface residues by prioritizing candidate residues to mutate.

For MICro-MS, chemical crosslinking sets up the foundation for the overall outcome of this strategy. The linker length of the chemical crosslinker is crucial for linking residues pairs around the protein-interaction interface. DSSO has a linker length of 10.1 Å, resulting

in potential linkages between lysines within ~20Å. This is a distance that has been determined to be optimal for specifically crosslinking lysines across interfaces. When lysines are scarce in one of the interacting proteins or both, other crosslinking reagents targeting other amino acid residues such as cysteines or acidic residues (Leitner et al., 2014) can be utilized similarly to determine protein interaction contacts. Interfaces that are small can be potentially probed by crosslinkers with shorter linker length such as EDC (1-ethyl-3-(3-dimethylaminopropyl)carbodiimide hydrochloride), which targets acidic residues (D and E), with zero linker length. Incorporating CID-inducible cleavage group into chemical crosslinkers with different linker lengths and/or reactive groups targeting various side chains apparently has urgent need. For structurally heterogeneous samples, crosslinking mass spectrometry has the advantage of probing proximal regions of interacting proteins in different conformations. Unlike most other biophysical techniques, in which sample heterogeneity interferes with the generation of characteristic signals, for MICro-MS, different protein interactions existing in different conformations can be identified as distinct crosslinking pairs with crosslinked peptide counts proportional to its population in the sample. Moreover, capturing stable interactions in general is much easier than identifying transient ones, but stability is not a requirement; this is another aspect of MICro-MS that allows the stabilization of transient complexes through chemical crosslinking for subsequent analysis to identify residues close to the interfaces. Finally, methods such as yeast two-hybrid and peptide arrays are known to identify binary interactions and have been used extensively to identify domains that mediate protein interaction. They can also be utilized to identifying protein-protein interacting surfaces residues when coupled with alanine scanning of the whole or selected region of the protein

pairs. In addition, once protein domains responsible for interaction are identified via yeast two hybrid, they can be subject to MICro-MS, which provides leading candidate residues for both methods to test, significantly reducing the number of residues to mutate. It is worth mentioning that MICro-MS allows the study of each individual interface in multi-protein complexes concurrently.

Shelterin Connectivity, Telomere Length Regulation, and Familial Melanoma

Our recent study of fission yeast shelterin revealed that the complete linkage within shelterin, connecting double-stranded and single-stranded telomeric DNA, governs the telomerase-nonextendible state of the telomere (Jun et al., 2013). In this study, taking advantage of XL-MS with a MS-cleavable linker strategy, we achieved complete dissection of Tpz1-centered shelterin component interactions (Tpz1-Ccq1, Tpz1-Poz1, Tpz1-Pot1) and obtained separation-of-function mutants that facilitate the investigation of their roles in telomerase regulation, telomere protection, and potentially other cellular functions such as telomere silencing (Tadeo et al., 2013) and meiosis. These mutants emphasize the importance of shelterin connectivity in negatively regulating telomerase as we concluded from Tpz1 separation-of-function mutants. This is because any mutation that disrupts the shelterin connectivity from dsDNA to ssDNA, no matter in Tpz1 or in the Tpz1 interacting partners, uniformly leads to over-elongated telomeres. They also make exploring the regulation of telomere length homeostasis by shelterin components, especially its activator Ccq1 (Webb and Zakian, 2012), possible.

In addition, our study also has clinical significance. Since fission yeast and human have homologous shelterin components and architecture, the shelterin interaction interface information obtained from fission yeast can be easily applied to the human shelterin. This information will not only help design separation-of-function mutants of human shelterin components, it will also offer mechanistic insights to a constellation of genetic diseases caused by impaired telomere maintenance due to defects in telomere shelterin. Human POT1 is the first member of shelterin components whose loss-of-function variants were found to predispose to human cancers, such as familial melanoma (Robles-Espinoza et al., 2014; Shi et al., 2014) and chronic lymphocytic (Ramsay et al., 2013; Speedy et al., 2014). Many identified POT1 mutations occurs in the N-terminal OB-fold domain that directly binds to the telomeric ssDNA. All four well-studied OB-fold domain mutants of hPOT1 identified in familial melanoma patients, e.g., POT1-Y89C, POT1-Q94E, POT1-R273L, and POT1- S270N, fail to bind to telomeric ssDNA and cause cells to have elongated telomeres (Robles-Espinoza et al., 2014; Shi et al., 2014). This can be mechanistically explained by the loss of complete linkage connecting telomeric dsDNA to ssDNA via shelterin, due to the inability of the mutants to bind to ssDNA, and thereby keeping the telomere constitutively in the extendible state. With sufficiently long telomeres reserve, tumorigenesis will not be impeded by the lack of telomerase in the cell, and cancer cells thus can automatically overcome the anti-proliferative barrier set by short telomeres (Taboski et al., 2012). Long telomeres help cells gain replicative time in order to accumulate other mutations (loss of function for tumor suppressor and gain of function for tumor activator). Exploiting homology between fission yeast and human shelterins, we find that another POT1 mutation (POT1-A532P), found in familial melanoma patients, affects

POT1-TPP1 interaction. Based on what we learned from fission yeast, disrupting any point in the proteinaceous shelterin bridge between telomeric dsDNA and ssDNA would lead to elongated telomeres. Therefore, in that sense, defect in POT1-TPP1 interaction is equivalent to that in POT1-ssDNA interaction, both acting to downregulate the negative force of telomere elongation. Recently, in addition to POT1, point mutations clustered in the POT1-interacting domain of TPP1 were found in melanoma patients (Aoude et al., 2015), presumably disrupting POT1-TPP1 interaction just as POT1-A532P does. Interestingly, gain-of-function mutations in the hTERT promoter, which increase gene expression of hTERT, were recently found to be driver alterations in melanoma and other cancers (Horn et al., 2013; Huang et al., 2013). Upregulation of positive regulators of telomere elongation (such as hTERT) is equivalent to downregulation of the negative regulators (such as the shelterin bridge) (as shown in Figure 7) in leading to the deregulated telomere over-elongation, both helping the cancer cells to achieve replicative immortality, during and after the transformation.

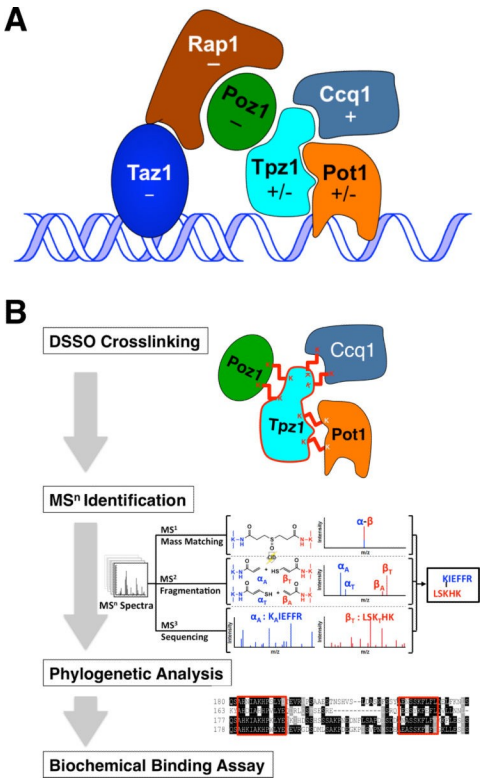

Figure 1. Fission Yeast Shelterin Complex and a Strategy—*MICro-MS*—to Dissect Its Interaction Interfaces. **(A)** Fission yeast shelterin complex is composed of telomeric sequence-specific double- stranded and single-stranded DNA binding proteins, Taz1 and Pot1, respectively, accompanied by their protein interaction partners, Rap1, Poz1, and Tpz1, forming a bridge between Taz1 and Pot1. If the deletion of a telomere protein causes telomere elongation, this protein is regarded as a negative regulator of telomere lengthening, and is therefore labeled "–", otherwise, labeled "+". For clarity, the stoichiometry of each individual component is not indicated in the figure and therefore only one copy of each component is shown. **(B)** Schematic illustration of MICro-MS strategy to identify contact residues at the interfaces of protein interactions. The MS-cleavable crosslinker DSSO chemically crosslinks neighboring lysine (K) residue pairs of two interacting proteins, which, in turn, can be identified via sequencing protease-digested crosslinked peptide pairs by multistage tandem mass spectrometry. The identified crosslinked residues are then mapped to the phylogenetically compiled sequence alignment. Around the locations of the crosslinked residues, mutations are individually introduced to the conserved residues. In vitro GST pull- down and/or in vivo co-immunoprecipitation assays are subsequently performed to evaluate the degree that introduced mutations disrupt the targeted protein-protein interaction.

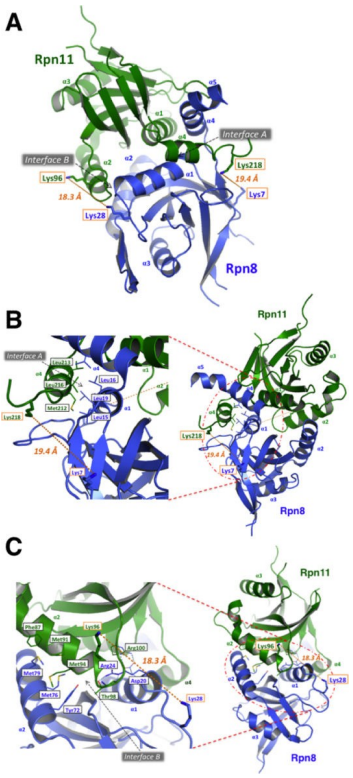

Figure 2. Benchmarking MICro-MS Using Rpn8-Rpn11 Complex. (A) Crystal structure of Rpn8-Rpn11 heterodimer is presented with Rpn8 colored in blue and Rpn11 colored in green. The two interfaces are designated as Interface A and Interface B. The crosslinked lysines boxed in orange are connected with orange dashed lines; the distances between the lysine pairs are shown next to the lines. **(B)** Close-up view showing a DSSO-crosslinked lysine pair (Rpn8-K7:Rpn11-K218) and interface A nearby in Rpn8-Rpn11 complex. The hydrophobic core of the interface is formed by four-helix bundle between α1, α4 of Rpn8 and α1, α4 of Rpn11. Specifically, side chains from residues L15, L16, and L19 (labeled in blue) in α1 of Rpn8 and residues M212, L216, and L213 (labeled in green) in α4 of Rpn11 are the essential constituents of the hydrophobic interface. **(C)** Close-up view showing a DSSO-crosslinked lysine pair (Rpn8-K28:Rpn11-K96) and interface B nearby in Rpn8-Rpn11 complex. Interface B is located between α2 of Rpn8 and α2 of Rpn11. A cluster of four methionines: M76 and M79 from Rpn8 (labeled in blue) as well as M91 and M94 from Rpn11 build the core of the interface (labeled in green), which is flanked by salt bridges between Rpn8-R24 and Rpn11-T98 and between Rpn8-D20 and Rpn11-R100. Identified DSSO-crosslinked lysine pair Rpn8-K28:Rpn11-K96 (linked by an orange dash line) lies at the edge of the interface, very close to the interface residues in primary sequence.

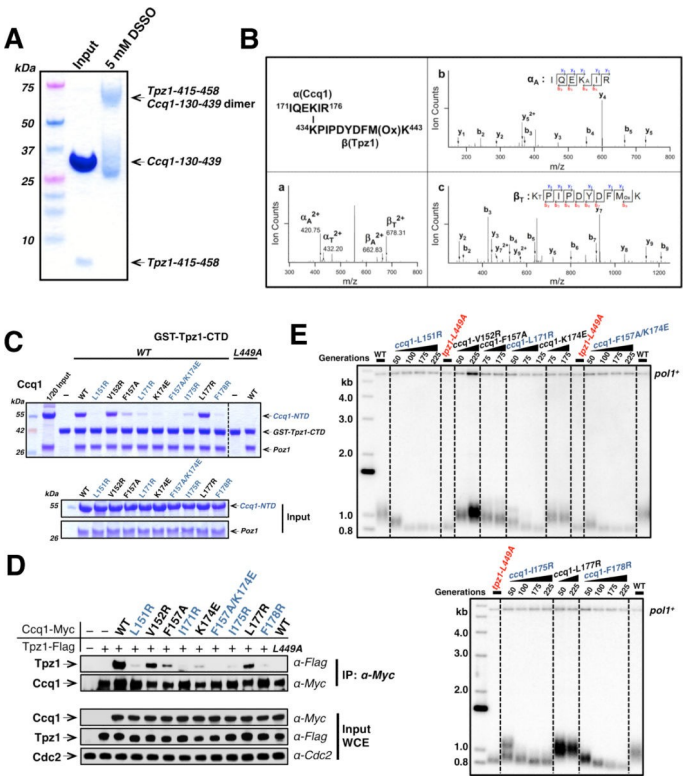

Figure 3. Dissecting Ccq1-Tpz1 Interacting Interface via MICro-MS. (A) SDS-PAGE of Ccq1 (130–439) and Tpz1 (415–458) complex before and after being crosslinked by DSSO. **(B)** (a) MS^2 spectrum of a quadruply charged crosslinked peptide α-β (m/z 554.2863^{2+}), in which two characteristic peptide fragment pairs were detected: α_A/β_T (m/z $420.75^{2+}/678.31^{2+}$) and α_T/β_A (m/z $432.20^{2+}/662.83^{2+}$). MS^3 spectra of (b) α_A (m/z 420.75^{2+}) and (c) β_T (m/z 678.31^{2+}) fragment ions detected in (a), which unambiguously identified their sequences as IQEK$_A$IR of Ccq1 and K$_T$PIPDYDFM$_{Ox}$K of Tpz1, respectively, demonstrating a linkage between residue K174 of Ccq1 and K434 of Tpz1. K$_A$, alkene-modified lysine; K$_T$, unsaturated thiol-modified lysine. **(C)** In vitro GST pull-down assays testing the binding of Ccq1 mutants and Poz1 to GST- Tpz1-CTD (406–508). GST-Tpz1-CTD-L449A serves as the negative control. Input: 1/20 of Ccq1 and 1/5 Poz1 before their incubation with GST-Tpz1-CTD. **(D)** Co-immunoprecipitation (coIP) assays evaluating the binding between full-length Tpz1 and Ccq1 mutants. *tpz1-L449A* serves as the negative control. Cdc2 was shown as the loading control. Input: 1/30 of input WCE (whole-cell extract). **(E)** Southern blot analysis of EcoRI-digested genomic DNA using the telomere DNA probe for the indicated *ccq1* mutant strains from successive re-streaks on agar plates. *ccq1* mutants disrupting Ccq1-Tpz1 interaction have shorter telomeres. In the telomere length analysis southern blots presented in this paper, the 1 kb plus marker from Life Technologies is used. Wild-type cells are denoted as "WT" in the blot. *pol1+* indicates the EcoRI-digested *pol1+* DNA fragment as loading control.

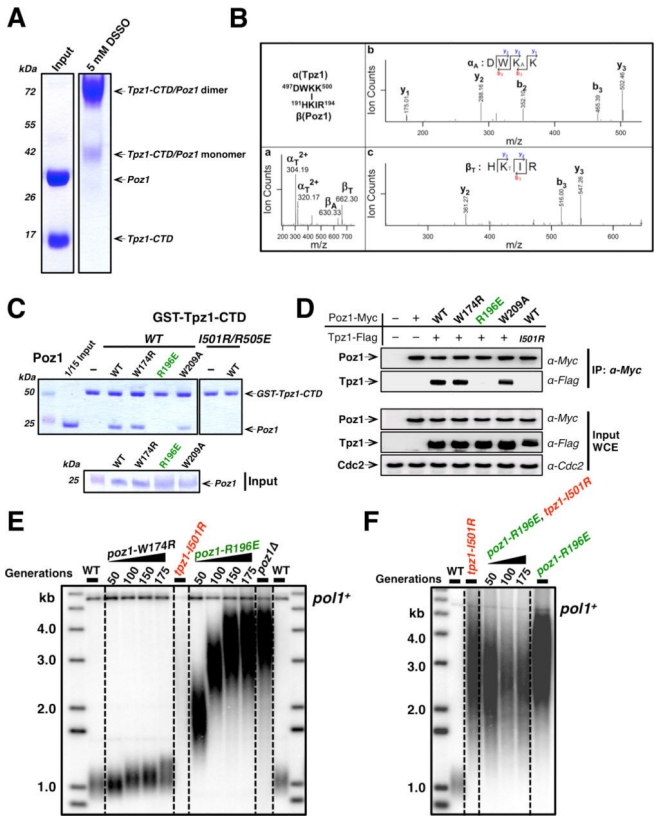

Figure 4. A Poz1 Mutation that Prevents Tpz1 Binding Results in Dramatic Telomere Elongation. (A) SDS-PAGE of full-length Poz1 and Tpz1 (406–508) complex before and after being crosslinked by DSSO. **(B)** (a) MS^2 spectrum of a triply charged crosslinked peptide α-β (m/z 429.5608^{3+}) in which two characteristic peptide fragment pairs were detected: α_A/β_T (m/z $304.19^{2+}/662.30^{+}$) and α_T/β_A (m/z $320.17^{2+}/630.3^{3+}$). MS^3 spectra of (b) α_A (m/z 304.19^{2+}) and (c) β_T (m/z 662.30^{+}) fragment ions detected in (a), which unambiguously identified their sequences as DWK_AK of Tpz1 and HK_TIR of Poz1, respectively, demonstrating a linkage between residue K192 of Poz1 and K499 of Tpz1. K_A, alkene-modified lysine; K_T, unsaturated thiol-modified lysine. **(C)** In vitro GST pull-down assays testing the binding of Poz1 mutants to GST-Tpz1-CTD (406–508). Poz1-R196E (colored in green) is defective in binding to GST-Tpz1-CTD. GST-Tpz1-CTD-I501R/R505E serves as the negative control. Input: 1/15 of the samples before their incubation with GST-Tpz1-CTD. **(D)** *poz1-R196E* disrupts Poz1-Tpz1 interaction as evaluated by coIP assays. *tpz1-I501R* serves as the negative control. Cdc2 was shown as the loading control. Input: 1/30 of input WCE. **(E)** Telomere length analysis southern blots for the indicated *poz1* mutant strains from successive re-streaks on agar plates. *poz1-R196E* causes telomere elongation. **(F)** Double-mutant strain *poz1-R196E/tpz1-I501R* cells have elongated telomeres similar to those of *poz1-R196E* or *tpz1-I501R* cells.

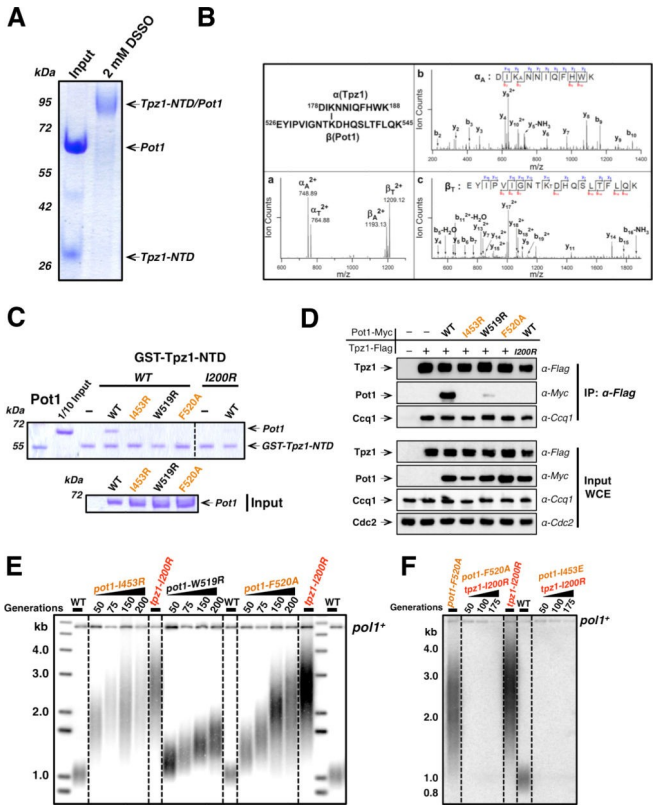

Figure 5. Pot1 Is a Negative Regulator of Telomere Length and Protects Telomeres Redundantly with Tpz1. (A) SDS-PAGE of full-length Pot1 and Tpz1-NTD (1–234) complex before and after being crosslinked by DSSO. **(B)** (a) MS^2 spectrum of a quadruply charged crosslinked peptide α-β (m/z 983.5108^{4+}) in which two characteristic peptide fragment pairs were detected: α_A/β_T (m/z $749.89^{2+}/1209.12^{2+}$) and α_T/β_A (m/z $764.88^{2+}/1193.13^{2+}$). MS^3 spectra of (b) α_A (m/z 748.89^{2+}) and (c) β_T (m/z 1209.12^{2+}) fragment ions detected in (a), which unambiguously identified their sequences as $DIK_AANNIQFHWK$ of Tpz1 and $EYIPVIGNTK_TTDHQSLTFLQK$ of Pot1, respectively, indicating a linkage between residue K180 of Tpz1 and K535 of Pot1. K_A, alkene-modified lysine; K_T, unsaturated thiol-modified lysine. **(C)** In vitro GST pull-down assays testing the binding of Pot1 mutants to GST-Tpz1-NTD (2–234). Pot1-I453R and Pot1-F520A (colored in orange) abolish the in vitro interaction with GST-Tpz1-NTD. GST-Tpz1-NTD-I200R serves as the negative control. Input: 1/15 of the samples before their incubation with GST-Tpz1-NTD. **(D)** CoIP assays evaluating the binding of Pot1 mutants and Ccq1 to full-length Tpz1. *pot1- I453R* and *pot1-F520A* completely disrupt Pot1-Tpz1 interaction. *tpz1-I200R* serves as the negative control. Cdc2 was shown as the loading control. Input: 1/30 of input WCE. **(E)** Telomere length analysis southern blots for the indicated *pot1* mutant strains from successive re-streaks on agar plates. *pot1-I453R* and *pot1-F520A* strains, in which Pot1-Tpz1 interaction is disrupted, have elongated telomeres. **(F)** Telomere deprotection phenotype was observed in both *pot1-F520A/tpz1-I200R* and *pot1-I453R/tpz1-I200R* double mutants.

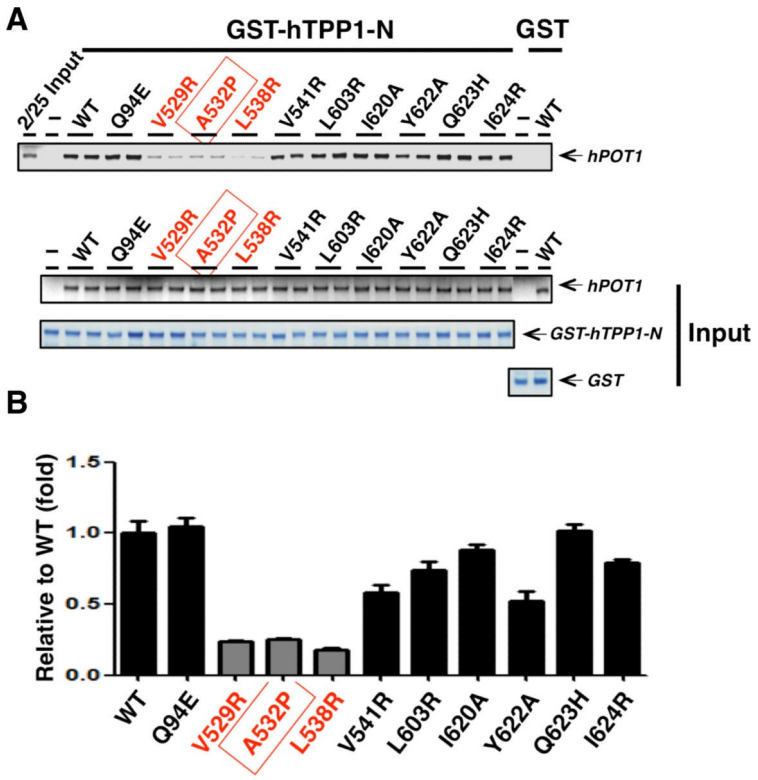

Figure 6. A Human Family Melanoma-Associated POT1 Variant Has Compromised hPOT1- hTPP1 Interaction. (A) In vitro GST pull-down assays testing the binding of hPOT1 mutants to GST-hTPP1-NTD (89–334). hPOT1-A532P (boxed in red) was identified in familiar melanoma patients. hPOT1-V529R and hPOT1-L538R (boxed in red) also negatively affect the interaction between hPOT1 and GST-hTPP1-NTD. All hPOT1 (WT and mutants) are labeled with 35S and visualized by Bio-Rad Phosphorimager. GST-hTPP1-NTD and GST are visualized by Coomassie blue staining. **(B)** Quantification of the binding between GST-hTPP1-NTD and hPOT1 mutants from (A). The interaction between GST-hTPP1-NTD and hPOT1-WT is set to 1.

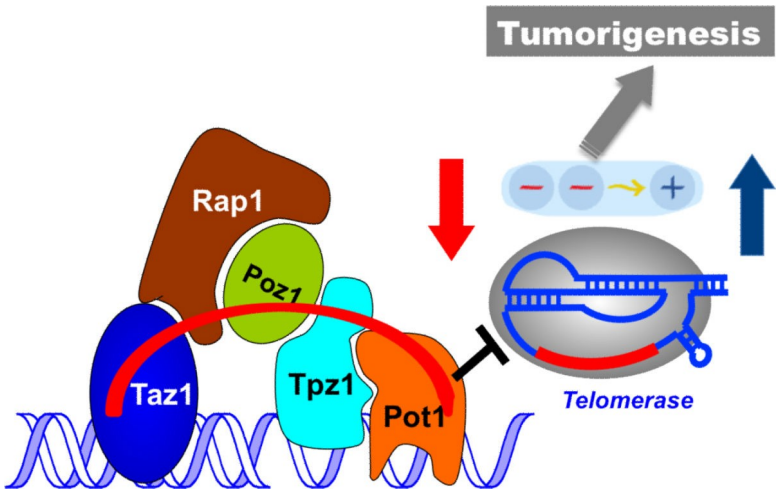

Figure 7. Model of Telomere Length Dysregulation-Related Tumorigenesis. Upregulation of positive regulators of telomere elongation (such as hTERT) is equivalent to downregulation of the negative regulators (such as the shelterin bridge) in leading to the deregulated telomere over-elongation, both helping the cancer cells to achieve replicative immortality, a key barrier to tumorigenesis.

CHAPTER 4

Multi-step coordination of telomerase recruitment in fission yeast through two coupled telomere-telomerase interfaces

Abstract

Tightly controlled recruitment of telomerase, a low-abundance enzyme, to telomeres is essential for regulated telomere synthesis. Recent studies in human cells revealed that a patch of amino acids in the shelterin component TPP1, called the TEL-patch, is essential for recruiting telomerase to telomeres. However, how TEL-patch—telomerase interaction integrates into the overall orchestration of telomerase regulation at telomeres is unclear. In fission yeast, $Tel1^{ATM}$/ $Rad3^{ATR}$-mediated phosphorylation of shelterin component Ccq1 during late S phase is involved in telomerase recruitment through promoting the binding of Ccq1 to a telomerase accessory protein Est1. Here, we identify the TEL-patch in $Tpz1^{TPP1}$, mutations of which lead to decreased telomeric association of telomerase, similar to the phosphorylation-defective Ccq1. Furthermore, we find that telomerase action at telomeres requires formation and resolution of an intermediate state, in which the cell cycle-dependent Ccq1-Est1 interaction is coupled to the TEL-patch—Trt1 interaction, to achieve temporally regulated telomerase elongation of telomeres.

Introduction

Telomeres, the physical ends of linear chromosomes, are essential for stable maintenance of chromosomes by facilitating chromosome end replication and preventing them from being degraded or fusing with each other (Artandi and Cooper, 2009; Palm and de Lange, 2008). In most eukaryotes, telomeres are comprised of short tandem DNA repeats. Rather than a blunt end, the telomere consists of a 3' single-stranded overhang called the G-tail that provides the substrate for telomerase to counteract iterative telomere shortening after each round of DNA replication. Telomerase is a ribonucleoprotein enzyme that extends telomeres utilizing an RNA component as template for its reverse transcriptase protein subunit (named TERT in vertebrates and Trt1 in fission yeast) (Autexier and Lue, 2006; Collins, 2006). This telomerase-dependent nucleotide addition is rigorously limited to late S/G2 phase. Dysregulation of telomerase and the subsequent perturbation of telomere length homeostasis lead to severe defects in cell proliferation. As a result, a constellation of genetic diseases caused by mutations in the telomere maintenance machinery (Sarek et al., 2015), referred to as 'telomeropathies' (Holohan et al., 2014) or 'telomere syndromes' (Armanios and Blackburn, 2012), have been continuously identified, and include dyskeratosis congenita (DC), aplastic anemia, and multiple types of cancers. Studies in telomerase regulation and telomere maintenance unveiled a precisely orchestrated process of telomerase recruitment (Hockemeyer and Collins, 2015; Nandakumar and Cech, 2013; Schmidt and Cech, 2015). In budding yeast, the interaction between the telomere-binding protein Cdc13 and the telomerase holoenzyme component Est1 regulates telomerase activation and its recruitment to the telomere (Chandra et al., 2001; Evans and Lundblad, 1999; Pennock et al., 2001; Qi and Zakian, 2000). Likewise, telomere-associated proteins in humans and fission yeast, which form a

highly conserved protein complex called shelterin (de Lange, 2005; Miyoshi et al., 2008), are essential to regulate telomere states, recruit telomerase, and govern its activity on telomeres. In fission yeast, the shelterin complex contains the double-stranded DNA (dsDNA) binding protein Taz1 (the homolog of TRF1/TRF2 in humans) (Cooper et al., 1997) and the single-stranded DNA (ssDNA) binding protein Pot1 (human POT1 ortholog) (Baumann and Cech, 2001), which are bridged via direct protein-protein interactions between Rap1 (Chikashige and Hiraoka, 2001; Kanoh and Ishikawa, 2001), Poz1, and Tpz1 (human RAP1, TIN2 and TPP1 orthologs, respectively) (Miyoshi et al., 2008). The human system shares a conserved shelterin arrangement by forming a similar 'shelterin bridge' architecture (Bianchi and Shore, 2008). Recent studies discovered a cluster of residues on human TPP1, collectively termed TEL-patch, which mediates TPP1-TERT interaction to recruit telomerase to telomeres (Nandakumar et al., 2012; Sexton et al., 2012; Zhong et al., 2012). TEL-patch mediated TPP1-TERT interaction also confers increased telomerase processivity in vitro (Nandakumar et al., 2012; Schmidt et al., 2014). Moreover, a detailed genetic study of TEL-patch mutants revealed multiple functions of TPP1 in telomerase recruitment, activation, and telomere length feedback regulation (Sexton et al., 2014). Altered TEL-patch function is clinically manifested as Hoyeraal-Hreidarsson (HH) syndrome. HH patients bear extremely short telomeres, even in comparison to other DC patients. A germline mutation causing a single-amino-acid deletion (K170Δ) in the human TPP1 TEL-patch that affects its telomerase recruitment function has been identified as the causal mutation of HH (Kocak et al., 2014). This signifies the critical telomerase recruitment function of the TEL-patch in normal stem cell development.

Interestingly, fission yeast *Schizosaccharomyces pombe*, which has a similar shelterin architecture to mammals, contains an additional shelterin component called Ccq1 (Flory et al., 2004), the functional homolog of which has not yet been identified in mammals. Ccq1 was demonstrated to be a cell cycle-dependent telomerase recruitment factor (Miyoshi et al., 2008; Tomita and Cooper, 2008). Further investigation showed that Ccq1 is required to bring telomerase to telomeres through its $Tel1^{ATM}$/$Rad3^{ATR}$-mediated Thr93 phosphorylation during late S phase, which creates a binding site for the 14-3-3 domain of Est1 (Moser et al., 2011; Webb and Zakian, 2012; Yamazaki et al., 2012). Est1 is an accessory protein of telomerase holoenzyme and is linked to the telomerase protein subunit (Trt1) via their co-association with telomerase RNA (TER1) (Leonardi et al., 2008). Ccq1 also interacts with Tpz1 (Miyoshi et al., 2008), and the Ccq1-Tpz1 interaction is therefore thought to bring the telomerase complex (Est1-TER1-Trt1) to the telomere (Moser et al., 2009) via the Ccq1 Thr93-phosphorylation dependent Ccq1-Est1 interaction. However, in-depth analyses further revealed that Ccq1-Est1 and Ccq1-Tpz1 interactions seem to be mutually exclusive (Armstrong et al., 2014). Moreover, Est1-Ccq1 interaction could be disrupted by TER1 in a yeast three-hybrid analysis and Est1 mutations that affect Est1-TER1 interaction also impair Est1-Ccq1 interaction (Armstrong et al., 2014; Webb and Zakian, 2012). In addition, based on a Ccq1-centric model, it is hard to explain why the telomeric association of Est1 requires not only Ccq1, but also Trt1 and TER1, which are downstream from Ccq1-Est1 interaction (Webb and Zakian, 2012). Therefore, the hypothetical Tpz1-Ccq1-Est1-TER1-Trt1 interaction chain seems unlikely to form to mediate telomerase recruitment. These results imply that an alternative mechanism exists to directly associate telomerase to other shelterin components, such as Tpz1, to initiate

telomere elongation in fission yeast in response to the cell cycle-dependent Ccq1-Thr93 phosphorylation (Chang et al., 2013).

In this study, we identified a Tpz1 mutation in the TEL-patch region that results in an ever shorter telomere (EST) phenotype, similar to the telomere phenotype of human TPP1 TEL-patch mutants. We observed decreased telomeric association of Trt1 and weakened Tpz1-Trt1 interaction in this Tpz1 TEL-patch mutant, indicating the conserved role of the TEL-patch in telomerase recruitment. Our epistasis analyses demonstrated that the Tpz1 TEL-patch functions by positively regulating Trt1. Furthermore, we found that telomerase action at telomeres requires formation and resolution of an intermediate state, formed via two cooperative telomere-telomerase interfaces involving cell cycle-regulated Ccq1-Est1 interaction and Tpz1 (TEL-patch)-Trt1 interaction. As a result, the temporal information for telomerase recruitment is endowed to the TEL-patch through the phosphorylation status of Ccq1 Thr93, thus achieving cell cycle-specific telomere elongation.

RESULTS

Tpz1 TEL-patch mutations lead to Ever Shorter Telomere—EST phenotype

Telomerase exists in low abundance in the cell. Therefore, the interaction between shelterin and telomerase has been proposed to enrich telomerase at chromosome ends. Indeed, a group of surface-exposed amino acids in the human TPP1 OB-domain, termed

TEL-patch, are found to be necessary for the telomerase recruitment to telomeres (Nandakumar et al., 2012; Sexton et al.,2012; Zhong et al., 2012). Although the fission yeast shelterin component Ccq1 has been connected to telomerase recruitment in this model organism, it is unlikely to be the sole factor to link Trt1 to telomeres (Armstrong et al., 2014). Additional interactions between shelterin components and Trt1 must exist to bring Trt1 directly to the telomere. Given the high conservation of the OB-fold domain arrangement in the N-terminal regions of *S. pombe* Tpz1 and human TPP1, we decided to test whether a Tpz1 TEL-patch functions in *S. pombe* as an interface between telomerase and shelterin. To identify candidate residues for such a TEL-patch in *S. pombe* Tpz1, we performed a sequence alignment between fission yeast Tpz1 and human TPP1 in combination with a secondary structure prediction (Figure 1A). We then identified 12 conserved Tpz1 residues in the region corresponding to the human TPP1 TEL-patch as candidate residues for fission yeast Tpz1 TEL-patch. *S. pombe* cells bearing individual mutations in these 12 residues of Tpz1 were tested for their telomere maintenance. *tpz1-I105R* and *tpz1-V107R* mutant strains appear to have destabilized Tpz1 protein and display a similar telomere deprotection phenotype (Figure 1—figure supplement 1) to *tpz1Δ* strain. The remaining 10 tpz1 mutant strains have comparable levels of Tpz1 expression as the wild-type strain (Figure 1—figure supplement 2). Strains bearing *tpz1-T73A*, *tpz1-K75E*, *tpz1-R76E*, *tpz1-I77R*, and *tpz1-R81E* displayed shortening telomeres (Figure 1B and Figure 1—figure supplement 1), implicating positive regulatory roles of these residues in telomere length regulation. Although *tpz1-T73A*, *tpz1-K75E*, and *tpz1-R76E* cells all have shortened telomeres, in contrast to the *tpz1-I77R* and *tpz1-R81E* cells, their telomeres remain stably short (Figure 1B and Figure 1—figure supplement 1). This telomere

phenotype is similar to that of previously identified fission yeast *tpz1-K75A* (Armstrong et al., 2014) or human *TPP1-L104A* (Sexton et al., 2014), proposed to affect telomerase activation and telomere length homeostasis set point, respectively. Strikingly, *tpz1-R81E* cells showed the classic *E*ver *S*horter *T*elomere (EST) phenotype (Lundblad and Szostak, 1989), similar to *trt1Δ* cells (Figure 1B) (Nakamura et al., 1997). The deterioration in telomere maintenance of *tpz1-R81E* strain started as early as ~50 generations. Its telomeres shorten to the critical length at 75 generations, and are almost completely lost afterwards. Gradual telomere loss was also observed in *tpz1-I77R* cells, albeit to a much milder degree than in *tpz1-R81E* cells. Furthermore, Tpz1-Arg81 and Trt1 appear to have an epistatic relationship because telomere shortening in the *tpz1-R81E/trt1Δ* double mutant is not additive (Figure 1C). The similar phenotypes observed for *tpz1-R81E*, *trt1Δ*, and *tpz1-R81E/trt1Δ* support a role of Tpz1-Arg81 in directly regulating telomerase activity on telomeres. Similar to the previously identified *tpz1-K75A* mutant that is defective in telomerase activation (Armstrong et al., 2014), *tpz1-K75E* and *tpz1-R76E* mutants have a milder telomere loss phenotype and their shortened telomeres are maintained for many generations. These observations clearly distinguish Tpz1-Arg81 from telomerase activation residues in Tpz1, i.e. Lys75 or Arg76.

We next asked whether the requirement for TEL-patch residue Tpz1-Arg81 can be bypassed by eliminating the negative shelterin linkage, which keeps telomeres constitutively in the telomerase-extendible state (Jun et al., 2013). To this end, we constructed a double-mutant strain, *tpz1-R81E/poz1Δ*, in which *poz1Δ* leads to defective shelterin linkage. As shown in Figure 1D, *tpz1-R81E/poz1Δ* cells presented EST phenotype and the cells senesced at a later generation, similar to the *trt1Δ/poz1Δ* mutant (Miyoshi et

al., 2008). A subpopulation survived at ~200 generations by circularizing their chromosomes to bypass the need for telomerase (Figure 1D and Figure 1—figure supplement 3). This result clearly indicates that Tpz1-Arg81 functions downstream of telomere switching from the non-extendible to the extendible state and upstream of telomerase action, most likely to mediate telomere-telomerase interaction. Therefore, we genetically demonstrated the existence of the TEL-patch in fission yeast Tpz1 that is functionally analogous to the TEL-patch of human TPP1.

The Tpz1 TEL-patch contributes to Tpz1-Trt1 interaction

Mutations of the TEL-patch residues in human TPP1 disrupt the direct interaction between TPP1 and TERT. Moreover, the TEN domain of human TERT was demonstrated to mediate its interaction with TPP1 (Schmidt et al., 2014), providing an interface required for the recruitment of telomerase to telomeres. In fission yeast, both Tpz1 and Ccq1 have been found to interact with Trt1 independent of telomerase RNA (Armstrong et al., 2014; Tomita and Cooper, 2008). To directly assess the function of the putative TEL-patch residue Tpz1-Arg81, we first examined the binding efficiency between Tpz1-R81E and Trt1 utilizing co-immunoprecipitation assay. As shown in Figure 2A,B and Figure 2—figure supplement 1, whereas Tpz1-E74R, Tpz1-K75A, Tpz1-K75E, and Tpz1-R76E pulled down similar amounts of Trt1 as the wild-type Tpz1, Tpz1-R81E only immunoprecipitated 30% of Trt1 compared to the wild-type Tpz1 (Figure 2B and C). Considerably reduced Tpz1-Trt1 interaction in the tpz1-R81E mutant correlates well with its progressive telomere shortening phenotype (Figure 1B), further supporting an essential role that Tpz1-Arg81 plays in mediating the

interaction between telomerase and shelterin at the telomere. Interestingly, *tpz1-I77R* cells lost about 50% of the Tpz1-Trt1 interaction (Figure 2B and C). This observation suggests that Tpz1-Ile77 is likely to be part of the TEL-patch as well, consistent with the compromised telomere maintenance in *tpz1-I77R* cells, albeit milder than that of the *tpz1-R81E* cells (Figure 1B). The *tpz1-R76E* mutant retains the wild-type Tpz1-Trt1 interaction (Figure 2A) but displays stably shortened telomeres. This implies that Tpz1-Arg76 is involved in telomerase activation, similar to what was previously described for Lys75 (Figure 2—figure supplement 1) (Armstrong et al., 2014).

If the Tpz1-Trt1 interaction were mediated solely via Ccq1, the reduced Tpz1-Trt1 interaction observed in *tpz1-R81E* cells would most likely result from reduced Tpz1-Ccq1 interaction, because other components in the proposed Tpz1-Ccq1-Est1-Trt1 interaction-chain remain intact. However, as shown in Figure 2B,D and E, all tested Tpz1 mutants, including Tpz1-R81E, interact with Ccq1 similarly to wild-type Tpz1. Moreover, the Ccq1-Trt1 interaction remains unchanged for all Tpz1 mutants as well (Figure 2E). Next, we tested whether two Ccq1 mutants, Ccq1-F157A/K174E and Ccq1-T93A, previously shown to be defective in Tpz1-Ccq1 (Liu et al., 2015) and Ccq1-Est1 (Moser et al., 2011) interactions, respectively, can completely abolish Tpz1-Trt1 interaction. As shown in Figure 2F, Tpz1-Trt1 interaction is clearly retained in both Ccq1-F157A/K174E and Ccq1-T93A mutants. This was particularly striking for the Ccq1-F157A/K174E mutant, in which Tpz1-Ccq1 interaction is completely disrupted. These data, together with previous studies (Armstrong et al., 2014; Webb and Zakian, 2012), argue against Ccq1 as the sole platform that recruits telomerase to telomeres. These results further point to the existence of the

TEL-patch in fission yeast Tpz1 and indicate a conserved function in the recruitment of telomerase.

The TEL-patch mutant of Tpz1 fails to localize telomerase to telomeres

To further test whether the failure of the *tpz1-R81E* mutant to replenish telomeres emanates from its inability to recruit telomerase to telomeres, we directly tested the group of Tpz1 OB-fold domain mutants for in vivo localization of telomerase to telomeres using ChIP assays. As expected, *tpz1-R81E*, which has significantly reduced Tpz1-Trt1 interaction, exhibited a dramatic decrease in the association of Trt1 with telomeres (Figure 3A). In contrast to the *tpz1-R81E* mutant, a telomerase activation-defective mutant *tpz1-R76E* displayed wild-type telomerase localization to telomeres (Figure 3A). The latter result is consistent with the phenotype of another previously described telomerase activation mutant strain *tpz1-K75A* (Armstrong et al., 2014). Interestingly, the *tpz1-I77R* mutant strain also showed significant decreased localization of Trt1 to telomeres (Figure 3A), consistent with the decreased Tpz1-Trt1 interaction observed in the co-immunoprecipitation assay (Figure 2B). In contrast, in all the tested Tpz1 OB-fold domain mutants, little effect was observed on the telomeric association of both Tpz1 and Ccq1 (Figure 3B and C). These results directly reveal a specific role for Tpz1 N-terminal OB-domain residues Ile77 and Arg81 in mediating telomere-Trt1 interaction and Trt1 recruitment. Moreover, since *tpz1-I77R* cells have a much more subtle telomere shortening phenotype than *tpz1-R81E* cells, we speculate that a threshold amount of residual telomerase interaction may be required for telomere maintenance upon disruption of the

Tpz1 TEL-patch. Taken together, we redefined the TEL-patch in fission yeast Tpz1, which functions analogously to the previously characterized TEL-patch in human TPP1 (Nandakumar et al., 2012; Sexton et al., 2012; Zhong et al., 2012).

Fusing Trt1 to Tpz1 bypasses the requirement for functional Tpz1 TEL-patch

Direct fusion of telomerase to a shelterin component has been shown to rescue the telomerase recruitment defect, but not other defects, such as telomere activation or telomere length homeostasis regulation in both fission yeast (Armstrong et al., 2014) and human embryonic stem cells (hESC) (Sexton et al., 2014). We next tested whether the inability of the Tpz1 TEL-patch mutant to maintain telomere length could be rescued by forcing telomerase to physically associate with telomeres. To this end, we measured telomere lengths of strains with Trt1 fused to Tpz1 mutants as previously described (Armstrong et al., 2014). Apparently, the strain bearing fused Trt1—Tpz1 TEL-patch mutant (*trt1—tpz1-R81E*) maintained the same telomere length as the *trt1—tpz1* wild-type strain (Figure 4A), indicating rescue of telomere shortening. However, fusion of Trt1 with Tpz1-L449A, which disrupts the Tpz1-Ccq1 interaction, failed to restore telomere maintenance, as previously reported (Armstrong et al., 2014). The expression levels of all Trt1—Tpz1 fusion proteins appear to be similar (Figure 4B). These results suggest that the Tpz1-Ccq1 interaction is required for aspects of telomere elongation besides bridging telomerase to telomeres. This interpretation is consistent with our previous genetic study implicating Ccq1 in switching telomeres from non-extendible to extendible state (Jun et al., 2013).

Est1 and Ccq1 form a stable complex through two binding sites

In fission yeast, Rad3^{ATR}/Tel1^{ATM}-dependent phosphorylation of Ccq1 at Thr93 promotes direct interaction between Ccq1 and Est1—a subunit of the telomerase holoenzyme (Moser et al., 2011; Yamazaki et al., 2012). The 14-3-3–like domain of Est1 was shown to recognize Ccq1 phosphorylated at Thr93 and was proposed to enable telomerase-telomeres association via the Ccq1-Tpz1 complex (Moser et al., 2011). Different from the proposed Tpz1-Ccq1-Est1 chain-interaction that connects telomerase to telomere shelterin, Ccq1-Est1 and Ccq1-Tpz1 interaction were demonstrated to be mutually exclusive (Armstrong et al., 2014) and the binding surfaces for Est1 and Tpz1 in Ccq1 are most likely to overlap. Our recent work utilizing a new strategy, called *MICro-MS* (Mapping Interfaces via Crosslinking-Mass Spectrometry), mapped the Tpz1-interacting interface on Ccq1 and isolated a group of separation-of-function mutants that specifically disrupt Ccq1-Tpz1 interaction (Liu et al., 2015). If Ccq1 interacts with Est1 via an overlapping surface that also mediates Ccq1-Tpz1 interaction, Ccq1 mutants that are defective in Ccq1-Tpz1 interaction is most likely to compromise Ccq1-Est1 interaction too. Indeed, as shown in Figure 5A, Ccq1-F157A/K174E and Ccq1-I175R, which were identified previously to be defective in Tpz1-Ccq1 interaction, both significantly diminished Ccq1-Est1 interaction in co-immunoprecipitation assays, whereas Ccq1-V152R and Ccq1-L177R still retained wild-type binding to Est1. Unexpectedly, we found that Ccq1-T93A, the Ccq1 mutant in the Rad3^{ATR}/Tel1^{ATM} phosphorylation site Thr93, did not completely abolish Ccq1-Est1

interaction; rather, it diminished Ccq1-Est1 interaction to a similar degree that was observed for Ccq1-F157A/K174E or Ccq1-I175R mutant.

We therefore speculated that Ccq1 and Est1 probably interact with each other via two binding sites: one provided by phosphorylated Thr93 and the other by the HDAC2/3-like domain at the N-terminus of Ccq1 (as depicted in Figure 5B). As a result, mutating either site only partially disrupts Ccq1-Est1 interaction. Indeed, as expected from the two-binding-site model, a Ccq1 mutant with both binding sites mutated—Ccq1-T93A/F157A/K174E completely lost its ability to bind to Est1 (Figure 5C). Previous mutational analysis of Est1 using the yeast two-hybrid assay identified residues in the predicted Est1 phospho-binding site (R79 and R180) that mediate the interaction between Est1 and Thr93-phosphorylated Ccq1 (Moser et al., 2011). Another study found that an additional residue—K252 in the 14-3-3–like domain of Est1 is also important for Est1-Ccq1 interaction, besides for Est1-TER1 interaction (Webb and Zakian, 2012). In the Est1 structure model, K252 is on a different surface compared to phospho-Thr93 binding residue R79 and R180. Est1-K252 is therefore very likely to be part of the binding site for the HDAC2/3-like domain at the N-terminus of Ccq1. In fact, in *ccq1-T93A/est1-K252E* cells, which bear mutations on Ccq1 and Est1 that in combination disrupt both binding sites, Ccq1-Est1 interaction could not be detected (Figure 5C). However, for strains *ccq1-T93A/est1-R79A/R180A* and *ccq1-F157A/K174E/est1-K252E*, in which mutations were introduced to only one of the Ccq1-Est1 binding sites with the other site intact, Ccq1 and Est1 interaction could still be observed at similar levels to single mutants *ccq1-T93A* or *est1-K252E* (Figure 5C). Altogether, our results indicate that phospho-Thr93 in Ccq1 contributes to one of the two binding sites that mediate Ccq1-Est1 interaction. The second

Est1-interacting surface resides in the HDAC2/3-like domain at the N-terminus of Ccq1, and overlaps with the Tpz1-interacting surface.

To further understand the relationship of Tpz1 and Est1 binding to the HDAC2/3-like domain in Ccq1, we performed a competitive binding assay. This evaluated the interaction between Est1 and Thr93-phosphorylated Ccq1 in the presence of Tpz1. In this assay, Flag-tagged Ccq1 was immunoprecipitated from the whole cell extract by a-Flag agarose beads. We then titrated increasing amounts of MBP-Tpz1-CTD to the Ccq1-Est1 complex. As shown in Figure 5E the addition of MBP-Tpz1-CTD partially displaced the Ccq1-bound Est1 at a high concentration of Tpz1. This did not occur when the Ccq1-binding defective mutant MBP-Tpz1-CTD L449A was added. Because of the entropic advantage provided by the phospho-Thr93-centered Est1-Ccq1 binding site, a high concentration of Tpz1 is needed to compete Est1 off the HDAC2/3-like domain of Ccq1. Taken together, the mutational analyses and the competitive binding assays indicate that Est1-Ccq1 interaction and Tpz1-Ccq1 interaction are mutually exclusive on the HDAC2/3-like domain of Ccq1 since both association events utilize the same binding surface on Ccq1 containing Phe157 and Lys174, et al. In addition, because phosphorylated Ccq1-Thr93 provides a secondary binding site for Ccq1-Est1 association, Tpz1-Ccq1-Est1 ternary complex can also form, likely in a transient manner, not as stable as Tpz1-Ccq1 or Ccq1-Est1 binary complexes. Thus, combined with our discovery of the TEL-patch in the N-terminal OB-domain of Tpz1, we suspect that the cell cycle-regulated Ccq1 (phospho-Thr93)-Est1 interaction can be coupled to the Tpz1 (TEL-patch)-Trt1 interaction via the Tpz1-Ccq1-Est1 intermediate complex to coordinate the recruitment of telomerase to telomeres.

TEL-patch function is regulated in a cell cycle-dependent manner

As shown before, Rad3^{ATR}/Tel1^{ATM}-dependent phosphorylation of Ccq1 at Thr93 is cell cycle-regulated and peaks during late S phase (Chang et al., 2013), correlating well with the temporal pattern of telomerase recruitment to the telomere (Moser et al., 2009; Webb and Zakian, 2012). Therefore, we asked whether the cell cycle-dependent phosphorylation of Ccq1 actually dictates the TEL-patch-mediated shelterin-telomerase interaction and thus restricts telomerase recruitment to late S phase. To test this, we incubated cdc25-22 cells at non- permissive temperature (36˚C) for 3 hr to arrest them in late G2 phase. Cells were then shifted to permissive temperature (25˚C) and cell samples were collected every 20 min for co-IP analysis to monitor Tpz1-Trt1 interaction in a 4-hr cell cycle window. As shown in Figure 6A and C, the interaction between Tpz1 and Ccq1 remained almost unchanged throughout the cell cycle. Strikingly, Tpz1 and Trt1 association gradually increased after release from the G2 arrest, peaked during late S phase (100–140 min), and then decreased to the level at G2 (Figure 6A and D). This temporal pattern of the Tpz1-Trt1 interaction along cell cycle progression correlates very well with that of Ccq1 phosphorylation (Chang et al., 2013), and consequently, with that of the Ccq1-Est1 interaction promoted by Ccq1 phosphorylation, which also peaked in late S phase (Figure 6E and G). Consistent with our hypothesis, when the critical Rad3^{ATR}/Tel1^{ATM} phosphorylation site in Ccq1—Thr93 was mutated, neither Tpz1-Trt1 interaction (Figure 6B and D) nor Ccq1-Est1 interaction (Figure 6F and G) peaked in late S phase. Therefore, we propose that through an intermediate telomerase recruitment complex formed by both Ccq1-Est1 and Tpz1-Trt1 interactions (Figure 7), the cell cycle information is delivered

through Ccq1 Thr93-phosphorylation to the TEL-patch on Tpz1. This in turn enables Tpz1 to directly position telomerase onto the telomere and elongate it during late S phase, after most of the genome has been replicated.

Discussion

Telomerase recruitment involving an intermediate state with two- pronged telomere-telomerase interfaces

Our study demonstrates that fission yeast Tpz1 also contains a TEL-patch in its OB-fold domain, analogous to its human ortholog—TPP1 (Nandakumar et al., 2012; Sexton et al., 2012; Zhong et al., 2012). A TEL-patch mutation causes drastically reduced association of telomerase with telomeres, and consequently an EST phenotype. Similar phenotypic consequences were previously reported for the Ccq1 Thr93 phosphorylation-deficient allele (Moser et al., 2011; Yamazaki et al., 2012). Moreover, our biochemical analyses reveal an unexpected complexity in the Ccq1-Est1 interaction involving two binding sites. As schematically illustrated in Figure 7, we envision that in late S phase, when the DNA replication machinery completes most of the genome, $Rad3^{ATR}$/$Tel1^{ATM}$ are activated and phosphorylate the critical Thr93 residue in Ccq1 at telomeres, priming the telomere for telomerase recruitment. Then, telomerase holoenzyme, minimally composed of Trt1-TER1-Est1, is attracted to the telomere by the cell cycle-regulated, phospho-Thr93-mediated Ccq1-Est1 interaction. At the same time, in a collaborative manner, Trt1 interacts with Tpz1 via the respective TEN domain and the TEL-patch residues, thus forming an

intermediate telomerase recruitment complex that further engages the telomerase core enzyme (Trt1-TER1) at the very 3' end of the telomere for nucleotide additions. Aided by phospho-Ccq1 Thr93, Est1-Ccq1 interaction at their second binding site takes place, resulting in dissociation of Ccq1 from Tpz1. Because Est1 may use the same surface to interact with Ccq1 as it interacts with TER1 (Webb and Zakian, 2012), Est1 is likely to depart from TER1 upon its binding to Ccq1. With phosphorylation of the critical Thr93 in Ccq1 disappearing after late S phase, Ccq1-Est1 interaction diminishes accordingly. Alignment of the very 3' end of telomeric ssDNA to the template region in TER1 might also participate in the telomerase recruitment process, and therefore, only Tpz1 on the extreme 3' end of the telomere, but not the majority of Tpz1 on the internal telomeric regions, is involved in forming the intermediate telomerase recruitment complex.

Ever since the very beginning of the telomere research at the molecular genetics level, the noncatalytic, accessory components of the telomerase holoenzyme, such as Est and Est3p in budding yeast, have been demonstrated to play equally important roles in telomere elongation as the catalytic core (telomerase reverse transcriptase and telomerase RNA) (Lundblad and Szostak, 1989). Indistinguishable progressive telomere shortening phenotypes are displayed by strains either with deletion of the telomerase RNA, the reverse transcriptase subunit, or accessory proteins (Leonardi et al., 2008; Lingner et al., 1997; Lundblad and Szostak, 1989; Webb and Zakian, 2008), suggesting that all these components work collaboratively to form a functional telomerase. Est1, whose homologs have been identified from yeasts to humans, has been proposed to recruit and activate telomerase RNP to telomeres in a cell-cycle dependent manner. Unexpectedly, a previous study discovered that the telomerase core, RNP, Trt1 and TER1 RNA, is also required for

the association of Est1 with the telomere (Webb and Zakian, 2012). Our finding that telomerase holoenzyme is recruited to telomeres via an intermediate state involving two-pronged cooperative Est1-Ccq1 and Trt1-Tpz1 interactions, uncovers the active role of Trt1 itself in the recruitment process. In addition, our model explains the intricate interdependence between Trt1, TER1, and Est1 for telomeric association of the holoenzyme.

What are the advantages of employing two cooperative telomere-telomerase interactions to recruit telomerase to telomeres? We think that this mode enables temporal and spatial regulation of telomerase recruitment. It has been shown in budding yeast that $Tel1^{ATM}$ prefers shorter telomeres than longer ones. We demonstrate here that the cell cycle-dependent interaction between Ccq1 and Est1 is coupled to the Tpz1 TEL patch-Trt1 interaction. Moreover, in fission yeast, strains with shorter telomeres show a higher level of Ccq1 phosphorylation (Moser et al., 2011). Therefore, shorter telomeres could have more access to telomerase due to the higher level of Thr93 phosphorylation in Ccq1. After locating which telomere to elongate, interaction between the TEL-patch of Tpz1 and the catalytic subunit Trt1 further orients the very 3' end of telomeric ssDNA via the sequence-specific Pot1/Tpz1-ssDNA interaction to the active site of Trt1. Two-interface recruitment mode has been observed in other pathways for similar purposes. For example, 53BP1, an important effector of DNA double-strand-break (DSB) response, simultaneously recognizes mononucleosomes containing dimethylated H4K20 (H4K20me2) and H2A ubiquitinated on Lys15 (H2AK15ub) (Fradet-Turcotte et al., 2013). There, it was proposed that the engagement of H4K20me2 by the Tudor domain of 53BP1 positions its ubiquitination-dependent recruitment (UDR) motif in the correct orientation to contact the epitope

formed by H2AK15ub, and thus to ensure that 53BP1 responds only to bona fide DSB signaling.

Multi-functionality of Tpz1 in regulating telomerase action at telomeres

Within the fission yeast telomere shelterin complex, Tpz1 physically lies in the middle of the telomeric ssDNA and dsDNA binding proteins. Functionally, Tpz1 is positioned between the positive and negative regulators of the telomerase elongation. Tpz1 directly interacts with three other shelterin components: Poz1, Ccq1, and Pot1. This unique position of Tpz1 in the shelterin complex enables its architectural role in shelterin complex assembly and underscores its potential coordination roles in communicating the dsDNA length and/or structural information to the 3' end of ssDNA—telomerase's ultimate destination. In our previous studies, utilizing biochemically identified Tpz1 separation-of-function mutants that can individually but specifically disrupt Tpz1's interactions with Poz1, Ccq1, or Pot1, we found that Tpz1-mediated complete linkage between telomere dsDNA and ssDNA binding proteins in the shelterin complex is required for defining the telomerase-nonextendible state of telomeres (Jun et al., 2013). Disruption of the linkage on either the dsDNA binder or the ssDNA binder side of Tpz1 causes unregulated elongation of telomeres. In addition to maintaining the telomerase-nonextendible state, through its interaction with Ccq1, Tpz1 may also activate the telomerase-nonextendible state of telomeres by participating in breaking down the 'shelterin bridge'. Moreover, Lys75, which is close to the TEL-patch in the OB-fold domain of Tpz1, was demonstrated to have telomerase activation function, the step that follows successful telomerase-telomere

association and alters telomerase conformation to become competent for telomere synthesis (Armstrong et al., 2014). Recently, SUMOylation of Tpz1-Lys242 in late S phase was shown to enhance the Tpz1-Stn1 interaction, promote Stn1-Ten1 association with telomeres, and thus to coordinate synthesis of the telomeric lagging strand by Polα stimulated via Stn1-Ten1-Polα interaction (Hannan et al., 2015; Miyagawa et al., 2014). The TEL-patch in Tpz1 and its conserved role in telomerase recruitment characterized in this work further extend the versatility of Tpz1 in telomere length homeostasis. Evidently, the ability to regulate the telomeric state together with the role of recruiting/activating telomerase and coordinating Polα are integrated into one single telomeric protein—Tpz1. This integration ensures timely, accurate, and efficient coupling of conformational transitions of the telomere to the engagement and activation of the telomerase RNP.

Conservation of telomerase recruitment mechanisms

Although the TEL-patch of the shelterin component TPP1 acting as the telomere-telomerase interface was initially discovered and extensively studied in human cells (Hockemeyer and Collins, 2015; Schmidt and Cech, 2015), upstream regulatory events of TEL-patch-mediated telomerase recruitment remain to be elucidated. In contrast, regulatory pathways and factors that control telomerase recruitment have been fairly well studied in both budding and fission yeasts due to their convenient and precise genetic manipulability. For instance, in budding yeast, cell cycle-specific assembly and disassembly of active telomerase RNP at telomeres have been shown to restrict telomerase action to late S phase (Tucey and Lundblad, 2014). Moreover, telomerase tends to preferentially

elongate short telomeres and Tel1^{ATM} is enriched in short telomeres to achieve telomere length homeostasis (Bianchi and Shore, 2007; Sabourin et al., 2007). Cdk1 was also shown to control the temporal recruitment of telomerase by directing the timing of Cdc13 and Stn1 phosphorylation along cell cycle progression (Li et al., 2009; Liu et al., 2014). Two recent studies unveil the conserved regulatory role of ATM/ATR in human recruitment and telomere elongation (Lee et al., 2015; Tong et al., 2015); however, the downstream substrate is mostly unknown.

In this work, we uncovered the conservation of the TEL-patch in fission yeast Tpz1, with similar biochemical and functional roles to human TPP1. This similarity between human and fission yeast makes us speculate that the conservation could probably be extended to other aspects of the telomerase recruitment pathway. Is it possible that human telomerase recruitment also involves two coupled telomere-telomerase interactions? What is the Ccq1-Est1 interaction equivalent in human cells? In fact, human TIN2 (Poz1 homolog) has been demonstrated to be essential for telomerase recruitment (Abreu et al., 2010). DC mutations in the C-terminal region of TIN2 (not contained in Poz1) lead to defective association of TIN2 with telomerase (Frank et al., 2015; Yang et al., 2011). As illustrated in Figure 7—figure supplement 1, we speculate that the C-terminal domain of TIN2 is likely to be the Ccq1-functional equivalent in humans and interacts either with hEST1 or the telomerase RNP directly, forming the second interface between telomeres and telomerase in addition to the TPP1 (TEL-patch)-TERT (TEN domain) interaction. Moreover, TIN2 may also be subject to cell cycle-controlled post-translational modifications, and thus mediate its telomerase recruitment function in a highly regulated way.

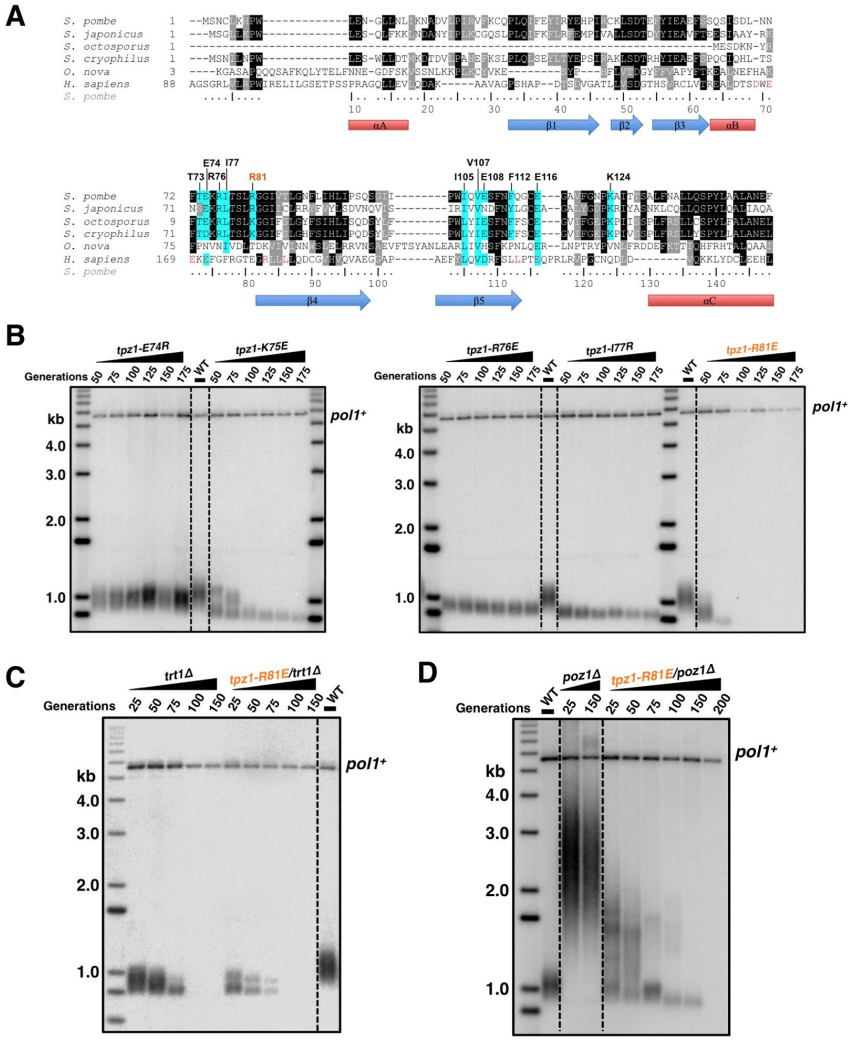

Figure 1. Fission yeast Tpz1 TEL-patch mutant leads to an EST phenotype. (A) A sequence alignment of OB fold-domains between fission yeast Tpz1, human TPP1 and *Oxytricha nova* TEBP-β, in combination with a secondary structure prediction. Twelve conserved fission yeast Tpz1 residues subjected to mutagenesis are highlighted in blue with their identities and sequence numbers indicated above the alignment. Residues colored in red are previously identified TEL-patch residues in human TPP1 and mutations of them lead to compromised TPP1-TERT interaction. Black and grey shading indicates sequence identity and similarity, respectively. If the sequence is identical among at least 50% of species, the residues will be shaded in black. The same rule applies to sequence similarity, which is shaded in grey. **(B)** Southern blot analysis to measure telomere lengths using EcoRI-digested genomic DNA visualized by the telomere DNA probe for the indicated tpz1 mutant strains from successive re-streaks on agar plates. *tpz1-K75E*, *tpz1- R76E*, *tpz1-I77R*, and *tpz1-R81E* strains caused telomere shortening and *tpz1-R81E* cells showed the classic *Ever Shorter Telomere (**EST**)* phenotype. For the telomere length analysis southern blots presented in all the figures, the 1 kb plus marker from Invitrogen is used. Wild type cells are denoted as 'WT' in the blot. *pol1⁺* indicates the EcoRI-digested *pol1⁺* DNA fragment used as a loading control. **(C)** Double-mutant strain *tpz1-R81E/trt1Δ* shows ***EST*** telomere phenotype, similar to the *trt1Δ* single-mutant strain. **(D)** Double-mutant strain *tpz1-R81E/poz1Δ* shows progressive telomere shortening phenotype.

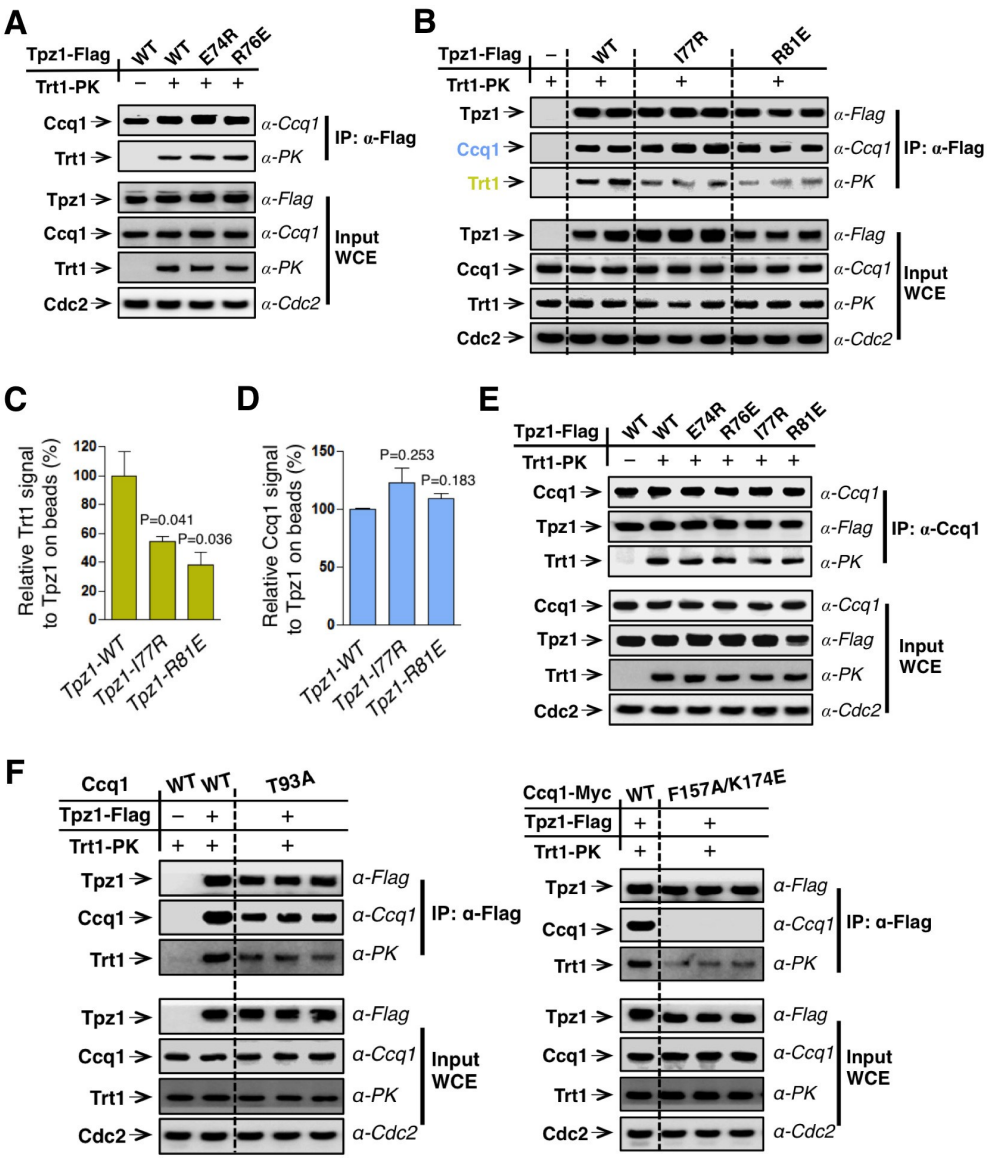

Figure 2. The Tpz1 TEL-patch mutant is defective in Tpz1-Trt1 interaction. **(A)** Coimmunoprecepitation (Co-IP) assays evaluating bindings between Trt1 and Tpz1-E74R and Tpz1-R76E. Cdc2 was shown as the loading control. Input: 1/30 of input WCE (whole cell extract). **(B)** Co-IP assays showing that Tpz1-I77R and Tpz1-R81E significantly decrease interaction between Tpz1 and Trt1. Cdc2 was shown as the loading control. Input: 1/30 of input WCE. **(C)** Quantification of the binding efficiency between Trt1 and Tpz1 mutants from (B). The interaction between Trt1 and Tpz1-WT is set to be 100%. Trt1 levels in the IP were normalized to Tpz1 bound to the beads. **(D)** Quantification of the binding efficiency between Ccq1 and Tpz1 mutants from (B). The interaction between Ccq1 and Tpz1-WT is set to be 100%. Ccq1 levels in the IP were normalized to Tpz1 bound to the beads. **(E)** Co-IP assays evaluating the binding efficiency between Trt1 and Ccq1 in various Tpz1 mutant cells. Cdc2 was shown as the loading control. Input: 1/30 of input WCE. **(F)** Co-IP assays evaluating the binding efficiency between Trt1 and Tpz1 in *ccq1-T93A* and *ccq1-F157A/K174E*. Cdc2 was shown as the loading control. Input: 1/30 of input WCE.

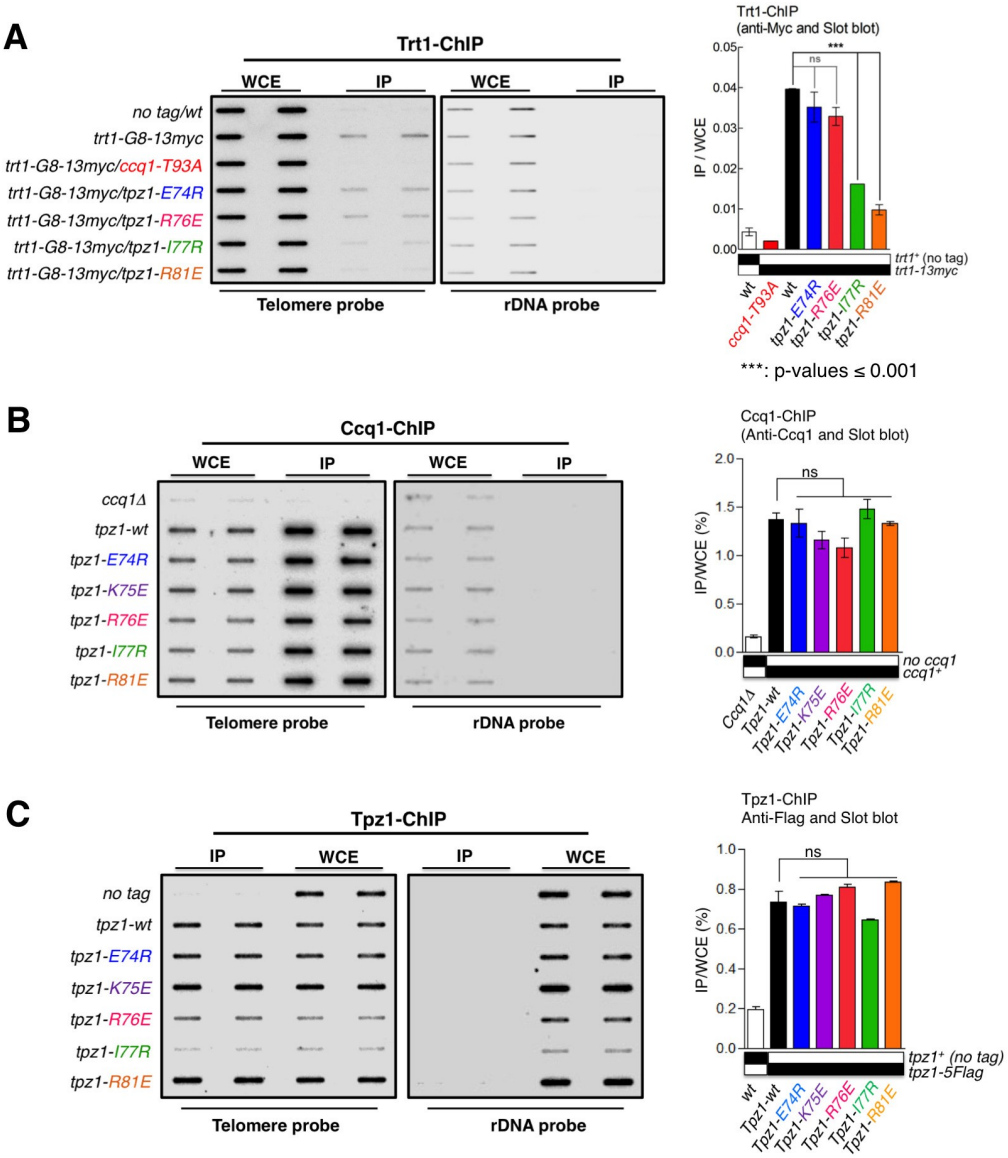

Figure 3. The Tpz1 TEL-patch mutant fails to localize telomerase to telomeres. (A–C) Enrichment of Trt1 (A), Ccq1 (B) or Tpz1 (C) at telomeres is monitored by chromatin immunoprecipitation (ChIP) assay. Slot-blot was used to visualize telomere association of Trt1, Ccq1 or Tpz1 in each indicated *tpz1* mutant strains. Error bars in the quantitation of the slot-blot analysis represent standard deviations of two individual repeats.

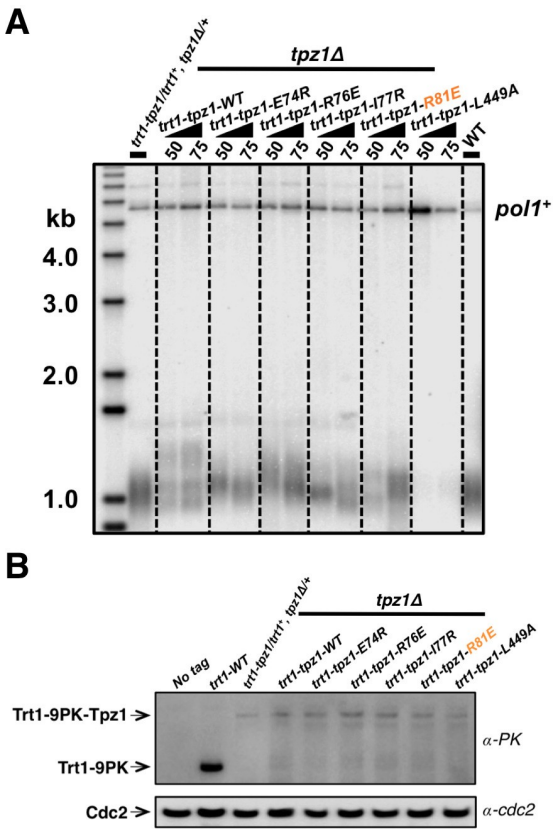

Figure 4. Fusing Trt1 to Tpz1 bypasses the requirement for functional Tpz1 TEL-patch. (A) Southern blot analysis to measure telomere lengths using EcoRI-digested genomic DNA visualized by the telomere DNA probe for the *trt1-tpz1* fusion strains with indicated WT or mutant versions of tpz1. 9PK tags were inserted between trt1 and tpz1. **(B)** Western blot showing expression levels of PK-tagged Trt1 protein and the chimeric Trt1-Tpz1 fusion proteins. Cdc2 was used as a loading control for total proteins.

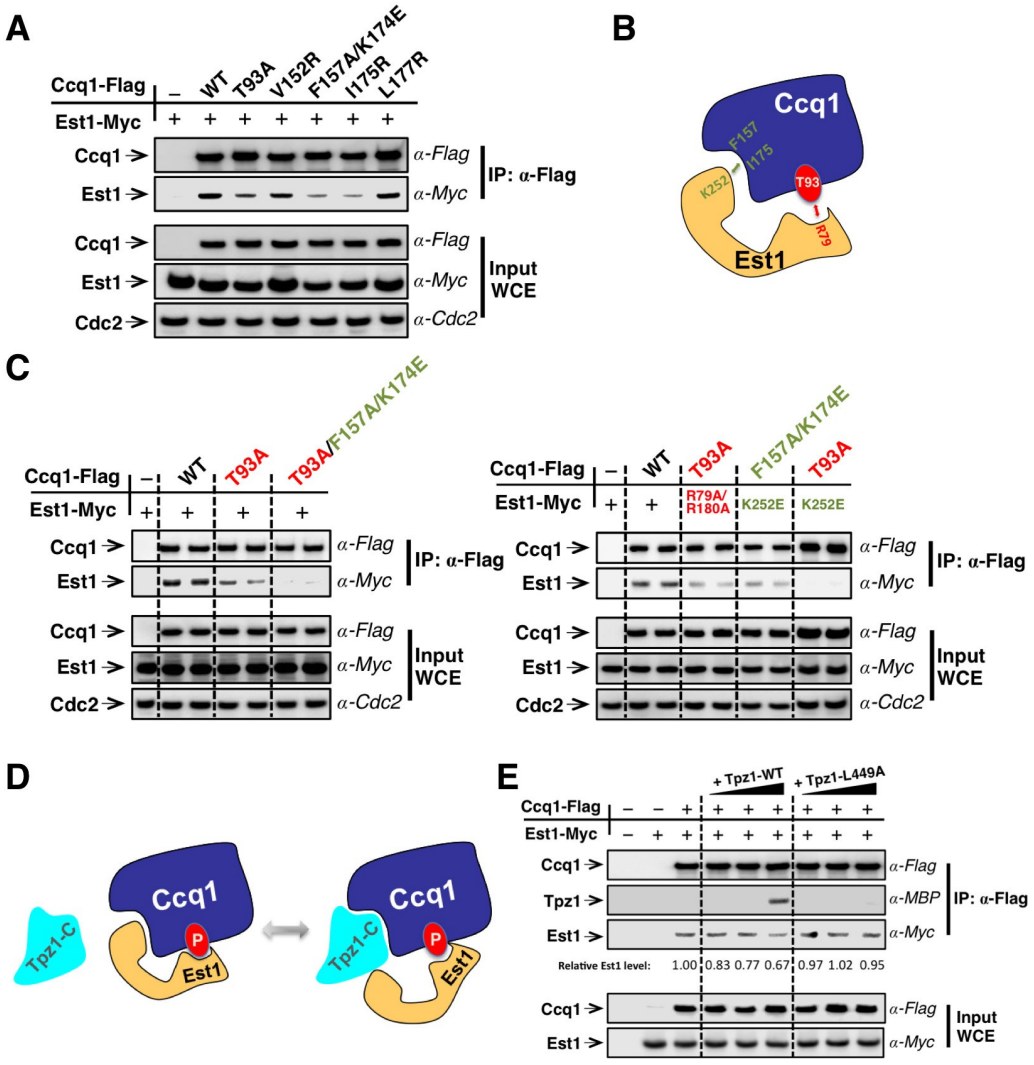

Figure 5. Est1 binds to Ccq1 through two different binding sites. **(A)** Ccq1-Est1 interaction is diminished but not completely disrupted in the *ccq1-T93A*, *ccq1-F157A/K174E*, and *ccq1-I175R* strains as evaluated by Co-IP assays. Cdc2 was shown as the loading control. Input: 1/30 of input WCE. **(B)** Schematic model of Est1 and Ccq1 interaction showing two binding sites for their interaction as further tested in (C). **(C)** Co-IP assays evaluating the contribution of two binding sites to the binding between Est1 and Ccq1. Cdc2 was shown as the loading control. Input: 1/30 of input WCE. **(D)** Schematic model of Tpz1 C-terminal domain, Est1 and Ccq1 forming an intermediate Est1-Ccq1-Tpz1 complex. **(E)** Competitive binding assay showing that Tpz1 can partially compete with Est1 for its interaction with Ccq1; however, the Tpz1-Ccq1 interaction defective mutant Tpz1-L449A cannot.

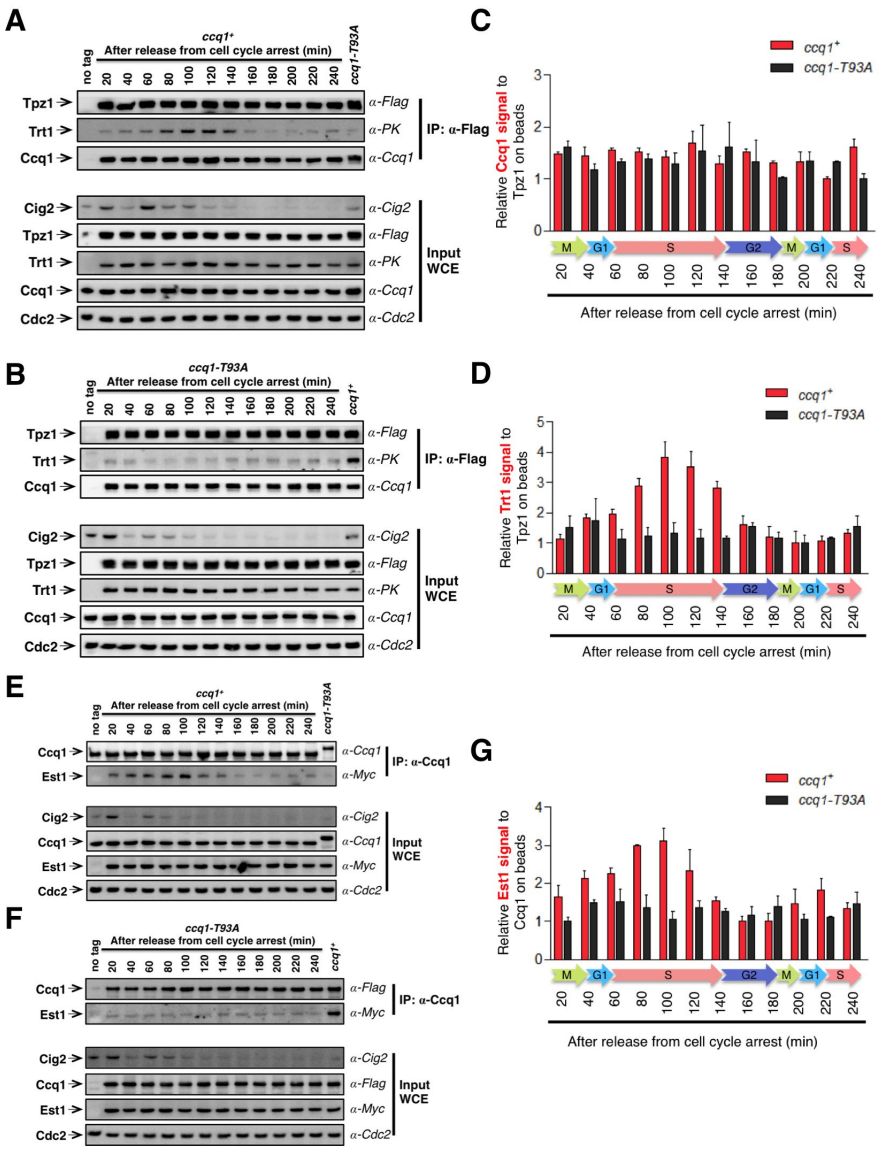

Figure 6. Tpz1-Trt1 interaction is cell cycle-regulated. **(A)** and **(B)** Co-IP assays evaluating the binding efficiency of Tpz1-Trt1 and Tpz1-Ccq1 interactions during cell cycle progression in *ccq1⁺* (A) and *ccq1-T93A* (B) cells. In addition to the indication of time after release from G2 arrest, the levels of S phase cyclin Cig2, which peak at the G1/S boundary and decline to low levels in G2 and M phase, are also shown. Cdc2 was shown as the loading control. Input: 1/30 of input WCE. **(C)** and **(D)** Quantification of the binding efficiency of Tpz1-Trt1 (C) and Tpz1-Ccq1 (D) interactions during cell cycle progression as assayed in (A) and (B). The lowest level of Tpz1-Trt1 (C) or Tpz1-Ccq1 (D) interactions is set to be 1. Plots show mean values ± s.d. for two independent experiments. **(E)** and **(F)** Co-IP assays evaluating the binding efficiency of Ccq1-Est1 interaction during cell cycle progression. As in (A) and (B), in addition to the indication of time after release from G2 arrest, the levels of S phase cyclin Cig2, are also shown. Cdc2 was shown as the loading control. Input: 1/30 of input WCE. **(G)** Quantification of the binding efficiency of Ccq1-Est1 interaction during cell cycle progression as assayed in (E) and (F). The lowest level of Ccq1-Est1 interaction is set to be 1. Plots show mean values ± s.d. for two independent experiments.

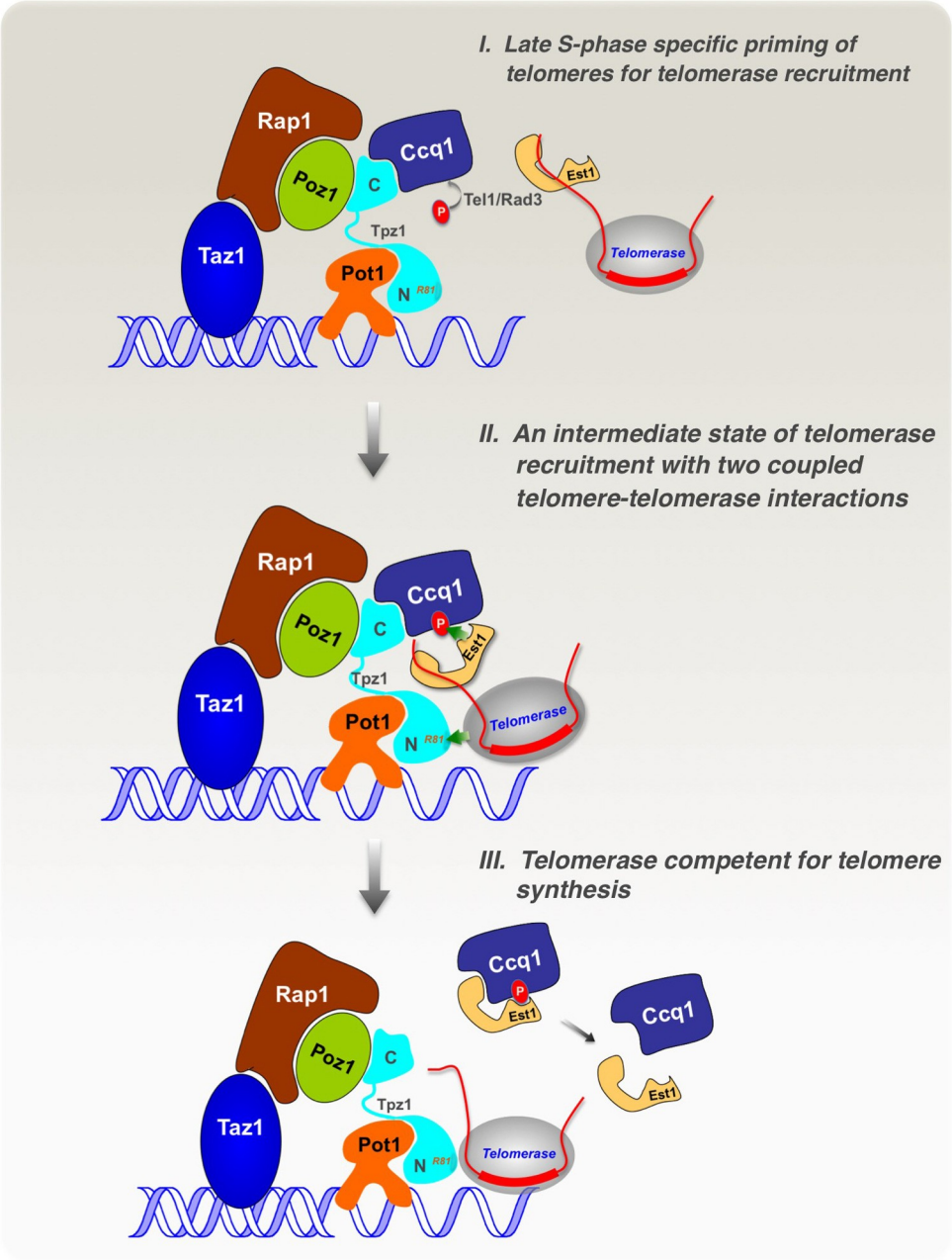

Figure 7. Model of cell cycle-regulated telomerase recruitment via an intermediate state with two coupled telomere-telomerase interactions. A model showing telomerase recruitment in fission yeast through an intermediate state in which Trt1 and Est1 in the telomerase holoenzyme are collaboratively anchored to the telomere via Trt1-Tpz1 TEL patch and Est1-Ccq1 interactions, respectively (illustrated by two green arrows drawn in the middle panel), thereby achieving cell cycle-regulated recruitment of telomerase to telomeres.

CHAPTER 5

Structural Basis for Shelterin Bridge Assembly

Summary

Telomere elongation through telomerase enables chromosome survival during cellular proliferation. The conserved multifunctional shelterin complex associates with telomeres to coordinate multiple telomere activities, including telomere elongation by telomerase. Similar to the human shelterin, fission yeast shelterin is composed of telomeric sequence-specific double- and single-stranded DNA binding proteins, Taz1 and Pot1, respectively, bridged by Rap1, Poz1, and Tpz1. Here, we report the crystal structure of the fission yeast Tpz1$^{475-508}$-Poz1-Rap1$^{467-496}$ complex that provides the structural basis for shelterin bridge assembly. Biochemical analyses reveal that shelterin bridge assembly is a hierarchical process in which Tpz1 binding to Poz1 elicits structural changes in Poz1, allosterically promoting Rap1 binding to Poz1. Perturbation of the cooperative Tpz1-Poz1-Rap1 assembly through mutation of the "conformational trigger" in Poz1 leads to unregulated telomere lengthening. Furthermore, we find that the human shelterin counterparts TPP1-TIN2-TRF2 also assemble hierarchically, indicating cooperativity as a conserved driving force for shelterin assembly.

Introduction

Telomeres are DNA-protein complexes that protect the ends of eukaryotic chromosome from degradation and recognition as DNA damage sites (Palm and de Lange, 2008). Telomere integrity is essential for cell survival and proliferation (Ferreira et al., 2004). Dysfunctional telomeres can initiate genomic instability, cellular senescence, and organismal aging (Batista and Artandi, 2013). Telomeric DNA consists of tandem DNA repeats, which are G-rich in one strand (called the G-strand) and C-rich in the complementary stand (called the C-strand). The G-strand extends beyond the C-strand, forming a single-stranded overhang. The 3' end of the single-stranded overhang acts as the substrate for telomerase—a reverse transcriptase (Nakamura et al., 1997) with its intrinsic RNA as the template—to extend the telomeric DNA (Autexier and Lue, 2006; Collins, 2006; Greider and Blackburn, 1985, 1987). Telomere shortening that is not countered by telomerase activity can directly lead to replicative senescence of cancer cells and prevent them from proliferating indefinitely. Thus, inhibiting telomere elongation, such as via telomerase inhibitors, represents a promising cancer therapeutic strategy (Baerlocher et al., 2015; Harley, 2008; Tefferi et al., 2015).

The basic structure and function of telomeres are conserved among eukaryotes (Palm and de Lange, 2008). A multi-protein complex called shelterin is vital for telomere function. Shelterin acts to regulate telomere elongation by telomerase, and to protect the ends of linear chromosomes from degradation and recognition as DNA damage sites (Artandi and Cooper, 2009; Jain and Cooper, 2010; Palm and de Lange, 2008). In human cells, the shelterin complex consists of double-stranded DNA (dsDNA) binders TRF1 and TRF2, single-stranded DNA (ssDNA) binder POT1, as well as RAP1, TIN2 and TPP1 (de Lange, 2005). Shelterin components connect telomeric dsDNA with ssDNA by forming a

proteinaceous bridge. Specifically, telomeric dsDNA binders TRF1 and TRF2 recruit TIN2 and RAP1 to the telomere; TIN2 then recruits TPP1-POT1 complex to the telomere (Takai et al., 2011). The shelterin architecture in fission yeast, *Schizosaccharomyces pombe*, closely resembles that of mammals (Miyoshi et al., 2008). Its dsDNA binder Taz1 (homolog of hTRF1/2)(Cooper et al., 1997) and its ssDNA binder Pot1 (Baumann and Cech, 2001) are bridged via three other shelterin components, Rap1, Poz1 (hTIN2 homolog), and Tpz1 (Miyoshi et al., 2008). Ccq1, a telomerase recruiter and telomere activator, interacts directly with Tpz1 (shown in Figure 1A) (Hu et al., 2016; Jun et al., 2013; Moser et al., 2011; Webb and Zakian, 2012; Yamazaki et al., 2012).

In telomerase positive cells, such as human embryonic stem cells (Hiyama and Hiyama, 2007), adult germ line cells (Lansdorp, 2005), most cancer cells (Shay and Wright, 1996, 2010), and single-celled eukaryotes—ciliated protozoa and yeasts (Cohn and Blackburn, 1995), telomeres are maintained at a defined species-specific range. Maintaining proper telomere length is critical for normal development and cellular function. While short telomeres lead to defective stem cell development and differentiation, and consequently premature aging diseases, long telomeres help cells gain replicative time to accumulate other mutations (loss-of-function mutations for tumor suppressor and gain-of-function mutations for tumor activator), and thus facilitate tumorigenesis (Bernardes de Jesus and Blasco, 2013; Gunes and Rudolph, 2013). Telomere length homeostasis is controlled through dynamic switching of the telomeres between two states: telomerase-extendible and –nonextendible state, depending on the telomere length (Teixeira et al., 2004). Using *S. pombe* as a model system, we recently discovered that the complete linkage within the shelterin complex, rather than the individual shelterin component *per se*,

regulates the extendibility of telomeres by telomerase (Jun et al., 2013; Liu et al., 2015). The importance of the shelterin linkage in regulating telomere state was further emphasized by the ability of an artificial linker, instead of shelterin components, to maintain wild-type telomere length (Pan et al., 2015). Disruption of the shelterin linkage leads to unregulated telomere elongation, emphasizing the critical role of shelterin complex assembly in telomere length regulation. However, the structural basis and the mechanistic principle underlying shelterin assembly remain largely unknown (Scott et al., 2017).

In this study, we solved crystal structures at up to 2.3Å resolution of the fission yeast Tpz1$^{475-508}$-Poz1-Rap1$^{467-496}$ complex that provide atomic-level views of shelterin bridge assembly. Importantly, we find that shelterin bridge assembly is a hierarchical process in which Tpz1 binding to Poz1 induces the conformational change of Poz1 through the Poz1 N-terminal helix—the "conformational trigger", and consequently enables high affinity binding of Rap1 to Poz1. Furthermore, perturbation of the cooperative Tpz1-Poz1-Rap1 assembly by mutating the "conformational trigger" in Poz1 leads to unregulated telomere lengthening, signifying the importance of optimal shelterin bridge assembly in telomere length regulation. Extending our findings to humans, we find that human shelterin bridge TPP1-TIN2-TRF2 also assembles in a similar hierarchical manner, indicating cooperativity as a conserved driving force for shelterin assembly to accurately regulate telomere length homeostasis.

RESULTS

Tpz1-Poz1 interaction promotes Poz1-Rap1 interaction

To elucidate the assembly mechanism of the shelterin bridge Tpz1-Poz1-Rap1 complex (Figure 1A), we first broke the assembly down to elementary steps of individually characterizing Tpz1-Poz1 and Poz1-Rap1 binary interactions. To this end, we cloned, expressed, and purified $Tpz1^{475-508}$ (C-terminal Poz1 binding domain)(Jun et al., 2013), $Rap1^{446-523}$ (Poz1 binding domain), and full length Poz1 to homogeneity. Upon obtaining recombinant $Tpz1^{475-508}$, Poz1, and $Rap1^{446-523}$, we measured the binding affinities of $Tpz1^{475-508}$-Poz1 and Poz1-$Rap1^{446-523}$ interactions by utilizing isothermal titration calorimetry (ITC). We determined the disassociation constant (K_d) of $Tpz1^{475-508}$-Poz1 interaction to be 0.94 μM and the K_d of Poz1-$Rap1^{446-523}$ interaction to be 5.62 μM (Figures 1B and 1C). Surprisingly, when we measured the binding affinity between $Rap1^{446-523}$ and $Tpz1^{475-508}$-Poz1 complex, our ITC measurement indicates that the K_d became 480 nM (Figure 1D), about 10 times stronger than that of free Poz1 to $Rap1^{446-523}$. Indeed, in an independent GST-pulldown assay, we found that GST-Rap1 can bind to as low as 3 μM Tpz1-Poz1 complex efficiently, whereas 30 μM of free Poz1 is required to achieve the same level of binding (Figure 1E). Therefore, the presence of Tpz1 enhanced Poz1-Rap1 interaction, indicating that Tpz1 binding to Poz1 confers positive cooperativity for the Poz1-Rap1 interaction, ensuring that the whole Tpz1-Poz1-Rap1 complex is more stable than the sum of its parts. Moreover, real time binding kinetics analysis using Bio-Layer Interferometry (BLI) reveals that while the association rate (k_{on}) of Rap1 binding to free

Poz1 is about 5 times faster than that of Rap1 to Tpz1-bound Poz1, the disassociation rate (k_{off}) of Rap1 binding to Tpz1-bound Poz1 complex is approximately 60 times slower than that of Rap1 binding to free Poz1 (Figures 1F and 1G). These results indicate that Tpz1-bound Poz1 "locks" Rap1 into the stable trimeric Tpz1$^{475\text{-}508}$-Poz1-Rap1$^{446\text{-}523}$ shelterin bridge. In addition, BLI also shows similar levels of binding affinity (K_d) to the ITC measurements for Poz1-Rap1, Tpz1-bound Poz1-Rap1 (Figures 1F and 1G), and Tpz1-Poz1 interactions (Figure S1). In summary, based on the above binding thermodynamics and kinetics results, we conclude that the Tpz1$^{475\text{-}508}$-Poz1-Rap1$^{446\text{-}523}$ complex assembles in a cooperative manner as shown in Figure 1H.

Crystal structure of the Tpz1-Poz1-Rap1 complex

Our finding that Tpz1-Poz1 interaction promotes the binding of Rap1 to Tpz1-bound Poz1, forming the shelterin bridge suggested two possible mechanisms to achieve this cooperativity. First, the association of Tpz1 with Poz1 might together create a novel composite binding site for Rap1. Alternatively, binding of Tpz1 to Poz1 could induce allosteric changes that create a high affinity Rap1 binding site. To distinguish these two possibilities and provide an atomic view of the shelterin bridge, we decided to determine the crystal structure of the Tpz1-Poz1-Rap1 complex. To facilitate the crystallization of Tpz1-Poz1-Rap1 complex, we first mapped the Rap1 region that is both necessary and sufficient for its binding to Tpz1-Poz1 (Figure S2A). A number of combinations of Tpz1, Poz1, and Rap1 constructs were trialed for crystallization of the complex, and finally Tpz1$^{475\text{-}508}$-Poz1-Rap1$^{467\text{-}496}$ produced high quality crystals. With these crystals, we

determined the crystal structure of Tpz1$^{475-508}$-Poz1-Rap1$^{467-496}$ complex using SAD (single-wavelength anomalous dispersion) at 2.3Å resolution (Table 1). As shown in Figure 2A, the Tpz1$^{475-508}$-Poz1-Rap1$^{467-496}$ complex forms a dimer in the crystal, showing a compact, butterfly-shaped structure, consisting mainly of α-helices. Two Poz1 molecules, each containing 11 α-helices, build the "body" and the "wings" of the butterfly with two Tpz1 molecules standing out as the "antennas". Each Rap1 molecule lies around the edge of the butterfly "wing". Helices α1 and α2 from each Poz1 interact with each other in an anti-parallel manner, forming the dimer interface of the complex, analogous to the "body" part of the butterfly. The dimerization interface is composed of 11 residues from α1 and α2, covering 707.2 Å^2 surface area (Figure S2B). In accordance with the dimer observed in the crystal structure, Tpz1$^{475-508}$-Poz1-Rap1$^{467-496}$ complexes were eluted at the dimer position when purified by the gel-filtration chromatography (Figure S2C) and were determined to have dimer mass by size-exclusion chromatograph-multi-angle light scattering (SEC-MALS) in solution (Figure S2D). The rest 8 α-helices (α3-α11) of Poz1 are arranged into a multi-helix bundle, resembling the butterfly "wing". Importantly, it is evident that Tpz1 and Rap1 bind to distinctively different locations on Poz1, and no direct contact is observed between Tpz1$^{475-508}$ and Rap1$^{467-496}$, supporting the allosteric mechanism.

In the Tpz1$^{475-508}$-Poz1-Rap1$^{467-496}$ complex, Tpz1$^{475-508}$ adopts a helix-turn-helix structure and inserts its longer helix into the concave formed by helices α2, α3, α4, and α5 of Poz1 (Figures 2B and 2C). The interaction between Tpz1 and Poz1 involves an extended hydrophobic core composed of four hydrophobic residues from Tpz1, Phe491, Leu494, Trp498 and Ile501, intertwining with a number of hydrophobic residues on Poz1. Specifically, Phe491 and Leu494 of Tpz1 sit in a pocket formed by Leu38, Leu41, Met47,

Met52, Met56 and Phe60 of Poz1. The aromatic ring of Trp498 in Tpz1 interacts with that of Tyr63 in Poz1 via π-π stacking. In addition, Trp498 also has hydrophobic interactions with Phe18, Tyr24, Met26, Leu38 and Tyr63 of Poz1. Tpz1-Ile501, a previously identified key residue for Tpz1-Poz1 interaction (Jun et al., 2013), is surrounded by Phe60, Tyr63, and Cys64 from α4, together with Leu90 and Leu95 from α5 of Poz1. Therefore, the four hydrophobic residues from Tpz1 mimic "key teeth", sticking into the shape-complemented convex formed by hydrophobic residues of Poz1 (Figure S2E). Around the hydrophobic interior, there are a number of salt bridges formed between Tpz1 and Poz1, for example, Asp497 of Tpz1 with Asn98 and Arg102 of Poz1, Lys500 of Tpz1 with Glu92 of Poz1, Glu502 of Tpz1 with Ser31 and Asn35 of Poz1, and Arg505 of Tpz1 with the backbone C=O groups of Poz1 Tyr63 and Gln88 (Figures 2B, 2C, and S2F). Interestingly, we also observed a Zn ion existing at the Tpz1-Poz1 interface, coordinated by Cys479, Cys482, His488 of Tpz1, and His49 of Poz1 with a tetrahedral conformation (Figure 2C).

On the opposite side of the Tpz1 binding region in the Tpz1$^{475\text{-}508}$-Poz1-Rap1$^{467\text{-}496}$ complex, Rap1 exists in an extended conformation and packs into a long groove in Poz1 created by its helices α8, α9, and α10 turning around helix α6 (Figures 2D and 2E). Rap1 interacts with Poz1 in an unusual way, consisting of two separate hydrophobic cores that anchor Rap1 to Poz1, burying a total of 918Å of solvent-accessible area of each protein. In the first hydrophobic core, Ile470, Phe471, Val472, Leu478 and Ile480 from Rap1 have extensive hydrophobic interactions with Leu128, Leu133, Leu140, Cys143, Ala146, Phe212, Val215, Cys222, and Leu225 of Poz1. The second hydrophobic core is built by Leu483 of Rap1, interacting with Ala184, Leu185, and Tyr199 of Poz1. Located in between these two hydrophobic cores is a region of Poz1 carrying overall positive surface potential (Figure

S2G). In fact, specific recognition of Rap1 by Poz1 is aided by multiple hydrogen bonds formed between the backbone of Rap1 and of Poz1 with side chains from α6 (Glu136 and Arg150) and α10 (Lys211 and Arg218) in this mostly positively charged region of Poz1. In addition, a salt bridge is also observed between side chains of Rap1-Glu476 and Poz1-Arg218. Lastly, an aromatic-thiol π-type H-bond between Cys222 of Poz1 and Phe471 of Rap1 is formed in the Rap1-Poz1 interface (Figure 2D).

Taken together, based on the crystal structure of the Tpz1$^{475-508}$-Poz1-Rap1$^{467-496}$ complex, Tpz1 does not provide any additional binding surface for Rap1 and is located in a distinctively different site on Poz1 from Rap1. Thus, Tpz1-Poz1 interaction most likely triggers allosteric changes in Poz1 that lead to the formation of the high affinity Rap1 binding groove.

Biochemical and functional analyses of the Tpz1-Poz1 interface

To validate the observed interaction interface between Tpz1 and Poz1 in the crystal structure, we first employed GST-pulldown assays to evaluate the binding of a panel of mutants targeting interface residues in Poz1. Interestingly, Poz1 single mutations of residues in the interface at most weakened, but did not disrupt Tpz1-Poz1 interaction (Figure 3A). However, a double mutant Poz1-C64D/L95R completely abolished Tpz1-Poz1 interaction in the GST-pulldown assay (Figure 3A). This is reminiscent of what we observed previously for the Tpz1 mutants targeted to disrupt Tpz1-Poz1 interaction, in which only a double-mutant of the Tpz1-Poz1 interface residues, Tpz1-I501A/R505E, completely disrupted Tpz1$^{406-508}$-Poz1 interaction (Jun et al., 2013). This result indicates

that the forces mediating Tpz1-Poz1 interaction along the interface are rather independent of each other, and therefore only combined mutations at different contact sites can lead to complete loss of Tpz1-Poz1 interaction. Furthermore, using coimmunoprecipitation, we confirmed that mutations abrogating Tpz1$^{406-508}$ and Poz1 interaction in vitro also disrupted the interaction between the full length Tpz1 and Poz1 (Figure S3A). In addition, these Poz1 mutants defective in Tpz1 binding also are unable to interact with Rap1, suggests that, in cells, disturbing the Poz1-Tpz1 interface inhibits Poz1-Rap1 interaction. These results further support the proposed allosteric effect of Tpz1 on Poz1 being required for the formation of shelterin bridge Tpz1-Poz1-Rap1 complex.

Next, we aimed to evaluate the functional outcome of disrupting Tpz1–Poz1 interaction by the *poz1*$^{+}$ mutant in telomere maintenance, we made a panel of *S. pombe* strains with the same set of Poz1 mutations as those in the binding assays. Among them, only *poz1-C64D/L95R* mutant cells had dramatically elongated telomeres, similarly to those of the previously characterized *tpz1*$^{+}$ mutant *tpz1-I501R/R505E* defective in Tpz1-Poz1 interaction (Figure 3B). Together with our previous studies, this result not only validates the physiological relevance of the Tpz1-Poz1 interface observed in the crystal structure, it also reconfirms the importance of the integrity of the shelterin bridge in proper telomeric state regulation.

Biochemical and functional analyses of the Poz1-Rap1 interface

We further assessed the extended Poz1-Rap1 interaction interface by mutational scanning of Rap1 residues interface based on the Tpz1$^{475-508}$-Poz1-Rap1$^{467-496}$ crystal

structure. We then utilized GST-pulldown assay to evaluate the binding efficiency between Rap1 mutants and Poz1-Tpz1 complex *in vitro*. As expected, Rap1 point mutations of residues comprising each of the two hydrophobic interaction cores, with I470R, F471A, V472R, L478R, and I480R targeting the first, and L483R targeting the second, were able to completely disrupt Rap1$^{446\text{-}512}$-Poz1 interaction (Figure 3C). Moreover, Rap1-E476R, a mutant that disrupts a salt bridge between Rap1-Glu476 and Poz1-Arg218, also leaded to loss of Rap1-Poz1 interaction (Figure 3C). Correspondingly, Poz1 point mutations that either compromise the hydrophobic interaction core (C143D and F212A) or disrupt the salt bridges (K139E, R150E, and R218E) were also able to fully disrupt or severely weaken Poz1-Rap1 interaction (Figure 3D). Our co-immunoprecipitation assays also confirmed the abrogation of full-length Poz1-Rap1 interaction caused by the same panel of Rap1 and Poz1 mutants (Figures S3B and S3C). Different from Tpz1-Poz1 interface, Poz1-Rap1 interaction appears to be mediated cooperatively by multiple hydrophobic interactions and salt bridges, and as a result, disruption of any one of these forces leads to the complete break down of the interaction.

Similarly, to test the in vivo consequence of the Poz1-Rap1 interaction in telomere length maintenance, we generated yeast strains carrying the same set of *rap1*$^{+}$ or *poz1*$^{+}$ point mutations as those used in the binding assays. Along the extended Poz1-Rap1 interaction interface, the disruption of the core residues in the hydrophobic patches of Rap1 (*rap1-I470R*, *rap1-F471A*, *rap1-L478R*, *poz1-C143D*) and residues forming a salt bridge (*rap1-E476R* and *poz1-R218E*) (Figures 3E and 3F) resulted in unregulated telomere elongation, similar to the *poz1Δ* strain. Moreover, other mutants that weakened Poz1-Rap1 interaction also caused telomere elongation to different degrees, in accordance with the

severity of Poz1-Rap1 interaction defect. Taken together, these results functionally verified Poz1-Rap1 interface structure and signify its role in telomere length regulation.

Tpz1 binding induces the folding of the N-terminal helix α1 of Poz1

To elucidate the mechanism by which Tpz1-Poz1 interaction enhances Poz1-Rap1 interaction, we aimed to probe the possible conformational changes in Poz1 upon its binding to Tpz1. We thus carried out a limited proteolysis assay to probe the protein flexibility of free Poz1 and Tpz1-bound Poz1. As shown in Figure 4A, the Poz1-Tpz1 complex was trypsin proteolysis-resistant whereas Poz1 alone was proteolyzed to a lower molecular weight product. Mass spectrometry sequencing of the lower molecular weight band identified it as Poz1 missing its N-terminal helix α1, denoted as Poz1*ΔN*. Therefore, the binding of Tpz1 to Poz1 is likely to induce the folding of the flexible N-terminal helix α1. To further understand the folding process of Poz1 helix α1 upon Poz1 binding to Tpz1, we employed amide hydrogen/deuterium exchange detected by mass spectrometry (HXMS) to probe the solvent accessibility of amide protons, enabling comparison of the folded states of free Poz1 and Tpz1-bound Poz1 (Balasubramaniam and Komives, 2013). The exchange rates of amide protons measured by HXMS vary from milliseconds for amides in unstructured peptides to days for amides in cores of globular proteins. As shown in Figure 4B, pepsin digestion of both free Poz1 and Tpz1-bound Poz1 yielded 34 peptides that cover 75% of the Poz1 sequence. Poz1 appears to have a wide range of different exchange properties, much of it is exchanging nearly all of its amides (Figure S4A), and then, there are a few regions that exchange very little (Figure S4B). Interestingly, whereas most

regions in Poz1 have similar exchange in its free and Tpz1-bound forms, there are three regions that show distinctly decreased exchanges, and two regions that show moderately decreased exchanges upon Tpz1 binding to Poz1 (Figures 4B and 4C). Among these five regions, the most dramatic one is a peptide covering residues 12 to18, representing the 2nd half of helix α1 (Figures 4B and 4C). In the free form, this part of Poz1 readily exchanges almost all of its amide protons for deuterons, suggesting the unstructured nature of this region (Figure 4D). However, this exchange dramatically reduces upon Tpz1 binding to Poz1 (Figure 4D), indicating that helix α1 becomes folded when bound to Tpz1. This HXMS result is highly correlated with the crystal structure of Tpz1$^{475\text{-}508}$-Poz1-Rap1$^{467\text{-}496}$ complex, in which α1 of Poz1 is packed against α2, α3, and α4. Accordingly, another peptic peptide with decreased exchange rate in Tpz1-bound Poz1 covers residues 37 to 55 (Figure 4E), which includes the end of α2, α3, and the very beginning of α4—all closely contacting the newly formed α1 upon Tpz1 binding (Figure 4C). Amide proton exchange is also sensitive to changes in protection at the binding interface. From the crystal structure, we can see that Tpz1 interacts with the other side of α2, α3, and α4 region, together with α1 contributing to the decreased exchange. In addition, another contact side for Tpz1 in Poz1, located at the very end of α5 consisting of residues 93-100, also shows less deuterium incorporation when Tpz1 is bound to Poz1 (Figure 4F). In two more distal regions from the Tpz1 binding site of Poz1, covering residues 138-140 and 185-202, moderate levels of decrease in deuterium incorporation were also observed (Figures S4C and 4G). These two regions fall into the Rap1 binding site of Poz1, based on the crystal structure of the Tpz1$^{475\text{-}508}$-Poz1-Rap1$^{467\text{-}496}$ complex (Figures 2D and 2E). These results directly demonstrate the allosteric structural changes in the Rap1 binding region of Poz1 induced by the binding of

Tpz1 to Poz1. Therefore, our limited proteolysis and HXMS experiments both suggest that Tpz1 binding to Poz1 prompts the conformational changes in Poz1, which includes the folding of its N-terminal helix and other structural changes propagated from it, and results in high-affinity binding to Rap1.

We next asked whether the induced folding of Poz1 N-terminal helix α1 upon Tpz1-Poz1 interaction is required for the enhanced Poz1-Rap1 interaction. Consistent with this hypothesis, our ITC data indicated that Poz1*ΔN* ($Poz1^{29-249}$), even in the presence of Tpz1, interacts with Rap1 with K_d of 4.58 μM (Figure 4H), similar to that of Poz1-Rap1 interaction without Tpz1 (K_d= 5.62 μM). Moreover, our real time binding kinetics analysis using BLI indicated that the binding kinetics (k_{on} and k_{off}) of the interaction between Rap1 and Tpz1-bound Poz1*ΔN* is very similar to that of Rap1 and free Poz1*ΔN* (Figure S4D and S4E). Therefore, given that the crystal structure of the $Tpz1^{475-508}$-Poz1-$Rap1^{467-496}$ complex clearly shows that Rap1 binds to the C-terminal, instead of the N-terminal region of Poz1 where Tpz1 binds, the N-terminal helix α1 most likely acts as a "conformational trigger", allosterically promoting Poz1 binding to Rap1 upon Tpz1-Poz1 interaction.

Structural basis for the allosteric promotion of Poz1-Rap1 interaction via the "conformational trigger"

Given the importance of the N-terminal helix α1 of Poz1 in stimulating Tpz1-bound Poz1 to interact with Rap1, we decided to elucidate the structural basis for the allosteric changes in Poz1 that enhance Poz1-Rap1 interaction via the "conformational trigger". To achieve this goal, we solved the crystal structure of the $Tpz1^{475-508}$-Poz1*ΔN* complex,

which enables the structural comparison of that to Tpz1$^{475\text{-}508}$-Poz1 structure in the Tpz1$^{475\text{-}508}$-Poz1-Rap1$^{467\text{-}496}$ complex. As shown in Figure 5A, Tpz1$^{475\text{-}508}$-Poz1*ΔN* forms a dimer of heterodimers. However, different from the dimer interface in Tpz1-Poz1, helices α2 from two Poz1*ΔN* molecules interact with each other in a "domain swapped" manner, mediating the dimerization of Tpz1$^{475\text{-}508}$-Poz1*ΔN* complex. Our SEC-MALS measurement also indicated the dimer formation of Tpz1$^{475\text{-}508}$-Poz1*ΔN* complex in solution (Figure S5A). Based on the structure superposition (Figure 5B), the "conformational trigger"—N-terminal helix α1 of Poz1 imparts the movement of helix α2 towards Tpz1, which consequently induces the rotation of the side chain of Tpz1-Trp498, resulting its packing against the side chain of Poz1-Leu38. In addition, folding of helix α1 creates new hydrophobic packing in Poz1 composed of Leu14, Phe18, Tyr24, Phe55, and Met56, providing structural explanations for the HXMS results. As demonstrated in a movie (Supplemental Movies 1 and 2) based on the structures of the low-affinity and high-affinity Poz1, mostly likely due to the induced folding of α1 in Poz1 upon Tpz1 binding, α1 forms new hydrophobic packing with α4 and Glu21 in the loop connecting α1 and α2 forms hydrogen bonding with Gln221 in α10 (Figure 5C), which in turn trigger structural rearrangements in helices α6, α7, α8, and α9 to various degrees (Figures 5D and 5E). These Tpz1 binding-induced allosteric structural changes in Poz1 result in a more open binding groove for Rap1 (Figures S5B and S5C).

The "conformational trigger" in Poz1 is essential for shelterin assembly and telomere length regulation

To assess the contribution of the "conformational trigger" in Poz1 to telomere maintenance, we introduced either Poz1 N-terminal deletion (*poz1-ΔN*) or several point mutations in helix α1 (*poz1-R6E, poz1-L14R,* and *poz1-F17A*) to *S. pombe* cells. Both *poz1-ΔN* and *poz1-L14R* strains had dramatically elongated telomeres, whereas *poz1-R6E* and *poz1-F17A* strains had wild-type telomere length (Figure 6A). From the crystal structure of Tpz1$^{475\text{-}508}$-Poz1-Rap1$^{467\text{-}496}$ complex, Leu14 in Poz1 α1 helix participates in the formation of the new hydrophobic packing against Leu38, Leu41 in α2, and Met56 in α4 (Figure S6A), and therefore, L14R mutation is most likely to disrupt the allosteric pathway that conveys Tpz1-Poz1 interaction-induced structure changes to the Rap1-binding region of Poz1. In contrast, residues Arg6 and Phe17 both point away from the new hydrophobic core (Figure S6A), and therefore mutations of them have little effect on the "conformational trigger" function of α1 helix in Poz1. Consistent with our structural analysis and the telomere elongation phenotype of *poz1-L14R* strain, the binding affinity of Tpz1-bound Poz1-L14R interacting with Rap1 is the same as that of the free Poz1-Rap1 interaction (Figure 6B), similar to that of Tpz1-Poz1*ΔN* and Rap1 interaction (Figures 4H and S4C). In addition, the ~60-fold slower k_{off} observed in the association of Rap1 with Tpz1-Poz1 complex than that of Rap1 with free Poz1 was not detected when L14R mutation was introduced to the Tpz1-Poz1 complex (Figure 6B). Interestingly, in our co-immunoprecipitation assays, we observed full abrogation of Poz1-Rap1 interaction in both *poz1-ΔN* and *poz1-L14R* cells, whereas Rap1-Taz1 interaction was maintained at the wild-type level (Figure 6C). The protein levels of Poz1 were unchanged. To our surprise, in both *poz1-ΔN* and *poz1-L14R* cells, Tpz1-Poz1 interaction is also decreased about 3-fold, while Tpz1-Ccq1 interaction is still at the wild-type level in both mutant cells (Figure 6D). Our in vitro binding assays

utilizing both BLI and ITC with purified recombinant proteins indicate that the binding affinity between Tpz1 and Poz1*ΔN* is similar to that of Tpz1 and wild-type Poz1 (Figures S6B and S6C).

To investigate the contribution of the "conformational trigger" in Poz1 to shelterin assembly on telomeres, we carried out Chromatin Immunoprecipitation (ChIP) analysis to investigate how Poz1 N-terminal deletion or mutation affects the telomeric localizations of Poz1 itself and other shelterin components. Whereas *poz1-ΔN* and *poz1-L14R* mutations only moderately decreased the telomeric localization of Rap1 (Figures 6E), these two mutations drastically diminished the enrichment of both Poz1 (Figure 6F) and Tpz1 (Figure 6G) on telomeres, indicating the critical role of the "conformational trigger" in Poz1 and the cooperativity it generates in promoting proper shelterin assembly on telomeres. For Tpz1, telomeric localization is still observed in both *poz1-ΔN* and *poz1-L14R* cells (Figure 6G); however, its enrichment along the elongated telomeres in these two mutant cells is low. The most likely explanation for this result is that Tpz1 is still recruited to telomeric G-overhang through Pot1, but the defective Tpz1-Poz1-Rap1 complex assembly in *poz1-ΔN* or *poz1-L14R* cells (Figure 6D) diminishes the recruitment of Tpz1 from the double-stranded telomeric DNA via Taz1-Rap1 interaction.

Cooperativity is a conserved driving force for human shelterin assembly

Fission yeast shelterin is architecturally conserved to its human counterpart (Figure S7A). In both species, single-stranded telomeric DNA binding complex—Tpz1/Pot1 in fission yeast and TPP1/POT1 in humans, is connected to telomeric duplex DNA binders—

Taz1/Rap1 in fission yeast and TRF1/2/RAP1 in humans. Poz1 mediates the linkage in fission yeast by binding directly to Tpz1 and Rap1, whereas TIN2 links TPP1 to TRF2-RAP1 complex as well as to TRF1. We speculated whether there is a region existing in TRF2 equivalent to the Poz1-binding domain of fission yeast Rap1. We thus aligned the previously identified TIN2 binding domain of mammalian TRF2 to the Poz1-binding domain of fission yeast Rap1. Consistent with our speculation, we found significant conservation between these two regions from such diverged eukaryotes (Figure S7B). Moreover, based on the crystal structure of the Tpz1-Poz1-Rap1 complex, most of the conserved residues in Rap1 directly mediate the Rap1-Poz1 interaction. Next, we tested whether human TPP1-TIN2 interaction also enhances TIN2-TRF2 interaction, as fission yeast Tpz1-Poz1 interaction does to Poz1-Rap1 interaction. As shown in Figure 7A, our ITC measurements indicated that $TRF2^{382-424}$ binds to free TIN2 with a K_d of 3.11 μM, but it binds to $TPP1^{486-544}$-bound TIN2 with a K_d of 0.18 μM (Figure 7B), an 18-fold increase of binding affinity. Accordingly, our GST-pulldown assay also demonstrated that GST-$TRF2^{42-446}$ binds to as low as 1 μM $TPP1^{486-544}$-bound TIN2 efficiently, whereas 30 μM of free TIN2 is required to achieve similar level of binding (Figure S7C). Similar binding enhancement of TIN2-$TRF2^{382-424}$ interaction by $TPP1^{486-544}$ was also observed in vivo (O'Connor et al., 2006). Evidently, human shelterin bridge TPP1-TIN2-TRF2 also assembles in a similar hierarchical manner as its fission yeast counterpart, signifying cooperativity as a conserved driving force for shelterin assembly.

Discussion

The mechanism of hierarchical shelterin bridge assembly

Recent progress in dissecting the subunit interactions in the shelterin bridge and elucidating their functions has allowed a better understanding of how the shelterin complex acts to regulate telomere length homeostasis. The core of fission yeast shelterin is formed by a three-protein complex, consisting of Tpz1, Poz1 and Rap1 (Jun et al., 2013; Miyoshi et al., 2008; Pan et al., 2015). The Tpz1-Poz1-Rap1 complex has emerged as a key regulatory element of telomere synthesis by telomerase, based on its ability to bridge telomeric G-overhang binding protein Pot1 to the telomeric duplex DNA binding protein Taz1. Thus, key questions to understand telomere length control have been the shelterin bridge architecture, the molecular mechanism of the bridge formation, and the nature of shelterin assembly at telomeres. Our biochemical, structural and functional analyses of the Tpz1-Poz1-Rap1 complex presented in this study reveal the hierarchical assembly of the shelterin bridge. This hierarchical assembly is enabled by the binary conformational change of Poz1 induced by Tpz1-Poz1 interaction, as illustrated in crystal structures of both the low and the high affinity Rap1-binding modes of Poz1. Our characterizations of the cooperative shelterin bridge assembly at the atomic-level coupled with in vivo functional analyses allow us to propose a model for shelterin assembly at telomeres. As depicted in Figure 7C, in fission yeast, Taz1 binds to telomeric dsDNA via its Myb DNA binding domain, which in turn recruits Rap1 through protein-protein interaction. At the single-stranded G-overhang, about 30 nucleotides in length for *S. pombe*, Pot1 localizes to this region via the interaction between its N-terminal OB-fold domain and the G-overhang (Baumann and Cech, 2001; Erdel et al., 2017; Lei et al., 2003). The association of Tpz1 with

Pot1 has been shown to increase the binding affinity with G-overhang ~10-fold (Nandakumar and Cech, 2012). Poz1 can be targeted to telomeres through its interaction with Tpz1, which triggers conformational changes in Poz1 thus making it bind to Rap1 with high affinity (Route I). As a result, a stable shelterin bridge linking telomeric dsDNA and ssDNA is formed via this step-wise, hierarchical assembly process, enforcing negative regulation on telomerase-mediated telomere elongation. On the other hand, Poz1 can also associate with chromatin-free Tpz1-Pot1 complex in the nucleus, turning into high-affinity Rap1 binding mode. Then, the Poz1-Tpz1-Pot1 complex is targeted to telomeres through associating with the Taz1-Rap1 complex located at telomeres (Route II).

Structural features of the shelterin bridge

The crystal structure of the Tpz1$^{475-508}$-Poz1-Rap1$^{467-496}$ complex, determined at a resolution of 2.3 Å, represents the atomic structure of the shelterin bridge, a significant step forward in mechanistic understanding of shelterin functions. The binding of Tpz1 to Poz1 induces the folding of the critical "conformational trigger", N-terminal helix α1 of Poz1, and the consequent structural changes propagated to the Rap1 binding region of Poz1. Both Tpz1-Poz1 and Rap1-Poz1 interaction interfaces appear to be uniquely tailored for the cooperative assembly process. Cooperativity ensures that the whole complex is more stable than the sum of its parts (Williamson, 2008) and our crystal structures illustrate the structural basis for the cooperative assembly. The interaction between Tpz1 and Poz1 relays on a wide and continuous hydrophobic interface. This strong and stable hydrophobic interaction induces committed structure changes in Poz1, including those at

its Rap1 binding sites. Our HXMS analysis revealed a high degree of plasticity in free Poz1, which facilitates its conformational changes immediately upon Tpz1 binding. The structure comparison of the low-affinity and the high-affinity Rap1-binding states of Poz1 further reveals the detailed allosteric structural changes of Poz1 upon its binding to Tpz1. It also highlights the critical role of Poz1 helix α1—the "conformational trigger" in promoting structural changes in Poz1 and in regulating shelterin bridge assembly. On the other hand, Rap1-Poz1 interaction interface adopts a uniquely long and narrow shape, most likely to allow efficient sensing of the altered structural elements in Poz1 by Rap1. It is worth noting that there are two rather separated hydrophobic cores mediating Rap1-Poz1 interaction. Further specificity is provided by hydrogen bonding between the backbone of Rap1 and several side chains from Poz1. These structure features may facilitate the modular recognition of allosteric changes in Poz1 and thus achieve effective coupling of Tpz1-Poz1 binding to Poz1-Rap1 binding to form a stable shelterin bridge.

Implications for the regulation of telomere elongation

Previous studies supports the model that the shelterin bridge between the double-stranded and single-stranded telomeric DNA is critical for maintaining telomere length by controlling the telomere state and by regulating the accessibility of telomerase to telomeres (Jun et al., 2013; Pan et al., 2015). Accurate and stable shelterin bridge assembly is essential for this important shelterin function. Our work reported here provides the atomic-level structural view of the shelterin bridge and its cooperative assembly mechanism. The cooperativity ensures that the binding between shelterin components is

connected through the structure, which warrants that the whole Tpz1-Poz1-Rap1 complex is more stable than the sum of its parts, thereby driving the complex assembly, in a similar manner as many other macromolecular complexes, such as ribosome (Mizushima and Nomura, 1970; Talkington et al., 2005). On the other hand, the cooperative mechanism also enables rapid disassembly of the shelterin bridge by disrupting a key element in the complex assembly, and thus to achieve timely switching from telomerase-non-extendible to -extendible state of telomere. Indeed, our co-immunoprecipitation assays show that either a mutation in or a deletion of the "conformational trigger" in Poz1 leads to a greater degree of disruption of Tpz1-Poz1-Rap1 complex than it causes in binding assays (ITC or BLI) using the purified recombinant proteins. Since co-immunoprecipitation monitors interactions between endogenous proteins in the cell, which can bear regulatory posttranslational modifications (PTMs), it is possible that loss of the "conformational trigger" in Poz1 elicits PTMs on Poz1, which further inhibit Poz1-Rap1 and Poz1-Tpz1 interactions.

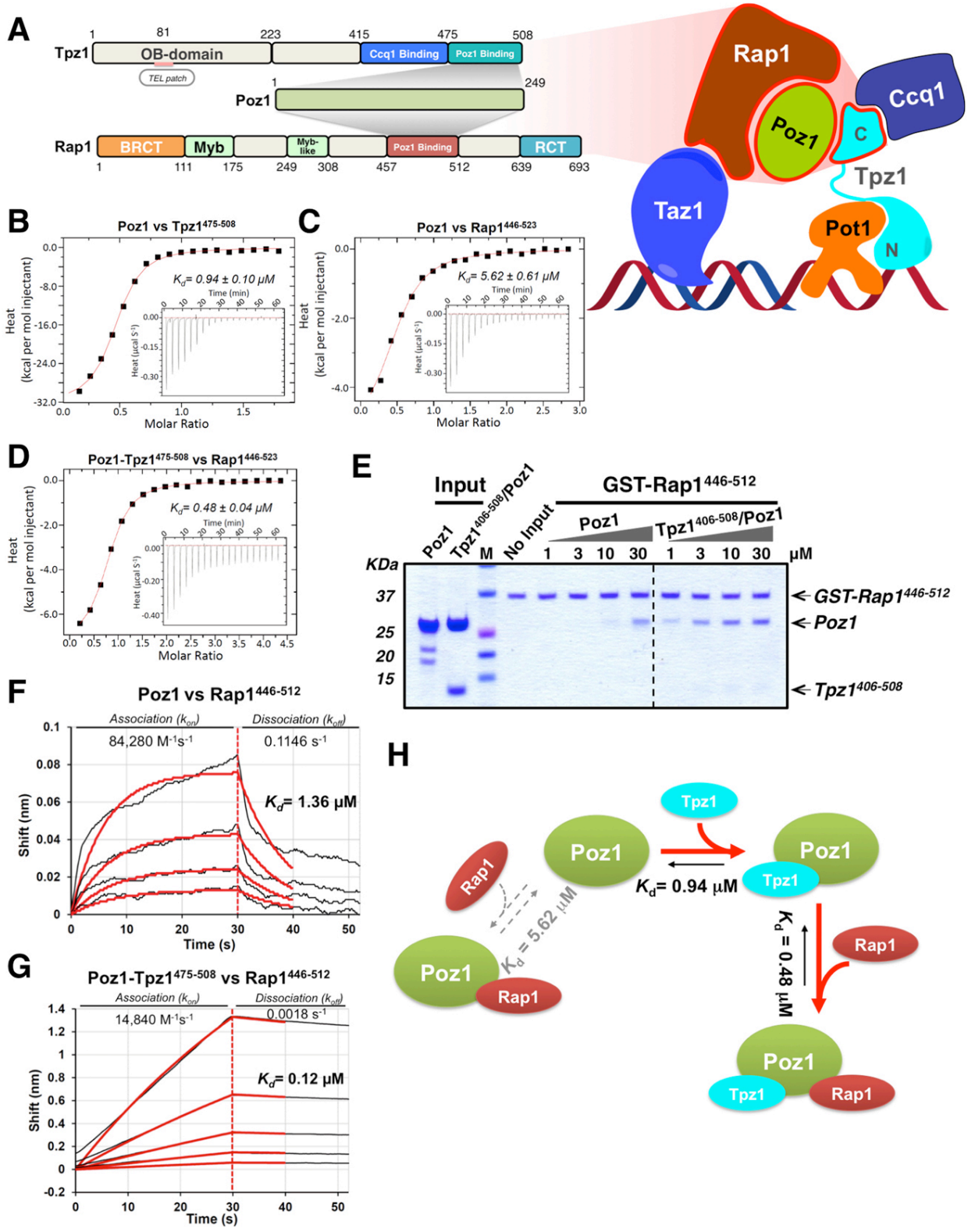

Figure 1. Tpz1-Poz1 interaction promotes Poz1-Rap1 interaction. See next page for legend.

Figure 1. Tpz1-Poz1 interaction promotes Poz1-Rap1 interaction. (A) Schematic diagram of *S. pombe* Tpz1-Poz1-Rap1 interaction (*left*) in the setting of overall shelterin complex on the telomere (*right*). *Left*: Domain organization of shelterin bridge components Tpz1, Poz1, and Rap1. Poz1 interacts simultaneously with the C-terminal domain of Tpz1 and a middle domain of Rap1. *Right*: Overview of *S. pombe* shelterin complex. Double-stranded telomeric DNA binding protein Taz1 and single-stranded DNA binding protein Pot1 are connected by their protein interaction partners—Rap1, Poz1, and Tpz1, forming a shelterin bridge between Taz1 and Pot1. For clarity, the stoichiometry of each individual component is not indicated in the figure; only one copy of each component is shown. **(B)**, **(C)** and **(D)** ITC measurements of interactions between Poz1 and Tpz1$^{475\text{-}508}$ (B), Poz1 and Rap1$^{446\text{-}523}$ (C), and Tpz1$^{475\text{-}508}$-Poz1 complex and Rap1$^{446\text{-}523}$ (D). The Poz1- Tpz1$^{475\text{-}508}$ interaction has ~6-fold higher binding affinity than that of the Poz1-Rap1$^{446\text{-}523}$ interaction. The binding of Tpz1$^{475\text{-}508}$ to Poz1 increases the binding affinity of Poz1- Rap1$^{446\text{-}523}$ interaction interaction more than 10 fold. Inserts are titration data, with the dissociation constants (K_d) value ± standard deviation calculated from the fit shown above it. All ITC experiments were repeated twice and representative results were shown. **(E)** *In vitro* GST pull-down assays examining Poz1-Rap1$^{446\text{-}512}$ and Tpz1$^{406\text{-}508}$-Poz1 complex-Rap1$^{446\text{-}512}$ interactions. Tpz1$^{406\text{-}508}$ promotes strong Poz1-Rap1$^{446\text{-}512}$ interaction (right side of the dashed line). Input: 0.1 nmole Poz1 or Tpz1$^{406\text{-}508}$-Poz1 before their incubation with GST-Rap1$^{446\text{-}512}$. **(F)** and **(G)** Bio-Layer Interferometry (BLI) sensorgrams obtained using biosensors loaded with Biotin-SUMO-tagged Rap1$^{446\text{-}512}$ (Zhao et al., 2016), incubated with different concentrations of Poz1 (F) or Tpz1$^{475\text{-}508}$-Poz1 complex (G) used as analysts. Binding curves were fit globally to a 1:1 binding model to yield equilibrium dissociation constant (K_d), as well as association (k_{on}) and dissociation (k_{off}) rate constants for Poz1-Rap1$^{446\text{-}512}$ (R2 = 0.9778) (F) or Tpz1$^{475\text{-}508}$-Poz1 complex-Rap1$^{446\text{-}512}$ (R2 = 0.9996) (G) interactions. Tpz1$^{475\text{-}508}$-Poz1 forms very stable complex with Rap1$^{446\text{-}512}$ and dissociates from Rap1$^{446\text{-}512}$ ~60 times slower than the dissociation of free Poz1 from Rap1$^{446\text{-}512}$, based, based on the k_{off}. All BLI experiments were repeated twice and representative results were shown. **(H)** Assembly pathway for Tpz1-Poz1-Rap1 complex. Based on binding affinity difference, Poz1 has strong preference to bind Tpz1 first, and Tpz1-Poz1 complex then interacts with Rap1 to form the ternary complex.
See Figure S1.

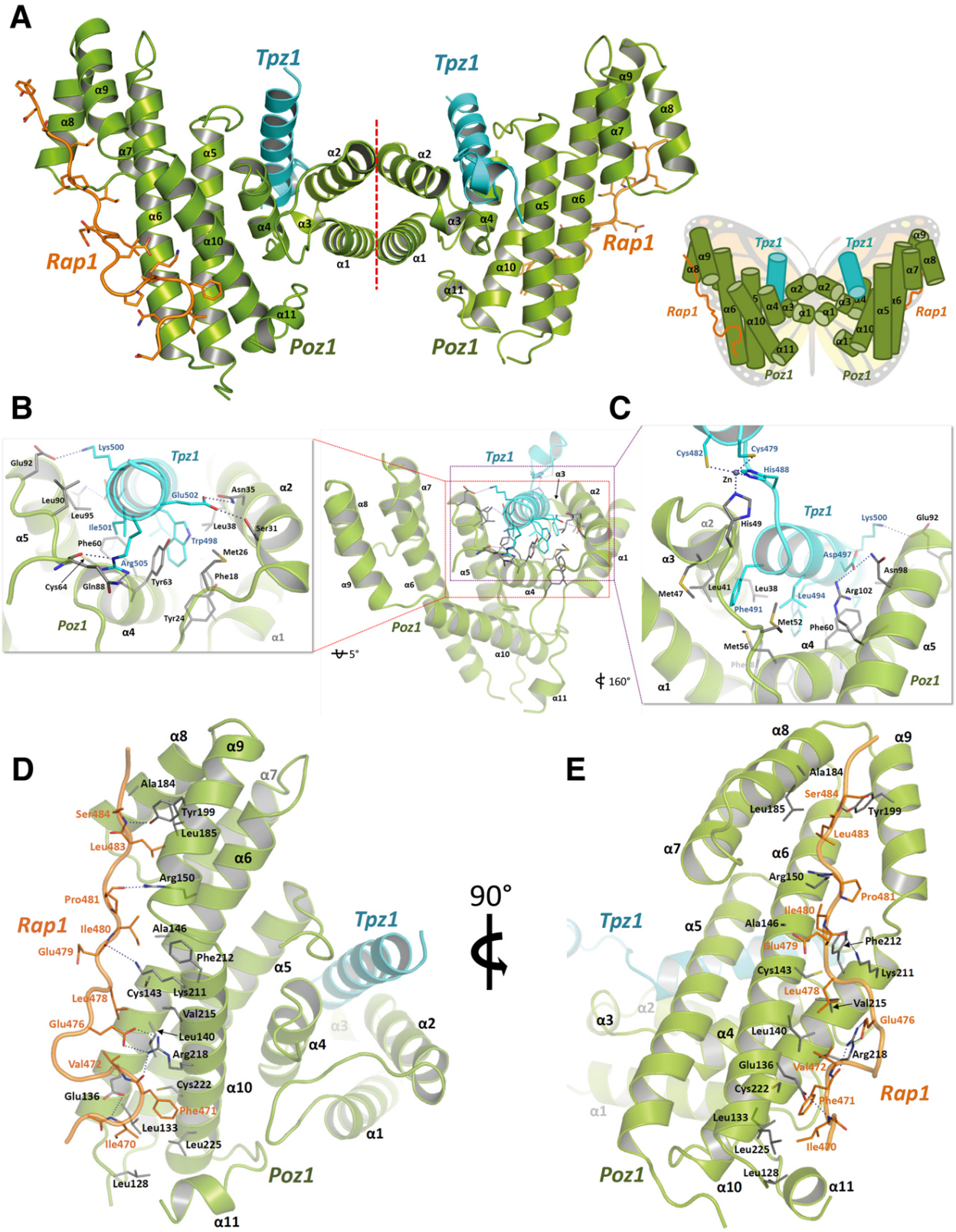

Figure 2. Crystal structure of the Tpz1-Poz1-Rap1 complex. See next page for legend.

Figure 2. Crystal structure of the Tpz1-Poz1-Rap1 complex. (A) Overall structure of the dimer form of Tpz1-Poz1-Rap1 complex, colored according to shelterin schematic drawing in Figure 1A with Tpz1 in cyan, Poz1 in light green, and Rap1 in brown (*left*) and schematic representation of Tpz1-Poz1-Rap1 complex structure (*right*). *Left:* First two helices (α1 and α2) in the N-terminus of Poz1 are involved in the dimerization of Tpz1-Poz1-Rap1 complex. Red dashed line indicates the dimer interface. Tpz1 was surrounded by 5 helices (α1, α2, α3, α4, and α5) of Poz1, located close to the dimerization interface. Rap1 binds to a long groove in Poz1 created by its helices α8, α9, and α10 turning around helix α6. *Right:* the outline of the dimer of Tpz1-Poz1-Rap1 complex resembling a butterfly shape. The position of each Tpz1 is at each antenna of the butterfly and the dimerization region of Poz1 forms the body part of the butterfly. Rap1 binding site is at the edge of each wing. **(B)** and **(C)** Close-up views of Tpz1-Poz1 interface. (B) Hydrophobic core residue, Trp498 interacts with Tyr63 by π-π stacking and is surrounded by hydrophobic residues Phe18, Tyr24, Met26, Leu38 and Tyr63 of Poz1. Glu502 forms H-bonds with Ser31 and Asn35 of Poz1. (C) Ile501 of Tpz1 is located in a hydrophobic core interacting with Phe60, Tyr63, Cys64, Leu90, and Leu95 of Poz1. **(D)** and **(E)** Close-up views of Rap1-Poz1 interface. (D) Leu128, Leu133, Leu140, Cys222, and Leu225 of Poz1 provide hydrophobic patch for the binding of Ile470, Phe471 and Val472 of Rap1. Arg218 in Poz1 is involved with H-bond with Glu476 of Rap1, which is located in middle of Rap1. Phe471 of Rap1 interacts with Cys222 of Poz1 by aromatic-thiol π-type H-bond (3.8 Å). (E) Ile480 of Rap1 is located on the center of a hydrophobic core, which interacts with Cys143 and Ala146 and Phe212 of Poz1. Leu478 of Rap1 interacts with Leu140, Cys143 and Val215 of Poz1. The side chain of Leu483 in Rap1 is surrounded by the hydrophobic residues, Ala184, Leu185, and Tyr199 in Poz1. All figures for the structure presentations were generated with PyMol. See Figure S2, Table 1.

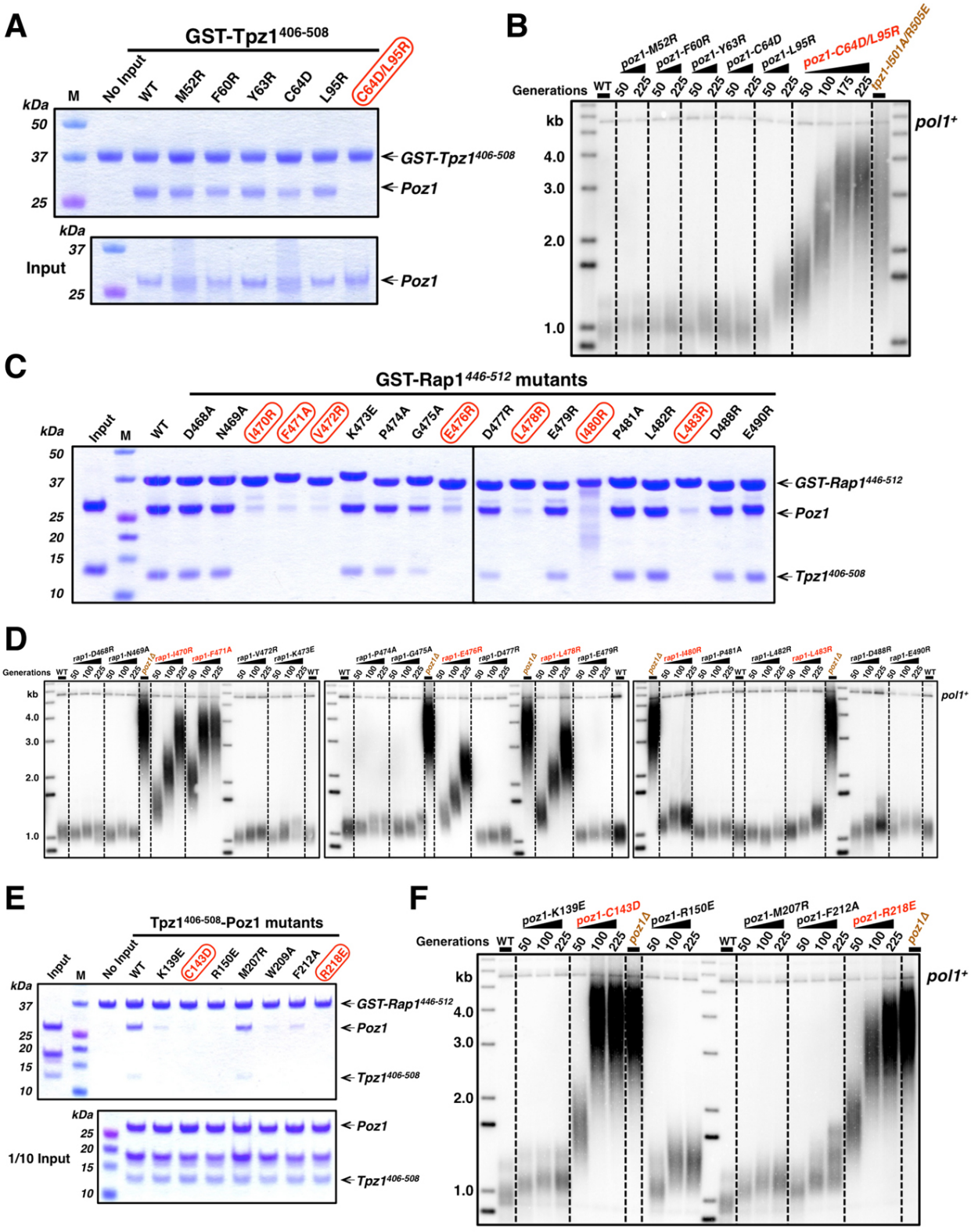

Figure 3. Dissection of Tpz1-Poz1-Rap1 interfaces and dramatic telomere elongation caused by binding deficient mutants. See next page for legend.

Figure 3. Dissection of Tpz1-Poz1-Rap1 interfaces and dramatic telomere elongation caused by binding deficient mutants. (A) *In vitro* GST-pulldown assays evaluating the binding of Poz1 mutants to GST-Tpz1$^{406\text{-}508}$. A double mutant of Poz1, Poz1-C64D/L95R (colored in red), is defective in binding to GST-Tpz1$^{406\text{-}508}$. Input: 1/15 of the samples before their incubation with GST-Tpz1$^{406\text{-}508}$. **(B)** Telomere length analysis of indicated *poz1* mutant strains from successive re-streaks on agar plates by southern blotting. The telomere fragment is released from total genomic DNA by EcoRI digestion. *tpz1-3Flag* serves as wild-type control and is denoted as "WT"; *tpz1-I501A/R505E* (colored in brown) is a previously identified mutant defective in Poz1-Tpz1 interaction and thus serves as a control. In this paper, the 1 kb plus marker (from Life Technologies) is used in all telomere length analysis. *pol1^{+}* indicates an EcoRI digested *pol1^{+}* gene fragment, which is used as the loading control. **(C)** and **(E)** *In vitro* GST-pulldown assays evaluating the bindings of GST-Rap1$^{446\text{-}512}$ mutants to Tpz1$^{406\text{-}508}$-Poz1 complex (C), and reversely, Tpz1$^{406\text{-}508}$-Poz1 mutants to GST-Rap1$^{446\text{-}512}$ (E). The mutants that disrupt Poz1-Rap1 interaction are colored in red. Input: 1/10 of Tpz1$^{406\text{-}508}$-Poz1 complex, either WT or mutants, before their incubation with GST-Rap1$^{446\text{-}512}$. **(D)** and **(F)** Telomere length analysis of indicated *rap1* mutant strains (D) or *poz1* mutants strains (F) from successive re-streaks on agar plates by southern blotting. The telomere fragment is released from genomic DNA by EcoRI digestion. *rap1-WT-3Flag* (D) or *poz1-WT-13myc* (F) is denoted as "WT" in the telomere blot.
See Figure S3.

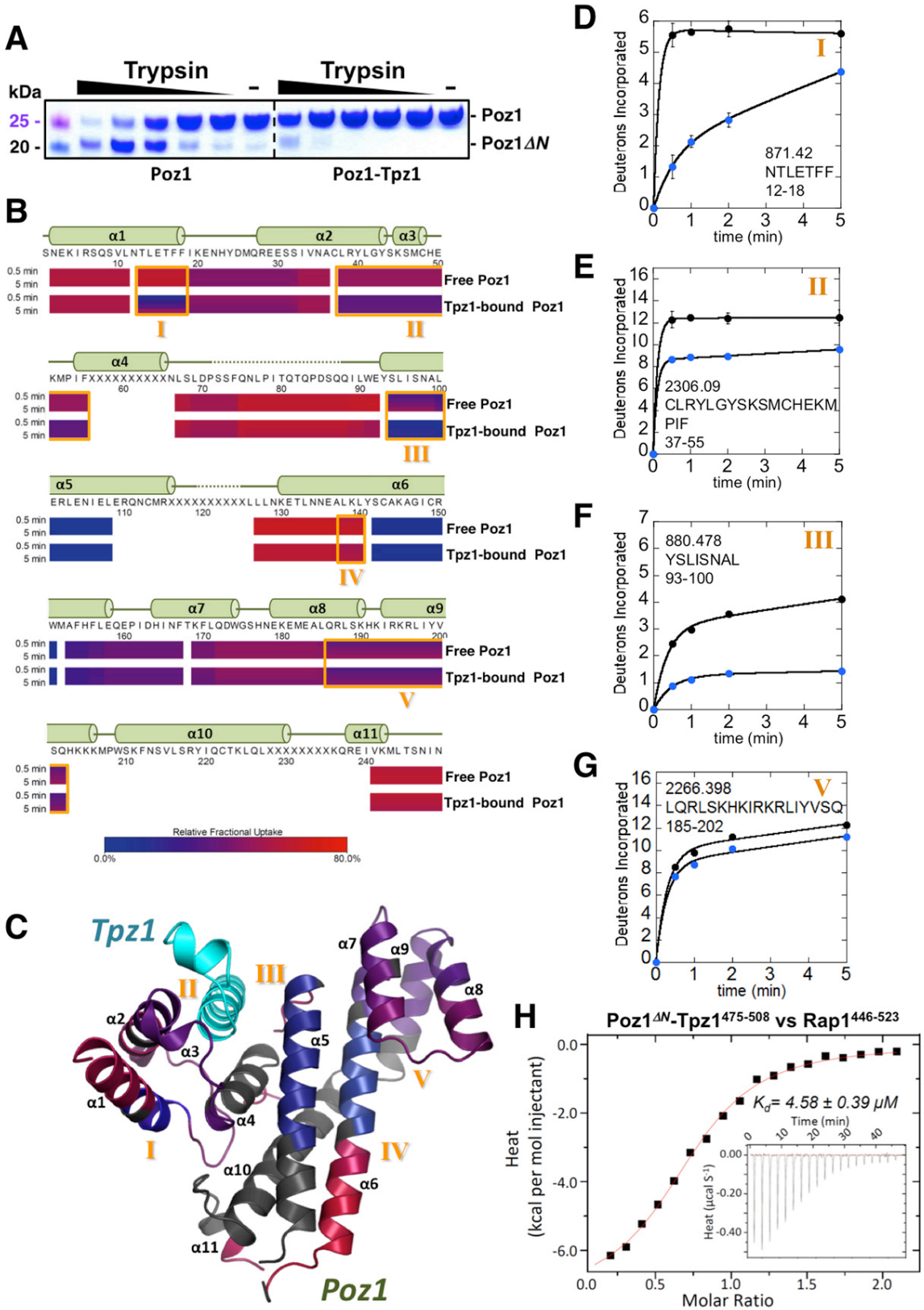

Figure 4. Identification of flexible region on N-terminus of Poz1. See next page for legend.

Figure 4. Identification of flexible region on N-terminus of Poz1. (A) Limited proteolysis assay of free Poz1 and Tpz1-Poz1 complex in the presence of increasing trypsin concentration. While Poz1 was rather stable in the Tpz1-bound form, Poz1 alone was cleaved by trypsin and produced a band with lower molecular weight. **(B)** Hydrogen-Deuterium Exchange Mass Spectrometry (HDXMS) analysis of free Poz1 and Tpz1-bound Poz1. Poz1 sequence is annotated by heat-maps below the sequence according to percent exchange after 0.5 and 5 min. Residues of Poz1 for which exchange are not reported are indicated as "X"s in the sequence and blank regions in heat-maps. The regions with lower deuterium exchange rate in Tpz1-bound Poz1 than that of free Poz1 are boxed with orange color (I, II, III, IV, and V). Secondary structure elements of Poz1 are indicated above the sequence. **(C)** Poz1 structure in the Tpz1-Poz1 complex is colored based on its exchange rate measured in the Tpz1-bound state as shown in (B). Regions with no exchange data reported are colored gray in the Poz1 structure. Tpz1 is color in cyan. **(D)**, **(E)**, **(F)** and **(G)** Amide hydrogen-deuterium exchange in Poz1 with and without Tpz1. The graphical data of deuterium incorporation in Poz1 show differences between free Poz1 (Black dot) and Tpz1-bound Poz1 (Blue dot) in I (D), II (E), III (F), and V (G) regions of (B). Error bars indicate standard deviation (n = 3). **(H)** ITC measurement of the affinity between Tpz1$^{475\text{-}508}$-Poz1*ΔN* complex and Rap1$^{446\text{-}523}$. The binding affinity of Tpz1$^{475\text{-}508}$-Poz1*ΔN* complex-Rap1$^{446\text{-}523}$ interaction (4.58 mM) is similar to that of free Poz1-Rap1$^{446\text{-}523}$ interaction (5.62 μM). Insert is the titration data, with the K_d value ± standard deviation calculated from the fit shown above it. ITC experiments were repeated twice and representative results were shown.
See Figure S4.

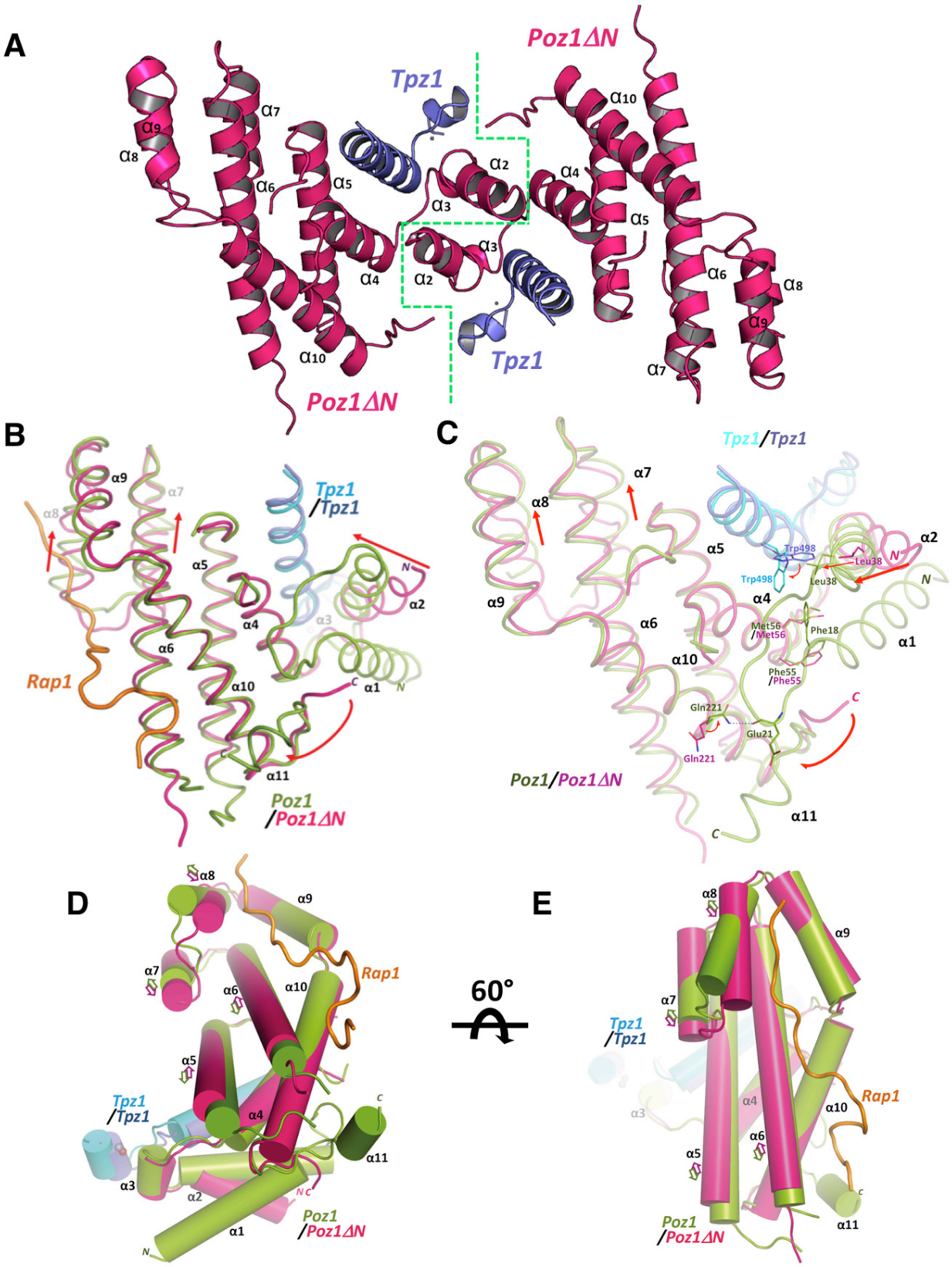

Figure 5. Structural comparison of Tpz1-Poz1Δ*N* and Tpz1-Poz1 complexes. See next page for legend.

Figure 5. Structural comparison of Tpz1-Poz1Δ*N* and Tpz1-Poz1 complexes. (A) Overall structure of the dimer of Tpz1 (slate)-Poz1**Δ*N*** (hotpink) complex. Two helices of Poz1 (α2 and α3) comprise the dimerization interface. The green dashed-line indicates the dimer interface. **(B)** Superposition of Tpz1-Poz1*ΔN* and Tpz1-Poz1 complexes using C_α atoms. Conformational changes are observed in α2, α7, α8 and α11 of Poz1, indicated by red arrows. The RMSD (root-mean-square deviation) between the two structures is 1.29 Å. **(C)** Close-up view of conformational changes induced by Poz1 "conformational trigger", helix α1, upon Tpz1 binding to Poz1. **(D)** and **(E)** Two close-up views of the structural changes in the Rap1 binding site of Poz1. Tpz1-binding induces allosteric structural changes in Poz1, resulting in a more open binding groove for Rap1. The arrows indicate the directions of helix movements due to the structural changes.
See Figure S5.

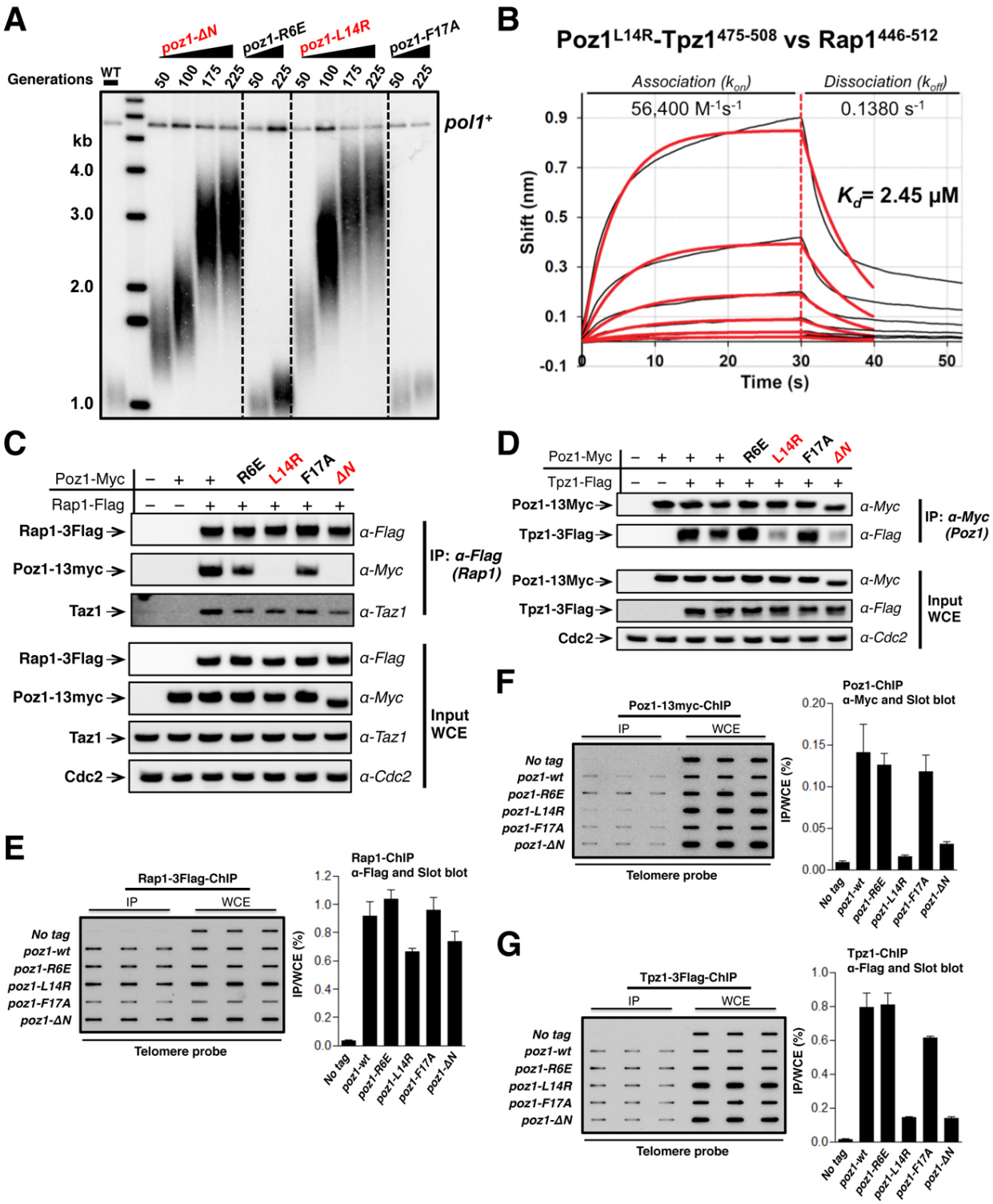

Figure 6. The "conformational trigger" in Poz1 is essential for shelterin assembly and telomere length regulation. See next page for legend.

Figure 6. The "conformational trigger" in Poz1 is essential for shelterin assembly and telomere length regulation. (A) Telomere length analysis of *poz1-NTD* mutant cells from successive re-streaks on agar plates. Total genomic DNA was digested by EcoRI. Wild-type cells are denoted as "WT" in the blot. Simultaneously digested *pol1*$^{+}$ DNA fragment serves as the loading control. Telomeres are elongated in *poz1-ΔN* and *poz1-L14R* cells (colored in red). **(B)** Bio-Layer Interferometry (BLI) sensorgrams monitoring dissociation and association events in real time between Poz1^{L14R}-Tpz1$^{475-508}$ and Rap1$^{446-512}$ using Octet red96 (R^2=0.9949). BLI experiments were repeated twice and representative results were shown. **(C)** and **(D)** Co-IP assays evaluating the effect of Poz1 N-terminal helix deletion or mutation on Taz1-Rap1, Poz1-Rap1 (C), and Tpz1-Poz1 (D) interactions. Poz1-Rap1 interaction is fully disrupted in *poz1-ΔN* and *poz1-L14R* cells, whereas Poz1-Tpz1 interaction is weakened in *poz1-ΔN* and *poz1-L14R* cells. Rap1-Taz1 interaction remains unchanged. **(E)**, **(F)** and **(G)** Telomeric localization of Rap1 (E), Poz1 (F), and Tpz1 (G) in strains with Poz1 N-terminal helix deletion or mutation was monitored by chromatin immunoprecipitation (ChIP) assay. Slot blot hybridized with telomere probe was used to visualize the telomeric signal associated with each protein. Error bars in the quantitation of the slot-blot analysis represent standard deviations of three individual repeats. Each ChIP assay was performed in triplicate (n=3). Error bars represent standard deviations. See Figure S6.

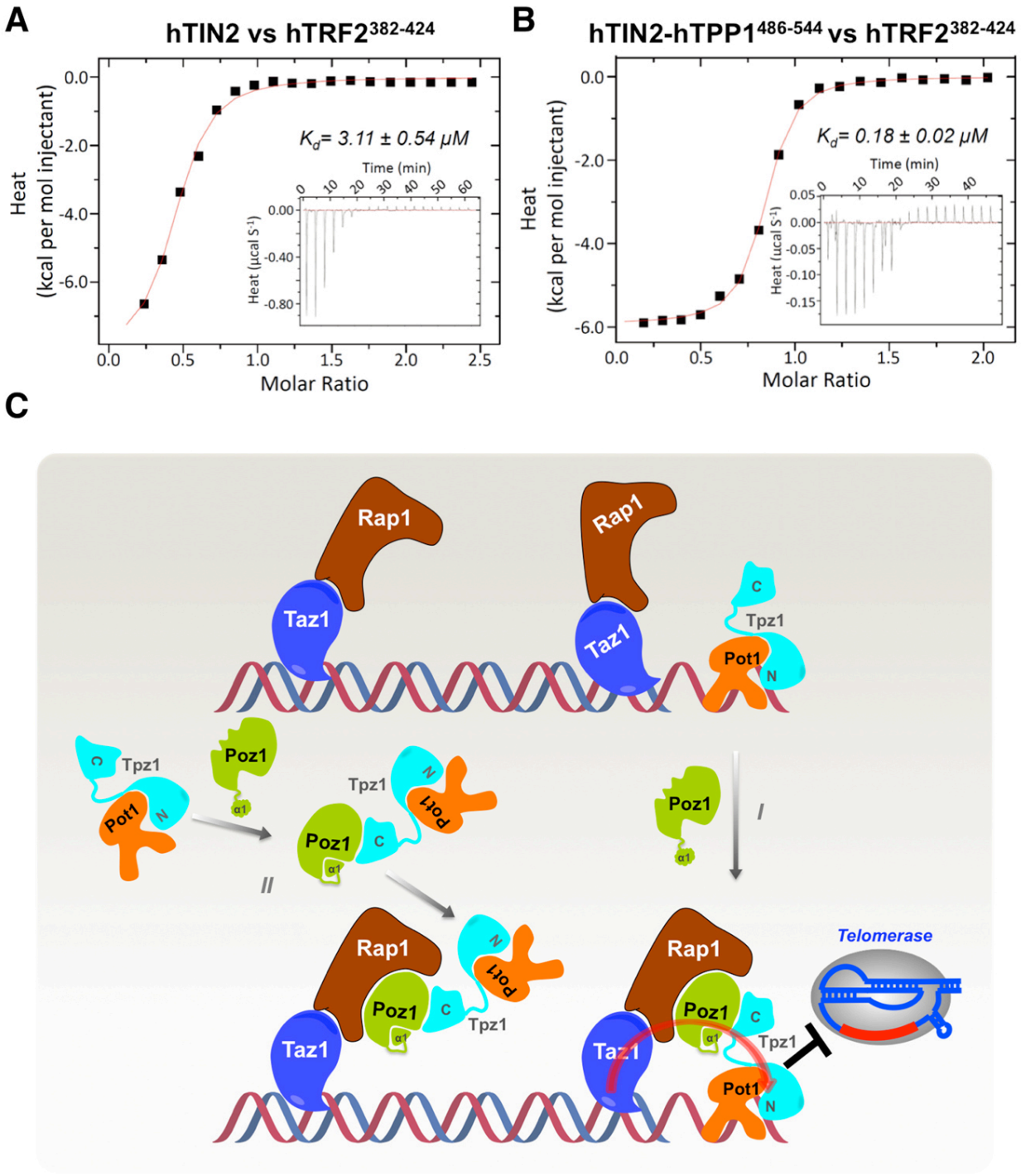

Figure 7. Conserved driving force for Cooperativity of human shelterin assembly. See next page for legend.

Figure 7. Conserved driving force for Cooperativity of human shelterin assembly. (A) and **(B)** ITC measurements of interactions between human shelterin components, hTIN2 and hTRF2$^{382-424}$ (A), and hTIN2-hTPP1$^{486-544}$ complex and hTRF2$^{382-424}$ (B). The binding of hTPP1$^{486-544}$ to hTIN2 increases the binding affinity of hTIN2-hTRF2$^{382-424}$ more than ~17 fold. Insert is the titration data, with the K_d value ± standard deviation calculated from the fit shown above it. ITC experiments were repeated twice and representative results were shown. **(C)** The schematic model of hierarchical shelterin complex assembly at telomeres in fission yeast. See Figure S7.

Table 1. Data collection and refinement statistics table.

Data collection	Tpz1$^{475-508}$-Poz1-Rap1$^{467-496}$	Tpz1$^{475-508}$-Poz1$^{29-249}$	Tpz1$^{475-508}$-Poz1-Rap1$^{470-494}$	Tpz1$^{475-508}$-Poz1^{3m}-Rap1$^{470-494}$
X-ray source	ALS 821	ALS 501	ALS 501	ALS 821
Wavelength (Å)	0.999996	0.977408	0.999931	0.979644
Space group	P_1	$P3_1$	$P2_12_12_1$	$P3_121$
Unit cell (a, b, c)	56.7, 82.0, 103.5	66.1, 66.1, 123.2	83.4, 95.4, 109.2	108.6, 108.6, 132.6
(α, β, γ)	90.0, 90.0, 74.0	90.0, 90.0, 120.0	90.0, 90.0, 90.0	90.0, 90.0, 120.0
Resolution (Å)	62.71-2.30 (2.42-2.30)	57.25-3.20 (3.37-3.20)	83.33-2.50 (2.64-2.50)	94.04-3.50 (3.69-3.5)
Reflections	178,361 (26,527)	52,268 (7,698)	221,705 (33,056)	150,707 (21,965)
Unique Reflections	77,768 (11,346)	9,911 (1,438)	30,787 (4,415)	11,817 (1,672)
Completeness (%)	97.6 (97.2)	99.7 (99.5)	99.9 (100.0)	100.0 (100.0)
Redundancy	2.3 (2.3)	5.3 (5.4)	7.2 (7.5)	12.8 (13.1)
R_{merge}[a]	0.103 (0.434)	10.4 (76.5)	8.7 (66.0)	0.128 (0.794)
Rmeas	0.132 (0.555)	0.116 (0.847)	0.094 (0.708)	0.146 (0.851)
Rpim	0.080 (0.342)	0.050 (0.361)	0.035 (0.255)	0.040 (0.232)
CC1/2	0.983 (0.726)	0.998 (0.847)	0.998 (0.912)	0.999 (0.887)
I/sigma	5.8 (2.4)	11.5 (2.6)	13.1 (2.8)	15.1 (4.2)
Wilson B factor (Å^2)	32.5	78.2	46.2	85.5
Refinement			0.357(initial)/0.77(final)	
Reflection used in Refinement	77,751 (5,512)	9,872 (2,310)	30,695 (2,001)	
Reflection used for R-free	1,978 (126)	514 (108)	2,000 (139)	
Resolution (Å)	62.73-2.30 (2.36-2.30)	51.92-3.20 (3.52-3.20)	45.67-2.50 (2.56-2.50)	
R_{work}[b]	0.1996 (0.2905)	0.2664 (0.3305)	0.2093 (0.2693)	
R_{free}[c]	0.2247 (0.3868)	0.3165 (0.4376)	0.2626 (0.3223)	
Number of atoms	9,273	3,513	4450	
Number of Ions	4 (Zn)	2 (Zn)	2 (Zn)	
Protein residues	1,076	417	525	
Waters	317	-	34	
B-values (Å^2)	46.4	86.7	66.1	
RMSD bonds (Å)	0.010	0.008	0.011	
RMSD angle (°)	1.12	1.5	1.28	
Ramachandran favored (%)	98.0	94.5	95.9	
Ramachandran allowed (%)	1.8	5.5	3.7	
Ramachandran disallowed (%)	0.2	0.0	0.4	
Rotamer outliers (%)	1.0	7.5	3.6	
Clashscore	7.24	23.41	10.48	
PDB ID	5WE0	5WE1	5WE2	

The numbers in parentheses are the statistics from the highest resolution shell.

[a] $R_{merge}=\sum|I-<I>|/\sum I$

[b] $Rwork=\sum|Fobs-Fcalc|/\sum Fobs$

[c] $R_{free}=\sum|Fobs-Fcalc|/\sum Fobs$, where all reflections belong to a test set of 5% randomly selected data.

CHAPTER 6

Recognition of budding yeast telomerase RNA by TERT and its role in template boundary definition

Abstract

Telomerase, a ribonucleoprotein (RNP) enzyme, serves the essential role in maintaining chromosome integrity by replenishing eroded telomere. The RNA subunit of telomerase, which is named TLC1 in *Saccharomyces cerevisiae*, not only provides the template during reverse transcription, but also has the scaffold role for the assemblies of Est1p, TERT (called Est2p in *Saccharomyces cerevisiae*), Ku, and Sm proteins with TLC forming the telomerase RNP. Although RNA elements of TLC1 that are responsible for mediating interactions with Est1p and with Ku have been identified and characterized, features of the core region of TLC1 that enable specific recognition of TLC1 by Est2p is much less known. To address this question, we probed Est2p-binding sites in TLC1 with single-nucleotide resolution using phosphorothioate footprinting. We find that the Est2p-binding sites lie in both sides of the template region. To our surprise, the secondary structure of the RNA elements, but not the sequence *per se*, is important for Est2p binding. Mutations introduced to disrupt the stem–loop secondary structure lead to shortened telomeres, whereas compensatory mutations that restore the secondary structure rescue telomeres to the wild-type length. Interestingly, we find that the distance between the two Est2p-binding sites in TLC1 is important for defining template boundary for reverse transcription; shortening of such distance by nucleotide deletion causes read-through of

the template. Our study reveals an active role of specific RNA-protein interactions in ribonucleoprotein enzyme function.

RESULTS

Assembling the TLC1 core region with Est2p-RBD *in vitro*

TLC1 is a ~1.2 kilo-nucleotide RNA with two thirds of dispensable regions for telomerase activity. To determine the interface of TLC1-Est2p, we set up *in vitro* assembly system with a derivative of Mini-T (500), which is called Micro-T 170 or μT-170. The three long flexible arms, as well as all functional distant ends, were removed and only the core region was remained in μT-170. When the μT-170 was analyzed with the RNA secondary structure prediction software Mfold, it was predicted to fold as same as TLC1 core. Therefore, we modeled the secondary structure of μT-170 according to the TLC1 core region with pseudoknot, based on the recently refined secondary structure with SHAPE assay and the crystal structure of partial Tetrahymena telomerase RNA (Fig. 1A).

Recombinant Est2p RNA Binding Domain (Est2p-RBD) was tagged with GST and optimized for overexpression in *E. coli* (Fig. 1B). Using a filter-binding assay, we measured the specific interaction between GST-Est2p-RBD and μT-170 with a K_d of 2.94 nM (Fig. 1C). Thus, we concluded that μT-170 retained the structure and function of TLC1 core region; and *in vitro* assembly system was established with GST-Est2p-RBD.

In vitro footprinting assay reveals three Est2 interfaces on μT-170

To identify the Est2p binding sites on μT-170, iodine cleavage protection assay was performed with the μT-170 containing phosphorothioate modification. The μT-170 was transcribed in the presence of NTP and α-Thiol NTP for partial incorporation of the nucleotides analogs by *in vitro* T7 transcription system. The RNA containing α-Thiol NTP is susceptible to iodine oxidative cleavage; however, interacting with a protein will block the access of iodine to the interface. Therefore, the binding sites on μT-170 will be expected to have reduced cleavage in the presence of GST-Est2-RBD.

The α-Thiol ATP incorporated μT-170 (or AαS-μT-170) and GST-Est2p-RBD were assembled *in vitro* and subjected to iodine treatment. Free AαS- μT-170 was used to generate ladder for sequencing gel, and mixing AαS- μT-170 with GST to eliminate non-specific iodine cleavage protection. The 5' end labeled μT-170 fragments were resolved on the sequencing gel. Comparing the AαS-μT-170 mixed with GST and GST-Est2p-RBD in the presence of 80 μM iodine, the protection was observed at many sites, which was visualized as reduced band signal in the presence of GST-Est2p-RBD. A22 to A41, A60 to A101, A121 to A123, A155 and A159 were identified as Est2 binding sites and were labeled as red on the right of gel (Fig. 2A). The same strategy was also applied to GαS-μT-170 (Fig. 2B). We successfully identified G19 to G24 as Est2p-RBD binding sites.

Since there are many nucleotides being protected by Est2p-RBD, we suspected that μT-170 utilizes more than one region to interact with Est2p-RBD. To this end, we mapped all the protected adenosine and guanine, which were highlighted in yellow or purple, on the

secondary structure of μT-170 (Fig. 2C). Not surprisingly, both sides of template region, which are called TBE (template boundary element) and TRE (template recognition element), respectively, are Est2p binding sites. The third interface is located near the triple helix in the pseudoknot region, which seems to share less similarity with other two interfaces. In the recent EM structure of Tetrahymena telomerase holoenzyme, telomerase RNA forms a ring shaped structure and TERT-RBD is inserted into it. In the manner, the Tetrahymena TERT-RBD is able to interact with different regions of telomerase RNA. Indeed, the interfaces we found in μT-170 via iodine cleavage protection assay correspond well to the ones in Tetrahymena telomerease.

Telomerase function in vivo requires the interactions between Est2 and all three interfaces on TLC1

To assess the significance of Est2-TLC1 interaction in telomerase activity, a series of Mini-T (500) or TLC1 mutants were designed to mutate the Est2p binding sites to disrupt or restore base pairing of these stems (Fig. 3A). As shown in right of Fig. 3A, the mutant at #16 region or M16 replaced the sequence of #16 region to its Watson-Crick complementary sequence, therefore disrupted the stem structure formed by #16 and #17 region. M17 was the same. However, in the compensatory mutant M16/17, #16 and #17 were mutated to the complementary sequence simultaneously, so that the stem structure could be restored even though the primary sequence was changed. The same design was also applied to #5a/12a, the binding sites near triple helix region, and #2a/8b, the binding sites on another side of template region (Supplementary Fig. 1).

Afterwards, a *tlc1Δ* strain was transformed with the above-mentioned Mini-T (500) mutants on a centromere plasmid, which has low copy-number in cells. Previous study has shown the Mini-T (500) cells have reduced fitness compared with TLC1; therefore, we suspected the sensitized Mini-T (500) cells could amplify any growth defects, including those caused by impaired telomerase activity. Successive cell culture was performed on solid media and the growth phenotype was assessed by checking colonies formation after selecting out the WT TLC1 cover plasmid. Interestingly, mutants M16, M17, M5a and M12a, which disrupted the stem structure, caused severe growth defect or even cell senescence, same as another two template mutants M18 and M19. However, the compensatory mutants M16/17 and M5a/12a could rescue the cell growth or even restore to wild type growth (Fig. 3B). This result indicates the secondary structure in these two Est2p binding sites, rather than the primary sequence, are essential for cell proliferation.

We further asked if the grow defects caused by Mini-T (500) mutants actually resulted from impaired telomerase activity. Since the telomere length of Mini-T (500) cells has already been shortened to the critical length, it is unfeasible to compare telomere length between Mini-T (500) WT and mutants. To this end, the centromere plasmids that harbor the above-mentioned TLC1 alleles were transformed in yeast. The cells of different generations from solid plate were future proliferated in liquid media and the genomic DNA was isolated to analyze telomere length. As shown in figure 3C, starting from 50 generations of growth on plate, the telomere lengths of the stem disruption mutants were substantially decreased in M16, M17, M5a and M12a. M2a and M8b caused less telomere shortening, which agreed with the growth phenotype of Mini-T (500) cells. Meanwhile, all three compensatory mutants were able to rescue the telomere shortening (Fig. 3C and

Supplementary Fig. 1). Taken together, we have identified three Est2p interfaces on TLC1, which are involved in telomerase activity. More importantly, Est2p specifically recognize the secondary structure, rather than primary sequence, of these interfaces.

Overexpression of the Est2-interface mutants don't affect telomere length

One potential caveat form above results was that the impaired telomerase activity, which was observed in the single mutants, might be caused by other reasons instead of defective TLC1-Est2p interaction. To explore more in depth, we constructed an extra set of strains in which the TLC1 mutants on a high copy number 2μ plasmid were introduce into wild type cells. In this case, the TLC1 mutants would be overexpressed in the presence of endogenous telomerase RNA. If the TLC1 mutants disrupted other telomerase function rather than Est2p interaction, such as M18 and M19, the outnumbered TLC1 mutants would be dominantly incorporated into telomerase holoenzyme and result in impaired telomerase activity, which was referred to 'dominant negative effect'. Oppositely, TLC1-Est2p interaction defective mutants would cause no or less dominant negative effect.

As shown in Fig. 4, overexpression of TLC1-M18 (Fig. 4A) or M19 (Fig. 4B) caused severe telomere shortening as expected. Meanwhile, overexpression of TLC1-WT or 2μ plasmid itself had no effect on telomere length, which suggested the dominant negative effects in M18 and M19 were the consequence of impaired telomerase activity. Strains that contain other TLC1 mutants, including the single mutants and compensatory mutants, all exhibited less dominant negative effect on telomere length (Fig. 4 and Supplementary Fig. 2). This result further provides evidence to substantiate that Est2p binds to these three

sites on TLC1. Interestingly, all the single mutants have shorter telomere length than the corresponded compensatory mutants. This also can be explained by the multiple interfaces between Est2p and TLC1. The outnumbered TLC1 single mutants could still bind to Est2p with less interfaces and low binding affinity; however, the lost interface would lead to misalignment of telomerase components and impaired telomerase activity.

Template anchoring through Est2-TLC1 interactions helps to define template boundary

We further set up to understand the biological significance of these multiple Est2p-TLC1 interfaces. Hypothetically, the close proximity between Est2p binding sites and template region indicates the role of Est2p-TLC1 interaction in defining template. One of the obvious evidence is that Est2p directly binds to the well-defined TBE (#16 and #17 in Fig. 3A). It may directly block the catalytic site on Est2p from moving beyond the template. Indeed, the crystal structure of *Tetrahymena* TERT RNA-binding domain with the TBE of TER has revealed atomic details in template boundary definition. However, it can't explain why Est2p still needs to bind to TRE, and what the relationship is between TBE and TRE. We noticed that the flexible and non-conserved sequences including template region, between pseudoknot and template boundary, exist in many TERs, such as human, mouse and ciliate. Therefore, we suspected that it is the distance between Est2p binding sites, rather than the sequence or the structure, that defines template region.

To this end, we deleted the nucleotides between pseudoknot and template in the μT-170, which generated μT-158. The new construct has the same Est2p binding sites (Fig. 5A);

however, we expected the template region in μT-158 would shift toward the template boundary region to compensate the nucleotides lost on the other side. *In vitro* primer extension assay clearly showed detectable read-through of 2 nt in μT-158 (Fig. 5A). The read-through disappeared in the absence of dATP, which suggested the signals beyond +7 were resulted from read-through, rather than the second round of telomerase reaction.

We then transformed the centromere plasmids with corresponded Mini-T (500) alleles into the cells, which are called Mini-T Δ141-168, Δ326-331 and Mini-T Δ139-168, Δ326-331, respectively. As expected, the cells with truncated Mini-T (500) show growth defects on solid media (Fig. 5B). Moreover, these cells have shorter telomeres than Mini-T (500) (Fig. 5C). Both results indicate deficiency in telomerase activity caused by the truncation between TRE and template of TER *in vivo*.

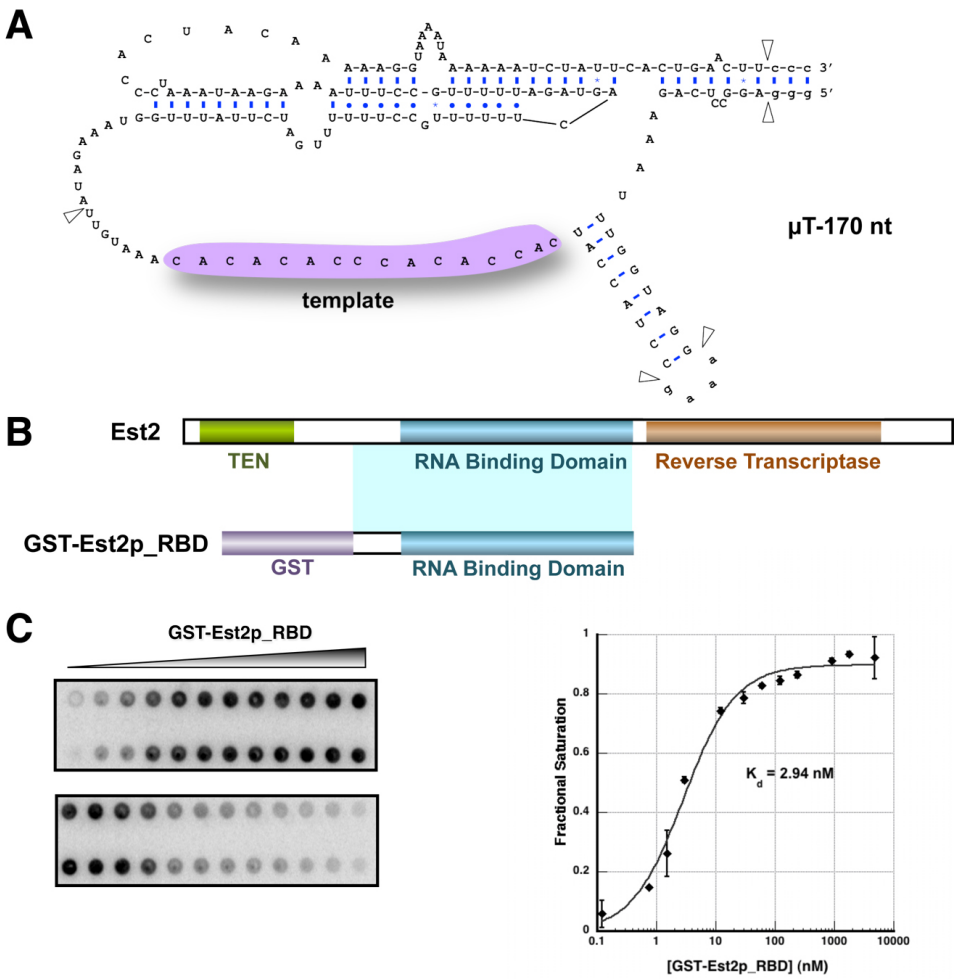

Figure 1. GST-Est2p_RBD binds μT170 RNA with high affinity. **(A)** and **(B)** Schematic diagram of *S. cerevesiae* μT170 (A) and GST-Est2_RBD (B). **(C)** Filter binding assay to measure binding affinity between μT170 and GST-Est2_RBP (left). The fitting curve is show on the right with calculated K_d inserted.

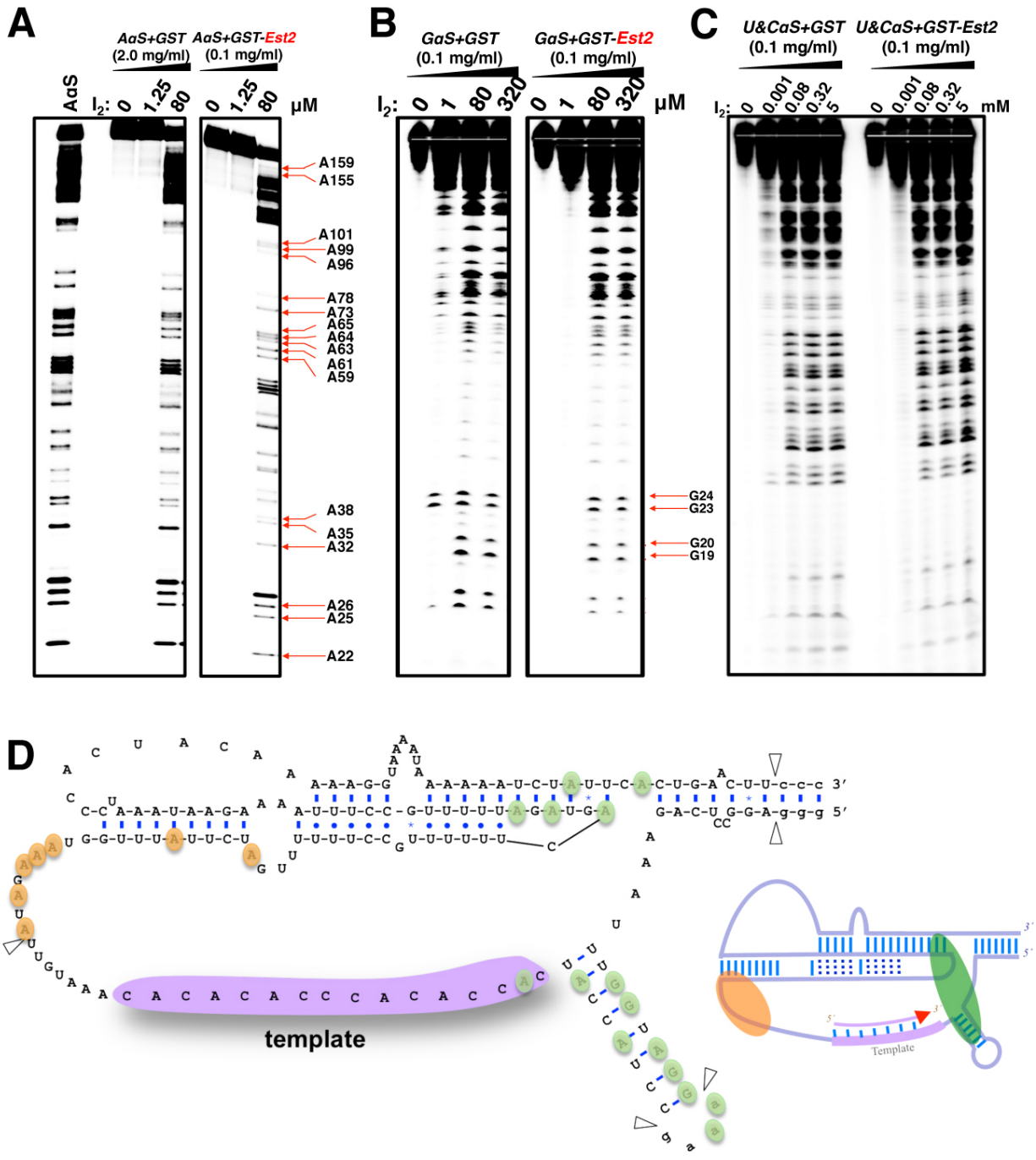

Figure 2. Iodine cleavage protection assay reveals Est2p binding regions of TLC1. (A) (B) and **(C)** Footprinting of protected μT170 sites upon GST-Est2p_RBD binding. μT170 incorporated with 1-Thio-ATP (A), 1-Thio-GTP (B) and 1-Thio-UTP (C) was cleaved by iodine with or without Est2p_RBP incubation. **(D)** Schematic diagram of protected sites by Est2p_RBD; the interface clearly locates at both sides of template region.

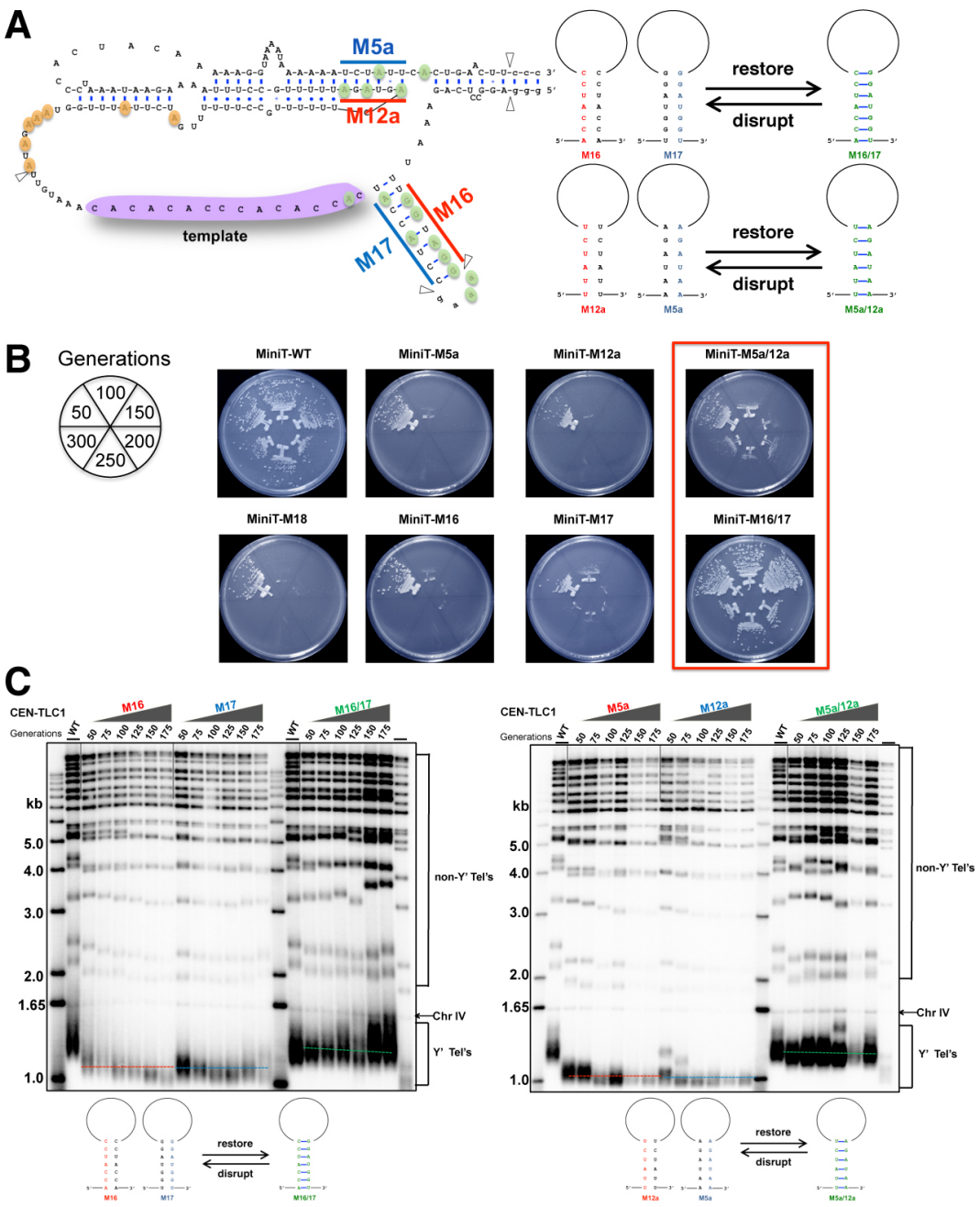

Figure 3. Functional dissection of TLC1-Est2_RBD interface. **(A)** Schematic diagram of RNA mutants designed to disrupt or restore the 2nd structure. **(B)** Severe cell proliferation defects are caused by single mutants; restoring the 2nd structure with complementary sequence is able to rescue cell growth. **(C)** Telomere length shortening is caused by single mutants and rescued by compensatory mutants.

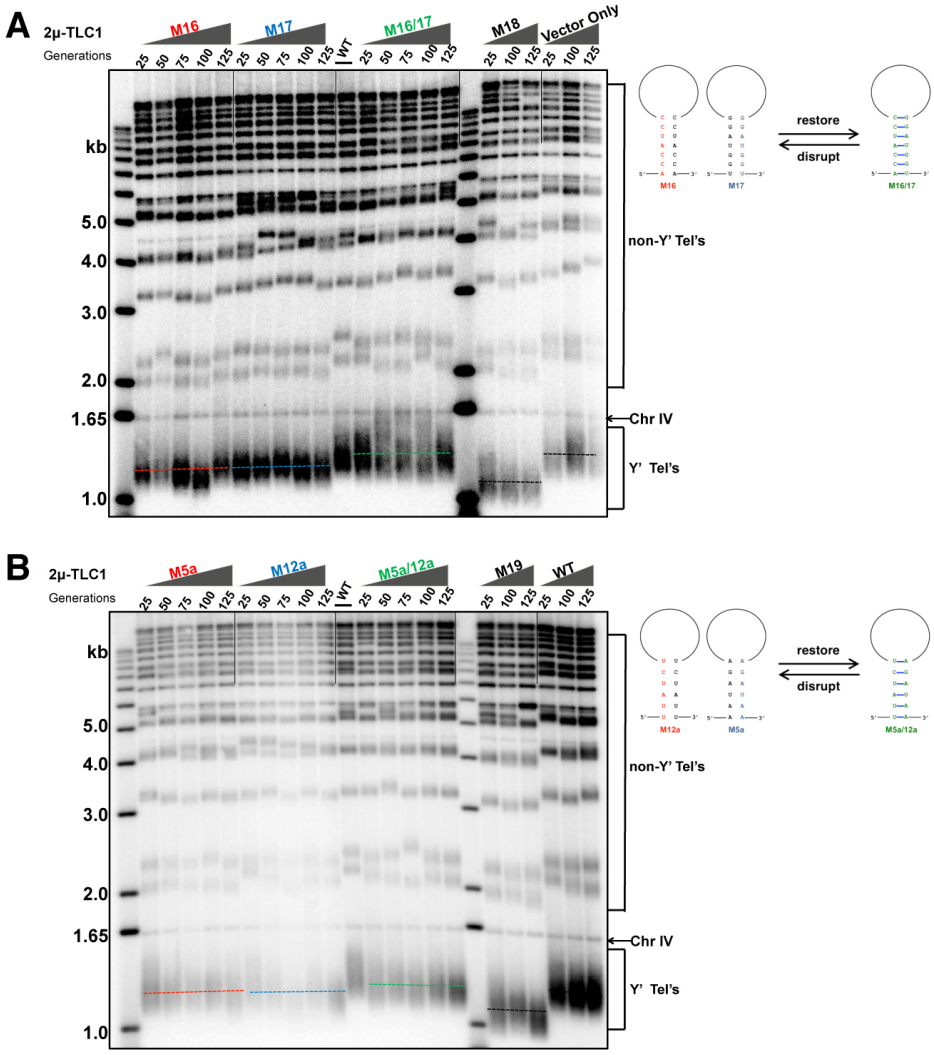

Figure 4. TLC1-Est2p interface mutants show less dominant negative effect. (A) and **(B)** Overexpression of TLC1-Est2p interface mutants has little effect on telomere length maintenance. M18 and M19 are catalytic sites mutants and show significant dominant negative effect.

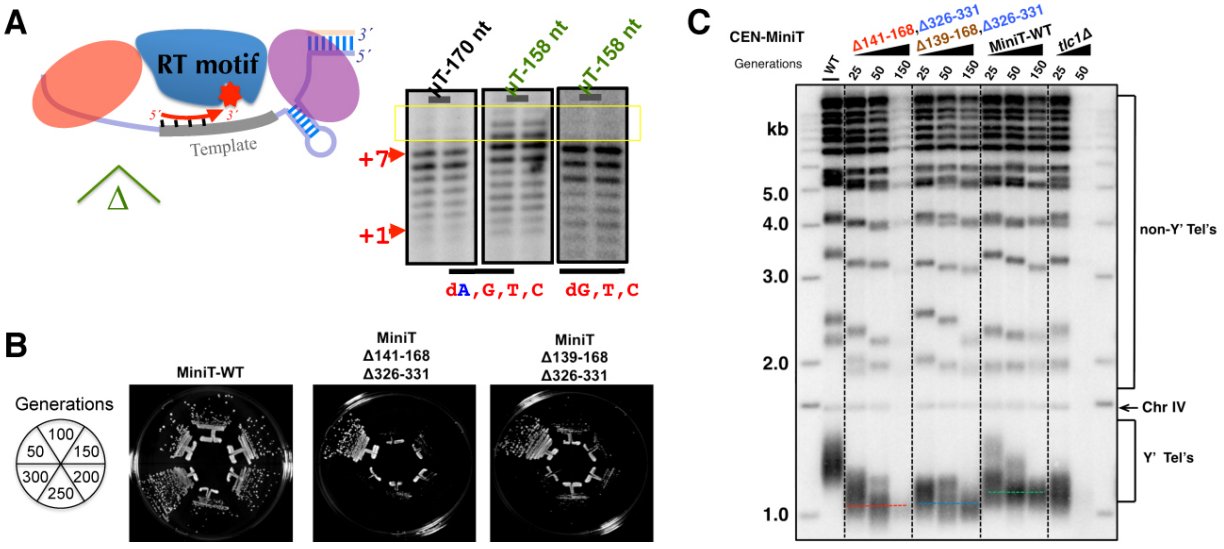

Figure 5. Template anchoring helps to define template boundary. **(A)** Truncation between TBE and TRE causes read-through over template region in telomerase activity assay *in vitro*. **(B)** and **(C)** Reduction in the distance between TBE and TRE causes cell growth defect (B) and telomere length maintenance defect (C).

CHAPTER 7

Summary and Conclusions

My Ph.D. thesis concentrates on elucidating the strategies that our cells adopt to maintain the very end of our chromosomes and their implications in cancer cell transformation. Telomeres have drawn tremendous attention since 1970s when it was first suggested as the "mortality clock" to measure the life span of a cell (Harley et al., 1990). Indeed, remarkable amount of genetic diseases caused by disruption of telomere maintenance have been continuously identified. Shortly after the discovery of human telomerase, it was shown that about 85% of cancer cells have abnormally increased telomerase activity, the enzyme acting to replenish lost telomeres along cell divisions. Moreover, exactly the opposite happens to the down-regulation of telomere lengthening: abnormally short telomeres are typically associated with premature aging syndromes, including certain forms of aplastic anemia and dyskeratosis congenital. Understanding the fundamental mechanisms that regulate telomere homeostasis is an obvious starting point to cure those diseases caused by aberrant telomere maintenance. During cell proliferation, our linear chromosomes cannot be fully copied and lose portions from their ends every cell cycle. And the existence of telomere and its replenishment by telomerase elegantly solve this fundamental problem. Therefore, shorter telomeres can reduce the replication capacity of cells and accelerate aging process of the entire organism. On the other hand, longer

telomeres will gain more replicative time to accumulate genomic mutations that lead to malignant transformation and development of multiple types of cancers.

The telomere length needs to be maintained at the defined range based on species; and this precise regulation of telomere length homeostasis is achieved through dynamic switch between two states of telomeres: telomerase-extendible and telomerase non-extendible states (Teixeira et al., 2004). Chapter 3 described a novel strategy called *MICro-MS* (Mapping Interfaces via Crosslinking-Mass Spectrometry) to complete dissect protein-protein interface without a 3D structure. With this novel technology, protein-protein proximity in Tpz1-centered complex in fission yeast shelterin was comprehensively probed and separation-of-function mutants of Ccq1, Poz1, or Pot1 were dissected that facilitate the investigation of their roles in telomere maintenance. These mutants emphasize the importance of shelterin connectivity in negatively regulating telomerase. In addition, this study also has clinical significance. The fission yeast shelterin interaction interface is successfully applied to human shelterin and revealed that a melanoma-associated hPOT1 mutation lies in the hTPP1-hPOT1 interface and weakens their interaction. Therefore, upregulation of positive regulators of telomere elongation (such as telomerase) is equivalent to downregulation of the negative regulators (such as the shelterin bridge) to cause the deregulated telomere over-elongation, which provides cancer cells a longer lifespan to achieve replicative immortality.

Tightly controlled recruitment of telomerase, a low-abundance enzyme, to telomeres is essential for regulated telomere synthesis. One puzzling question in telomere field is the discrepancy in telomerase recruitment between human and fission yeast system, which share a similar shelterin architecture. In humans, a cluster of residues on human TPP1,

collectively termed TEL-patch, were identified to mediate direct TPP1-telomrease interaction for telomerase recruitment (Nandakumar et al., 2012; Sexton et al., 2012; Zhong et al., 2012). However, in *S. pombe*, telomerase is recruited by the cell cycle dependent phosphorylation of the addition shelterin component called Ccq1, the functional homolog of which has not been identified in human yet (Flory et al., 2004; Miyoshi et al., 2008; Tomita and Coo-per, 2008). In Chapter 4, the conserved TEL-patch residues were identified in *S. pombe* Tpz1. Moreover, deep analysis revealed that telomerase recruitment is promoted by a bivalent transition-state, in which the cell cycle-dependent Ccq1-Est1 interaction is coupled to the TEL patch-Trt1 interaction, hence ensuring timely and legitimate telomerase engagement. This *S. pombe* work is originally derived from human studies and turned out to provide a novel bivalent telomerase recruitment mechanism that is very likely to be conserved in humans.

The long-term goal is to obtain the structure of the shelterin complex with telomeric DNA to reveal the positional and architectural information of each component, and the conformational changes associated with telomeric state transitions. Chapter 5 shows the high-resolution crystal structure of Tpz1-Poz1-Rap1 complex and an intriguing fact about Tpz1-Poz1-Rap1 complex is its cooperative assembly. From ITC (Isothermal titration calorimetry) assay, Tpz1 is able to increase the binding affinity ten times of Poz1-Rap1 interaction. Remarkably, even though the primary sequence and protein interaction partner have been evolved in human shelterin (hTRF2-hTIN2-hTPP1), the cooperative assembly is firmly retained. This conservation indicates that the cooperative assembly of shelterin plays a vital role in telomere length homeostasis and it is worth pursuing further more. Moreover, the human TRF2-TIN2-TPP1 structure will provide valuable hints to

elucidate the initiation and development of dyskeratosis congenital since multiple hTIN2 variants have been identified in the patients (Frescas and de Lange, 2014; Frank et al, 2015).

More and more data indicate hierarchical complexity in telomere maintenance machinery, including telomerase (Jiang et al., 2015; Berman et al., 2011; Chapter 6 in this work), shelterin (O'Connor et al., 2006; Lim et al., 2017; Kim et al., 2017) and interaction between them (Sexton et al., 2014; Armstrong et al., 2014; Hu et al., 2016). Structural analysis of the whole machinery and deciphering the conformational changes among different functional states have emerged as a key step to fully understand telomere length homeostasis.

Reference

Abreu, E., Aritonovska, E., Reichenbach, P., Cristofari, G., Culp, B., Terns, RM., Lingner, J., Terns, MP. (2010). TIN2-tethered TPP1 recruits human telomerase to telomeres in vivo. Molecular and Cellular Biology *30*:2971–2982.

Aoude, L.G., Pritchard, A.L., Robles-Espinoza, C.D., Wadt, K., Harland, M., Choi, J., Gartside, M., Quesada, V., Johansson, P., Palmer, J.M., et al. (2015). Nonsense mutations in the shelterin complex genes ACD and TERF2IP in familial melanoma. Journal of the National Cancer Institute *107*:107.

Armanios, M., Blackburn, EH. (2012). The telomere syndromes. Nature Reviews Genetics *13*:693–704.

Armstrong, C.A., Pearson, S.R., Amelina, H., Moiseeva, V., Tomita, K. (2014). Telomerase activation after recruitment in fission yeast. Current Biology *24*:2006–2011.

Artandi, S.E., Cooper, J.P. (2009). Reverse transcribing the code for chromosome stability. Molecular Cell *36*:715–719.

Autexier, C., Lue, N.F. (2006). The structure and function of telomerase reverse transcriptase. Annual Review of Biochemistry *75*:493–517.

Baerlocher, G.M., Oppliger Leibundgut, E., Ottmann, O.G., Spitzer, G., Odenike, O., McDevitt, M.A., Roth, A., Daskalakis, M., Burington, B., Stuart, M.*, et al.* (2015). Telomerase Inhibitor Imetelstat in Patients with Essential Thrombocythemia. The New England journal of medicine *373*, 920-928.

Bähler, J., Wu, J.Q., Longtine, M.S., Shah, N.G., McKenzie, A. 3rd, Steever, A.B., Wach, A., Philippsen, P., Pringle, J.R. (1998). Heterologous modules for efficient and versatile PCR-based gene targeting in Schizosaccharomyces pombe. Yeast *14*:943–951.

Balasubramaniam, D., Komives, E.A. (2013). Hydrogen-exchange mass spectrometry for the study of intrinsic disorder in proteins. Biochim Biophys Acta *1834*, 1202-1209.

Batista, L.F., and Artandi, S.E. (2013). Understanding telomere diseases through analysis of patient-derived iPS cells. Current opinion in genetics & development *23*, 526-533.

Baumann, P., Cech, T.R. (2001). Pot1, the putative telomere end-binding protein in fission yeast and humans. Science *292*:1171–1175.

Berman, A.J., Akiyama, B.M., Stone, M.D., Cech, T.R. (2011). RNA accordion model for template positioning by telomerase RNA during telomeric DNA synthesis. Nature Structural & Molecular Biology *18*:1371-5.

Bernardes de Jesus, B., and Blasco, M.A. (2013). Telomerase at the intersection of cancer and aging. Trends in genetics : TIG *29*, 513-520.

Bessman, M.J., Lehman, I.R., Simms, E.S., Kornberg, A. (1958). Enzymatic synthesis of deoxyribonucleic acid. II. General properties of the reaction. The Journal of Biological Chemistry *233*:171-7.

Bianchi, A., Shore, D. (2007). Increased association of telomerase with short telomeres in yeast. Genes & Development *21*:1726–1730.

Bianchi, A., Shore, D. (2008). How telomerase reaches its end: mechanism of telomerase regulation by the telomeric complex. Molecular Cell *31*:153–165.

Blackburn, E.H., Gall, J.G. (1978). A tandemly repeated sequence at the termini of the extrachromosomal ribosomal RNA genes in Tetrahymena. The Journal of Biological Chemistry *120*:33-53.

Borah, S., Xi L., Zaug, A.J., Powell, N.M., Dancik, G.M., Cohen, S.B., Costello, J.C. Theodorescu, D., Cech, T.R. (2015). TERT promoter mutations and telomerase reactivation in urothelial cancer. Science *347*:1006–1010.

Chandra, A., Hughes, T.R., Nugent, C.I., Lundblad, V. (2001). Cdc13 both positively and negatively regulates telomere replication. Genes & Development *15*:404–414.

Chang, Y.T., Moser, B.A., Nakamura, T.M. (2013). Fission yeast shelterin regulates DNA polymerases and Rad3(ATR) kinase to limit telomere extension. PLoS Genetics *9*:e1003936.

Chikashige, Y., Hiraoka, Y. (2001). Telomere binding of the Rap1 protein is required for meiosis in fission yeast. Current Biology *11*:1618–1623.

Cohn, M., Blackburn, E.H. (1995). Telomerase in yeast. Science *269*, 396-400.

Collins, K. (2006). The biogenesis and regulation of telomerase holoenzymes. Nature Reviews Molecular Cell Biology *7*:484–494.

Cooper, J.P., Nimmo, E.R., Allshire, R.C., Cech, T.R. (1997). Regulation of telomere length and function by a Myb-domain protein in fission yeast. Nature *385*:744–747.

de Lange, T. (2005). Shelterin: the protein complex that shapes and safeguards human telomeres. Genes & development *19*, 2100-2110.

Erdel, F., Kratz, K., Willcox, S., Griffith, J.D., Greene, E.C., and de Lange, T. (2017). Telomere Recognition and Assembly Mechanism of Mammalian Shelterin. Cell reports *18*, 41-53.

Erzberger, J.P., Stengel, F., Pellarin, R., Zhang, S., Schaefer, T., Aylett, C.H., Cimermančič, P., Boehringer, D., Sali, A., Aebersold, R., Ban, N. (2014). Molecular architecture of the 40S•eIF1•eIF3 translation initiation complex. Cell *158*:1123–1135.

Evans, S.K., Lundblad, V. (1999). Est1 and Cdc13 as comediators of telomerase access. Science *286*:117–120.

Ferreira, M.G., Miller, K.M., Cooper, J.P. (2004). Indecent exposure: when telomeres become uncapped. Molecular cell *13*, 7-18.

Fitzpatrick, A.L., Kronmal, R.A., Kimura, M., Gardner, J.P., Psaty, B.M., Jenny, N.S., Tracy, R.P., Hardikar, S., Aviv, A. (2011). Leukocyte telomere length and mortality in the Cardiovascular Health Study. The journals of gerontology. Series A, Biological sciences and medical sciences *66*:421-429.

Flory, M.R., Carson, A.R., Muller, E.G., Aebersold, R. (2004). An SMC-domain protein in fission yeast links telomeres to the meiotic centrosome. Molecular Cell *16*:619–630.

Fradet-Turcotte, A., Canny, M.D., Escribano-D´ıaz, C., Orthwein, A., Leung, C.C., Huang, H., Landry, M.C., Kitevski-LeBlanc, J., Noordermeer, S.M., Sicheri, F., Durocher, D. (2013). 53BP1 is a reader of the DNA-damage-induced H2A Lys 15 ubiquitin mark. Nature *499*:50–54.

Frank, A.K., Tran, D.C., Qu, R.W., Stohr, B.A., Segal, D.J., Xu, L. (2015). The shelterin TIN2 subunit Mediates Recruitment of Telomerase to Telomeres. PLoS Genetics *11*:e1005410.

Frescas, D., de Lange, T. (2014). A TIN2 dyskeratosis congenita mutation causes telomerase-independent telomere shortening in mice. Genes & Development *28*:153-66.

Fuster, J.J., Andres, V. (2006). Telomere biology and cardiovascular disease. Circulation Research *99*:1167-1180.

Greider, C.W., Blackburn, E.H. (1985). Identification of a specific telomere terminal transferase activity in Tetrahymena extracts. Cell *43*, 405-413.

Greider, C.W., Blackburn, E.H. (1987). The telomere terminal transferase of Tetrahymena is a ribonucleoprotein enzyme with two kinds of primer specificity. Cell *51*, 887-898.

Griffith, J., Michalowski, S., Makhov, A.M. (1999). Electron microscopy of DNA-protein complexes and chromatin. Methods Enzymol *304*: 214-30.

Günes, C., Rudolph, K.L. (2013). The role of telomeres in stem cells and cancer. Cell *152*:390–393.

Hanahan, D., Weinberg, R.A. (2011). Hallmarks of cancer: the next generation. Cell *144*:646–674.

Hannan, A., Abraham, N.M., Goyal, S., Jamir, I., Priyakumar, U.D., Mishra, K. (2015). Sumoylation of Sir2 differentially regulates transcriptional silencing in yeast. Nucleic Acids Research *43*:10213–10226.

Harley, C.B. (2008). Telomerase and cancer therapeutics. Nature reviews Cancer *8*, 167-179.

Hiyama, E., Hiyama, K. (2007). Telomere and telomerase in stem cells. Br J Cancer *96*, 1020-1024.

Hockemeyer, D., Collins, K. (2015). Control of telomerase action at human telomeres. Nature Structural & Molecular Biology *22*:848–852.

Holohan, B., Wright, W.E., Shay, J.W. (2014). Cell biology of disease: Telomeropathies: an emerging spectrum disorder. The Journal of Cell Biology *205*:289–299.

Horn, S., Figl, A., Rachakonda, P.S., Fischer, C., Sucker, A., Gast, A., Kadel, S., Moll, I., Nagore, E., Hemminki, K., et al. (2013). TERT promoter mutations in familial and sporadic melanoma. Science *339*:959–961.

Horvath, M.P., Schweiker, V.L., Bevilacqua, J.M., Ruggles, J.A., Schultz, S.C. (1998). Crystal structure of the Oxytricha nova telomere end binding protein complexed with single strand DNA. Cell *95*:963–974.

Houghtaling, B.R., Cuttonaro, L., Chang, W., Smith, S. (2004). A dynamic molecular link between the telomere length regulator TRF1 and the chromosome end protector TRF2. Current Biology *14*:1621–1631.

Hu, X., Liu, J., Jun, H.I., Kim, J.K., and Qiao, F. (2016). Multi-step coordination of telomerase recruitment in fission yeast through two coupled telomere-telomerase interfaces. Elife *5*: e15470.

Huang, F.W., Hodis, E., Xu, M.J., Kryukov, G.V., Chin, L., Garraway, L.A. (2013). Highly recurrent TERT promoter mutations in human melanoma. Science *339*:957–959.

Jain, D., Cooper, J.P. (2010). Telomeric strategies: means to an end. Annual Review of Genetics *44*:243–269.

Jiang, J., Chan, H., Cash, D.D., Miracco, E.J., Ogorzalek, Loo R.R., Upton, H.E., Cascio, D., O'Brien Johnson, R., Collins, K., Loo, J.A., Zhou, Z.H., Feigon, J. (2015). Structure of Tetrahymena telomerase reveals previously unknown subunits, functions, and interactions. Science *350*:aab4070

Joseph, I., Lustig, A.J. (2007). Telomeres in meiotic recombination: the yeast side story. Cellular and Molecular Life Sciences *64*:125-30.

Jun, H.I., Liu, J., Jeong, H., Kim, J.K., Qiao, F. (2013). Tpz1 controls a telomerase-nonextendible telomeric state and coordinates switching to an extendible state via Ccq1. Genes & Development *27*:1917–1931.

Kaake, R.M., Wang, X., Burke, A., Yu, C., Kandur, W., Yang, Y., Novtisky, E.J., Second, T., Duan, J., Kao, A., et al. (2014). A new in vivo cross-linking mass spectrometry platform to define protein-protein interactions in living cells. Molecular Cell Proteomics *13*:3533–3543.

Kanoh, J., Ishikawa, F. (2001). spRap1 and spRif1, recruited to telomeres by Taz1, are essential for telomere function in fission yeast. Current Biology *11*:1624–1630.

Kao, A., Chiu, C.L., Vellucci, D., Yang, Y., Patel, V.R., Guan, S., Randall, A., Baldi, P., Rychnovsky, S.D., Huang, L. (2011). Development of a novel cross-linking strategy for fast and accurate identification of cross-linked peptides of protein complexes. Molecular Cell Proteomics *10*:M110.002212 http://dx.doi.org/10.1074/ mcp.M110.002212.

Kao, A., Randall, A., Yang, Y., Patel, V.R., Kandur, W., Guan, S., Rychnovsky, S.D., Baldi, P., Huang, L. (2012). Mapping the structural topology of the yeast 19S proteasomal regulatory particle using chemical cross-linking and probabilistic modeling. Molecular Cell Proteomics *11*:1566–1577.

Kim, J.K., Liu, J., Hu, X., Yu, C., Roskamp, K., Sankaran, B., Huang, L., Komives, E.A., Qiao, F. (2017). Structural Basis for Shelterin Bridge Assembly. Molecular Cell *68*:698-714

Kim, N.W., Piatyszek, M.A., Prowse, K.R., Harley, C.B., West, M.D., Ho, P.L., Coviello, G.M., Wright, W.E., Weinrich, S.L., Shay, J.W. (1994). Specific association of human telomerase activity with immortal cells and cancer. Science *266*:2011-5.

Kocak, H., Ballew, B.J., Bisht, K., Eggebeen, R., Hicks, B.D., Suman, S., O'Neil, A., Giri, N., Maillard, I., Alter, B.P., Keegan, C.E., Nandakumar, J., Savage, S.A., Laboratory NDCGR, Group NDCSW, NCI DCEG Cancer Genomics Research Laboratory, NCI DCEG Cancer Sequencing

Working Group. (2014). Hoyeraal-Hreidarsson syndrome caused by a germline mutation in the TEL patch of the telomere protein TPP1. Genes & Development *28*:2090–2102.

Lansdorp, P.M. (2005). Role of telomerase in hematopoietic stem cells. Ann N Y Acad Sci *1044*, 220-227.

Lee, S.S., Bohrson, C., Pike, A.M., Wheelan, S.J., Greider, C.W. (2015). ATM kinase is required for telomere elongation in mouse and human cells. Cell Reports *13*:1623–1632.

Lei, M., Podell, E.R., Baumann, P., Cech, T.R. (2003). DNA self-recognition in the structure of Pot1 bound to telomeric single-stranded DNA. Nature *426*, 198-203.

Leitner, A., Joachimiak, L.A., Unverdorben, P., Walzthoeni, T., Frydman, J., Förster, F., Aebersold, R. (2014). Chemical cross-linking/mass spectrometry targeting acidic residues in proteins and protein complexes. Proc Natl Acad Sci U S A *111*:9455–9460.

Leonardi, J., Box, J.A., Bunch, J.T., Baumann, P. (2008). TER1, the RNA subunit of fission yeast telomerase. Nature Structural & Molecular Biology *15*:26–33.

Li, S., Makovets, S., Matsuguchi, T., Blethrow, J.D., Shokat, K.M., Blackburn, E.H. (2009). Cdk1-dependent phosphorylation of Cdc13 coordinates telomere elongation during cell-cycle progression. Cell *136*:50–61.

Lim, C.J., Zaug, A.J., Kim, H.J., Cech, T.R. (2017). Reconstitution of human shelterin complexes reveals unexpected stoichiometry and dual pathways to enhance telomerase processivity. Nature Communications *8*:1075.

Lingner, J., Hughes, T.R., Shevchenko, A., Mann, M., Lundblad, V., Cech, T.R. (1997). Reverse transcriptase motifs in the catalytic subunit of telomerase. Science *276*:561–567.

Liu, C.C., Gopalakrishnan, V., Poon, L.F., Yan, T., Li, S. (2014). Cdk1 regulates the temporal recruitment of telomerase and Cdc13-Stn1-Ten1 complex for telomere replication. Molecular and Cellular Biology *34*:57–70.

Liu, D., Safari, A., O'Connor, M.S., Chan, D.W., Laegeler, A., Qin, J., Songyang, Z. (2004). PTOP interacts with POT1 and regulates its localization to telomeres. Nature Cell Biology *6*:673–680.

Liu, J., Yu, C., Hu, X., Kim, J.K., Bierma, J.C., Jun, H.I., Rychnovsky, S.D., Huang, L., Qiao, F. (2015). Dissecting fission yeast shelterin interactions via MICro-MS links disruption of shelterin bridge to tumorigenesis. Cell Reports *12*:2169–2180.

Loayza, D., de Lange, T. (2003). POT1 as a terminal transducer of TRF1 telomere length control. Nature *423*:1013–1018.

Lundblad, V., Szostak, J.W. (1989). A mutant with a defect in telomere elongation leads to senescence in yeast. Cell *57*:633–643.

Marks, D.S., Colwell, L.J., Sheridan, R., Hopf, T.A., Pagnani, A., Zecchina, R., Sander, C. (2011). Protein 3D structure computed from evolutionary sequence variation. PLoS ONE *6*:e28766.

McEachern, M.J., Blackburn, E.H. (1994). A conserved sequence motif within the exceptionally diverse telomeric sequences of budding yeasts. Proc Natl Acad Sci U S A. *91*:3453-7.

Meyne, J., Baker, R.J., Hobart, H.H., Hsu, T.C., Ryder, O.A., Ward, O.G., Wiley, J.E., Wurster-Hill, D.H., Yates, T.L., Moyzis, R.K. (1990). Distribution of non-telomeric sites of the (TTAGGG)n telomeric sequence in vertebrate chromosomes. Chromosoma *99*: 3-10.

Miyagawa, K., Low, R.S., Santosa, V., Tsuji, H., Moser, B.A., Fujisawa, S., Harland, J.L., Raguimova, O.N., Go, A., Ueno, M., Matsuyama, A., Yoshida, M., Nakamura, T.M., Tanaka, K. (2014). SUMOylation regulates telomere length by targeting the shelterin subunit Tpz1(Tpp1) to modulate shelterin-Stn1 interaction in fission yeast. Proc Natl Acad Sci U S A *111*:5950–5955.

Miyoshi, T., Kanoh, J., Saito, M., Ishikawa, F. (2008). Fission yeast Pot1-Tpp1 protects telomeres and regulates telomere length. Science *320*:1341–1344.

Mizushima, S., Nomura, M. (1970). Assembly mapping of 30S ribosomal proteins from E. coli. Nature *226*, 1214.

Moser, B.A., Chang, Y.T., Kosti, J., Nakamura, T.M. (2011). Tel1ATM and Rad3ATR kinases promote Ccq1-Est1 interaction to maintain telomeres in fission yeast. Nature Structural & Molecular Biology *18*:1408–1413.

Moser, B.A., Subramanian, L., Khair, L., Chang, Y.T., Nakamura, T.M. (2009). Fission yeast Tel1(ATM) and Rad3(ATR) promote telomere protection and telomerase recruitment. PLoS Genetics *5*:e1000622.

Moyzis, R.K., Buckingham, J.M., Cram, L.S., Dani, M., Deaven, L.L., Jones, M.D., Meyne, J., Ratliff, R.L., Wu, J.R. (1988). A highly conserved repetitive DNA sequence, (TTAGGG)n, present at the telomeres of human chromosomes. Proc Natl Acad Sci U S A *85*: 6622-6.

Murray, A.W., Schultes, N.P., Szostak, J.W. (1986). Chromosome length controls mitotic chromosome segregation in yeast. Cell *45*:529-36.

Nakamura, T.M., Morin, G.B., Chapman, K.B., Weinrich, S.L., Andrews, W.H., Lingner, J., Harley, C.B., Cech, T.R. (1997). Telomerase catalytic subunit homologs from fission yeast and human. Science *277*:955–959.

Nandakumar, J., Cech, T.R. (2012). DNA-induced dimerization of the single-stranded DNA binding telomeric protein Pot1 from Schizosaccharomyces pombe. Nucleic acids research *40*, 235-244.

Nandakumar, J., Bell, C.F., Weidenfeld, I., Zaug, A.J., Leinwand, L.A., Cech, T.R. (2012). The TEL patch of telomere protein TPP1 mediates telomerase recruitment and processivity. Nature *492*:285–289.

Nandakumar, J., Cech, T.R. (2013). Finding the end: recruitment of telomerase to telomeres. Nature Reviews Molecular Cell Biology *14*:69–82.

O'Connor, M.S., Safari, A., Xin, H., Liu, D., Songyang, Z. (2006). A critical role for TPP1 and TIN2 interaction in high-order telomeric complex assembly. Proc Natl Acad Sci U S A *103*, 11874-11879.

Ovchinnikov, S., Kamisetty, H., Baker, D. (2014). Robust and accurate prediction of residue-residue interactions across protein interfaces using evolutionary information. eLife *3*:e02030.

Palm, W., de Lange, T. (2008). How shelterin protects mammalian telomeres. Annual Review of Genetics *42*:301–334.

Pan, L., Hildebrand, K., Stutz, C., Thoma, N., Baumann, P. (2015). Minishelterins separate telomere length regulation and end protection in fission yeast. Genes & development *29*, 1164-1174.

Pathare, G.R., Nagy, I., Śledź, P., Anderson, D.J., Zhou, H.J., Pardon, E., Steyaert, J., Förster, F., Bracher, A., Baumeister, W. Crystal structure of the proteasomal deubiquitylation module Rpn8-Rpn11. Proc Natl Acad Sci U S A *111*:2984–2989.

Pennock, E., Buckley, K., Lundblad, V. (2001). Cdc13 delivers separate complexes to the telomere for end protection and replication. Cell *104*:387–396.

Politis, A., Stengel, F., Hall, Z., Hernández, H., Leitner, A., Walzthoeni, T., Robinson, C.V., Aebersold, R. (2014). A mass spectrometry-based hybrid method for structural modeling of protein complexes. Nature Methods *11*:403–406.

Qi, H., Zakian, V.A. (2000). The Saccharomyces telomere-binding protein Cdc13p interacts with both the catalytic subunit of DNA polymerase alpha and the telomerase-associated est1 protein. Genes & Development *14*:1777–1788.

Qiao, F., Cech, T.R. (2008). Triple-helix structure in telomerase RNA contributes to catalysis. Nature Structural & Molecular Biology *15*:634-40.

Ramsay, A.J., Quesada, V., Foronda, M., Conde, L., Martínez-Trillos, A., Villamor, N., Rodríguez, D., Kwarciak, A., Garabaya, C., Gallardo, M., et al. (2013). POT1 mutations cause telomere dysfunction in chronic lymphocytic leukemia. Nature Genetics *45*:526–530.

Robles-Espinoza, C.D., Harland, M., Ramsay, A.J., Aoude, L.G., Quesada, V., Ding, Z., Pooley, K.A., Pritchard, A.L., Tiffen, J.C., Petljak, M., et al. (2014). POT1 loss-of-function variants predispose to familial melanoma. Nature Genetics *46*:478–481.

Sabourin, M., Tuzon, C.T., Zakian, V.A. (2007). Telomerase and Tel1p preferentially associate with short telomeres in S. cerevisiae. Molecular Cell *27*:550–561.

Saliques, S., Zeller, M., Lorin, J., Lorgis, L., Teyssier, J.R., Cottin, Y., Rochette, L., Vergely, C. (2010). Telomere length and cardiovascular risk in hypertensive patients with leftventricular hypertrophy: the LIFE study. Archives of Cardiovascular Diseases *103*:454-459.

Sarek, G., Marzec, P., Margalef, P., Boulton, S.J. (2015). Molecular basis of telomere dysfunction in human genetic diseases. Nature Structural & Molecular Biology *22*:867–874.

Sato, M., Dhut, S., Toda, T. (2005). New drug-resistant cassettes for gene disruption and epitope tagging in Schizosaccharomyces pombe. Yeast *22*:583–591.

Schmidt, J.C., Cech, T.R. (2015). Human telomerase: biogenesis., trafficking., recruitment., and activation. Genes & Development *29*:1095–1105.

Schmidt, J.C., Dalby, A.B., Cech, T.R. (2014). Identification of human TERT elements necessary for telomerase recruitment to telomeres. eLife *3*:e03563.

Scott, H., Kim, J.K., Yu, C., Huang, L., Qiao, F., and Taylor, D.J. (2017). Spatial Organization and Molecular Interactions of the Schizosaccharomyces pombe Ccq1-Tpz1-Poz1 Shelterin Complex. Journal of molecular biology 429, 2863-2872.

Seto, A.G., Livengood, A.J., Tzfati, Y., Blackburn, E.H., Cech, T.R. (2002) A bulged stem tethers Est1p to telomerase RNA in budding yeast. Genes & Development *16*:2800–2812.

Sexton, A.N., Regalado, S.G., Lai, C.S., Cost, G.J., O'Neil, C.M., Urnov, F.D., Gregory, P.D., Jaenisch, R., Collins, K., Hockemeyer, D. (2014). Genetic and molecular identification of three human TPP1 functions in telomerase action: recruitment, activation, and homeostasis set point regulation. Genes & Development *28*:1885–1899.

Sexton, A.N., Youmans, D.T., Collins, K. (2012). Specificity requirements for human telomere protein interaction with telomerase holoenzyme. The Journal of Biological Chemistry *287*:34455–34464.

Shampay, J., Szostak, J.W., Blackburn, E.H. (1984). DNA sequences of telomeres maintained in yeast. Nature *310*:154-7.

Shay, J.W., Wright, W.E. (1996). Telomerase activity in human cancer. Curr Opin Oncol *8*, 66-71.

Shay, J.W., Wright, W.E. (2010). Telomeres and telomerase in normal and cancer stem cells. FEBS letters *584*, 3819-3825.

Shi, J., Yang, X.R., Ballew, B., Rotunno, M., Calista, D., Fargnoli, M.C., Ghiorzo, P., Bressac-de Paillerets, B., Nagore, E., Avril, M.F., et al. (2014). NCI DCEG Cancer Sequencing Working Group; NCI DCEG Cancer Genomics Research Laboratory; French Familial Melanoma Study Group. Rare missense variants in POT1 predispose to familial cutaneous malignant melanoma. Nature Genetics *46*:482–486.

Speedy, H.E., Di Bernardo, M.C., Sava, G.P., Dyer, M.J., Holroyd, A., Wang, Y., Sunter, N.J., Mansouri, L., Juliusson, G., Smedby, K.E., et al. (2014). A genome-wide association study identifies multiple susceptibility loci for chronic lymphocytic leukemia. Nature Genetics *46*:56–60.

Spyridopoulos, I., Dimmeler, S. (2007). Can telomere length predict cardiovascular risk? Lancet *369*:81-82.

Stewart, S.A., Weinberg, R.A. (2006). Telomeres: cancer to human aging. Annual Review of Cell and Developmental Biology *22*:531-57.

Sugiyama, T., Cam, H.P., Sugiyama, R., Noma, K., Zofall, M., Kobayashi, R., Grewal, S.I. (2007). SHREC, an effector complex for heterochromatic transcriptional silencing. Cell *128*:491–504.

Taboski, M.A., Sealey, D.C., Dorrens, J., Tayade, C., Betts, D.H., Harrington, L. (2012). Long telomeres bypass the requirement for telomere maintenance in human tumorigenesis. Cell Reports *1*:91–98.

Tadeo, X., Wang, J., Kallgren, S.P., Liu, J., Reddy, B.D., Qiao, F., Jia, S. (2013). Elimination of shelterin components bypasses RNAi for pericentric heterochromatin assembly. Genes & Development *27*:2489–2499.

Takai, K.K., Kibe, T., Donigian, J.R., Frescas, D., de Lange, T. (2011). Telomere protection by TPP1/POT1 requires tethering to TIN2. Molecular Cell *44*:647-659.

Talkington, M.W., Siuzdak, G., Williamson, J.R. (2005). An assembly landscape for the 30S ribosomal subunit. Nature *438*, 628-632.

Tefferi, A., Lasho, T.L., Begna, K.H., Patnaik, M.M., Zblewski, D.L., Finke, C.M., Laborde, R.R., Wassie, E., Schimek, L., Hanson, C.A*., et al.* (2015). A Pilot Study of the Telomerase Inhibitor Imetelstat for Myelofibrosis. The New England journal of medicine *373*, 908-919.

Teixeira, M.T., Arneric, M., Sperisen, P., Lingner, J. (2004). Telomere length homeostasis is achieved via a switch between telomerase-extendible and -nonextendible states. Cell *117*, 323-335.

Tomita, K., Cooper, J.P. (2008). Fission yeast Ccq1 is telomerase recruiter and local checkpoint controller. Genes & Development *22*:3461–3474.

Tong, A.S., Stern, J.L., Sfeir, A., Kartawinata, M., de Lange, T., Zhu, X.D., Bryan, T.M. (2015). ATM and ATR signaling regulate the recruitment of human telomerase to telomeres. Cell Reports *13*:1633–1646.

Tucey, T.M., Lundblad, V. (2014). Regulated assembly and disassembly of the yeast telomerase quaternary complex. Genes & Development *28*:2077–2089.

Velázquez-Muriel, J., Lasker, K., Russel, D., Phillips, J., Webb, B.M., Schneidman-Duhovny, D., Sali, A. (2012). Assembly of macromolecular complexes by satisfaction of spatial restraints from electron microscopy images. Proc Natl Acad Sci U S A *109*:18821–18826.

Walzthoeni, T., Leitner, A., Stengel, F., Aebersold, R. (2013). Mass spectrometry supported determination of protein complex structure. Current Opinion in Structural Biology *23*:252–260.

Wang, F., Podell, E.R., Zaug, A.J., Yang, Y., Baciu, P., Cech, T.R., Lei, M. (2007). The POT1-TPP1 telomere complex is a telomerase processivity factor. Nature *445*:506–510.

Watson, J.D., Crick, F.H. (1953). Molecular structure of nucleic acids; a structure for deoxyribose nucleic acid. Nature *171*:737-8.

Webb, C.J., Zakian, V.A. (2008). Identification and characterization of the Schizosaccharomyces pombe TER1 telomerase RNA. Nature Structural & Molecular Biology *15*:34–42.

Webb, C.J., Zakian, V.A. (2012). Schizosaccharomyces pombe Ccq1 and TER1 bind the 14-3-3-like domain of Est1, which promotes and stabilizes telomerase-telomere association. Genes & Development *26*:82–91.

Weigt, M., White, R.A., Szurmant, H., Hoch, J.A., Hwa, T. (2009). Identification of direct residue contacts in protein-protein interaction by message passing. Proc Natl Acad Sci U S A *106*:67–72.

Wellinger, R.J., Zakian, V.A. (2012) Everything You Ever Wanted toKnow About Saccharomyces cerevisiae Telomeres: Beginning to End. Genetics *191*:1073-105.

Williamson, J.R. (2008). Cooperativity in macromolecular assembly. Nature chemical biology *4*, 458-465.

Worden, E.J., Padovani, C., Martin, A. (2014). Structure of the Rpn11-Rpn8 dimer reveals mechanisms of substrate deubiquitination during proteasomal degradation. Nature Structural & Molecular Biology *21*:220–227.

Yamazaki, H., Tarumoto, Y., Ishikawa, F. (2012). Tel1(ATM) and Rad3(ATR) phosphorylate the telomere protein Ccq1 to recruit telomerase and elongate telomeres in fission yeast. Genes & Development *26*:241–246.

Yang, B., Wu, Y.J., Zhu, M., Fan, S.B., Lin, J., Zhang, K., Li, S., Chi, H., Li, Y.X., Chen, H.F., et al. (2012). Identification of cross-linked peptides from complex samples. Nature Methods *9*:904–906.

Yang, D., He, Q., Kim, H., Ma, W., Songyang, Z. (2011). TIN2 protein dyskeratosis congenita missense mutants are defective in association with telomerase. The Journal of Biological Chemistry *286*:23022–23030.

Ye, J.Z., Hockemeyer, D., Krutchinsky, A.N., Loayza, D., Hooper, S.M., Chait, B.T., de Lange, T. (2004). POT1- interacting protein PIP1: a telomere length regulator that recruits POT1 to the TIN2/TRF1 complex. Genes & Development *18*:1649–1654.

Zappulla, D.C., Cech, T.R. (2004). Yeast telomerase RNA: A flexible scaffold for protein subunits. Proc Natl Acad Sci U S A *101*:10024–10029.

Zappulla, D.C., Goodrich, K., Cech, T.R. (2005). A miniature yeast telomerase RNA functions in vivo and reconstitutes activity in vitro. Nature Structural & Molecular Biology *12*:1072-7.

Zhao, B., Shu, C., Gao, X., Sankaran, B., Du, F., Shelton, C.L., Herr, A.B., Ji, J.Y., Li, P. (2016). Structural basis for concerted recruitment and activation of IRF-3 by innate immune adaptor proteins. Proc Natl Acad Sci U S A *113*, E3403-3412.

Zhong, F.L., Batista, L.F., Freund, A., Pech, M.F., Venteicher, A.S., Artandi, S.E. (2012). TPP1 OB-fold domain controls telomere maintenance by recruiting telomerase to chromosome ends. Cell *150*:481–494.

APPENDIX

CHAPTER 3: Dissecting Fission Yeast Shelterin Interactions via MICro-MS Links Disruption of Shelterin Bridge to Tumorigenesis

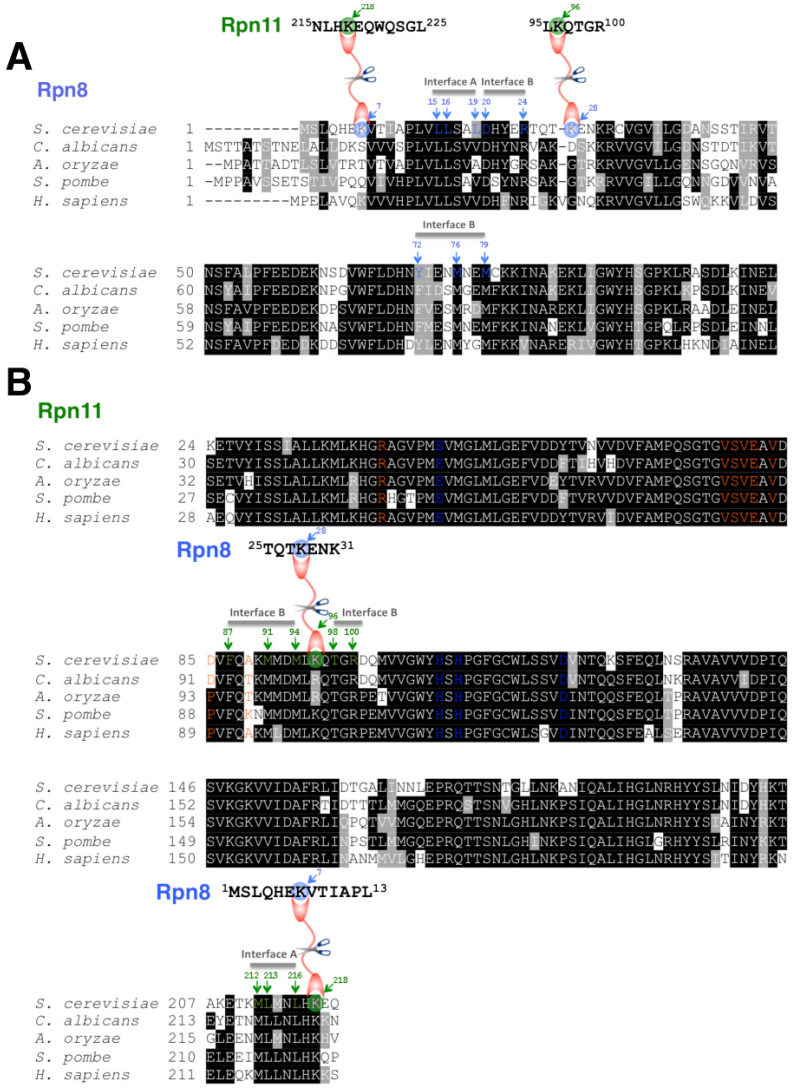

Figure S1. (Related to Figure 2) Sequence alignments of Rpn8 **(A)** and Rpn11 **(B)** from fungi to human. Identical residues are highlighted in black, and chemically similar residues are highlighted in gray. The crosslinked lysine residues are highlighted in blue and green for Rpn8 and Rpn11, respectively. Crosslinked peptides are shown on the top with crosslinked lysines indicated. The residues colored in blue or green with residue numbers above are the contact residues observed in the interface from the crystal structure from Rpn8 and Rpn11, respectively. In sequence alignment of Rpn11 (B), Zn^{2+}-coordinating residues are colored in blue and residues involved in catalysis are in red.

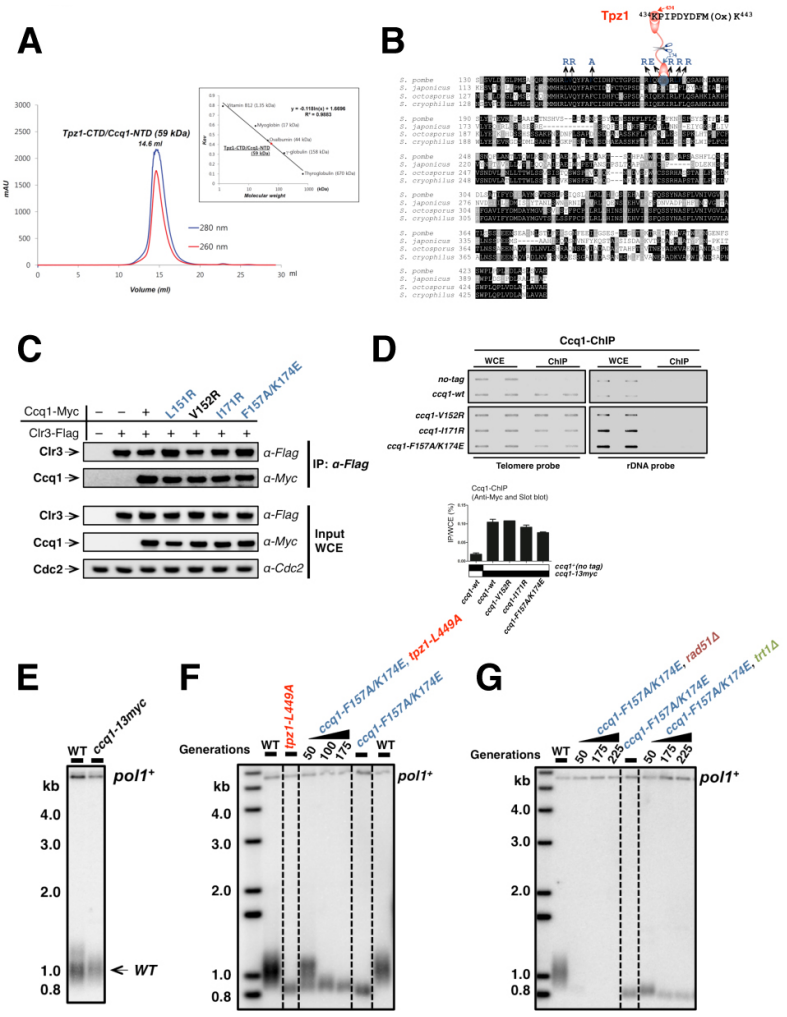

Figure S2. (Related to Figure 3) **(A)** Gel filtration chromatography showing Tpz1-CTD and Ccq1-NTD complex forms a dimer of the Tpz1-CTD/Ccq1-NTD heterodimer. **(B)** Sequence alignment of Ccq1 from four different fission yeast species. The crosslinked lysine is highlighted in dark blue with corresponding Tpz1 fragment on the top. The targeted residues for mutation are colored in dark blue and were mutated to the amino acids indicated above them. **(C)** Co-immunoprecepitation (co-IP) assays evaluating the binding between Clr3 and Ccq1 mutants. The mutants colored in dark blue are Tpz1-binding deficient. Cdc2 was shown as the loading control. Input: 1/30 of input WCE (whole cell extract). **(D)** Localization of Ccq1 mutants to telomere is monitored by ChIP assay. Slot-blot was used to visualize telomeric association of Ccq1 in each genetic background. Telomeric enrichment of Ccq1 was expressed as immunoprecipitate (IP)/whole-cell extract (WCE) from the telomere DNA probe hybridization. The same membrane was stripped and then hybridized with the rDNA probe. Error bars in the quantitation of the slot blot analysis represent standard deviations of two individual repeats. **(E)** *ccq1-wt-13myc* has wild-type telomere length. Therefore, C-terminal tagging of *ccq1⁺* does not interfere with telomere maintenance. **(F)** *ccq1-F157A/K174E tpz1-L449A* double-mutant cells have identical telomere phenotype as either *ccq1-F157A/K174E or tpz1-L449A* cells. (G) Telomere maintenance in *ccq1-F157A/K174E* cells is not telomerase dependent, but HR dependent.

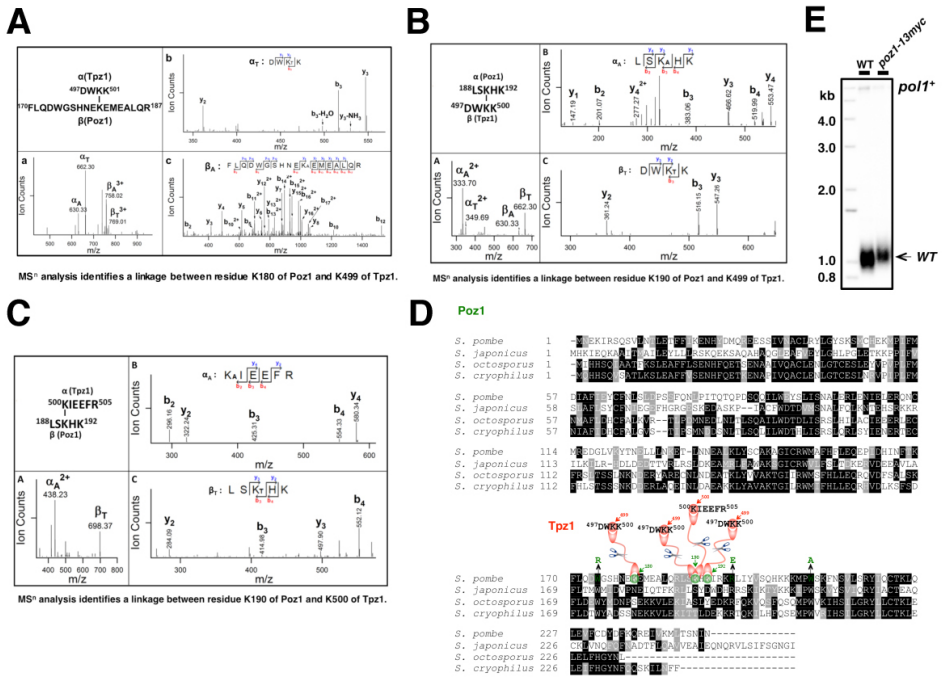

Figure S3. (Related to Figure 4) **(A)** MS^n analysis of a DSSO crosslinked peptide representing an interaction between Poz1 and Tpz1. (a) MS^2 spectrum of a quadruply-charged crosslinked peptide α-β (m/z 739.5940^{4+}) in which two characteristic peptide fragment pairs were detected: α_T/β_A (m/z $662.30^{+}/758.02^{3+}$) and α_A/β_T (m/z $630.33^{+}/769.01^{3+}$) with defined modifications. Respective MS^3 spectra of (b) α_T (m/z 662.30^{+}) and (c) β_A (m/z 758.02^{3+}) fragment ions unambiguously identified their sequences as DWK_TK of Tpz1 and $FLQDWGSHNEK_AEMEALQR$ of Poz1. This identifies a linkage between residue K180 of Poz1 and K499 of Tpz1. **(B)** MS^n analysis of a DSSO crosslinked peptide representing an interaction between Poz1 and Tpz1. (a) MS^2 analysis of a triply-charged parent ion α-β (m/z 449.2354^{3+}) in which two characteristic peptide fragment pairs were detected: α_A/β_T (m/z $333.70^{2+}/662.30^{+}$) and α_T/β_A (m/z $349.69^{2+}/630.33^{+}$), unique to DSSO inter-linked peptides; MS^3 spectra of (b) α_A (m/z 333.70^{2+}) and (c) β_T (m/z 662.30^{+}) fragment ions detected in (a), which unambiguously identify their sequences as LSK_AHK of Poz1 and DWK_TK of Tpz1, respectively. This identifies a linkage between residue K190 of Poz1 and K499 of Tpz1. Note: K_A: alkene modified lysine; K_T: unsaturated thiol modified lysine. **(C)** MS^n analysis of a DSSO crosslinked peptide representing an interaction between Poz1 and Tpz1. (a) MS^2 spectrum of a triply-charged parent ion α-β (m/z 530.9461^{3+}), in which a characteristic peptide fragment pair was detected: α_A/β_T (m/z $438.23^{2+}/698.37^{+}$), unique to DSSO inter-linked peptides; MS^3 spectra of (b) α_A (m/z 438.23^{2+}) and (c) β_T (m/z 698.37^{+}) fragment ions detected in (a), which unambiguously identified their sequences as K_AIEEFR of Tpz1 and LSK_THK of Poz1, respectively, indicating a linkage between residue K190 of Poz1 and K500 of Tpz1. Note: K_A: alkene modified lysine; K_T: unsaturated thiol modified lysine. **(D)** Sequence alignment of Poz1 from four different fission yeast species. The crosslinked lysines are highlighted in dark blue with corresponding Tpz1 peptide fragments on the top. The targeted residues for mutation are colored in green and were mutated to the amino acids indicated above them. **(E)** *poz1-wt-13myc* has wild-type telomere length. Therefore, C-terminal tagging of *poz1⁺* does not interfere with telomere maintenance.

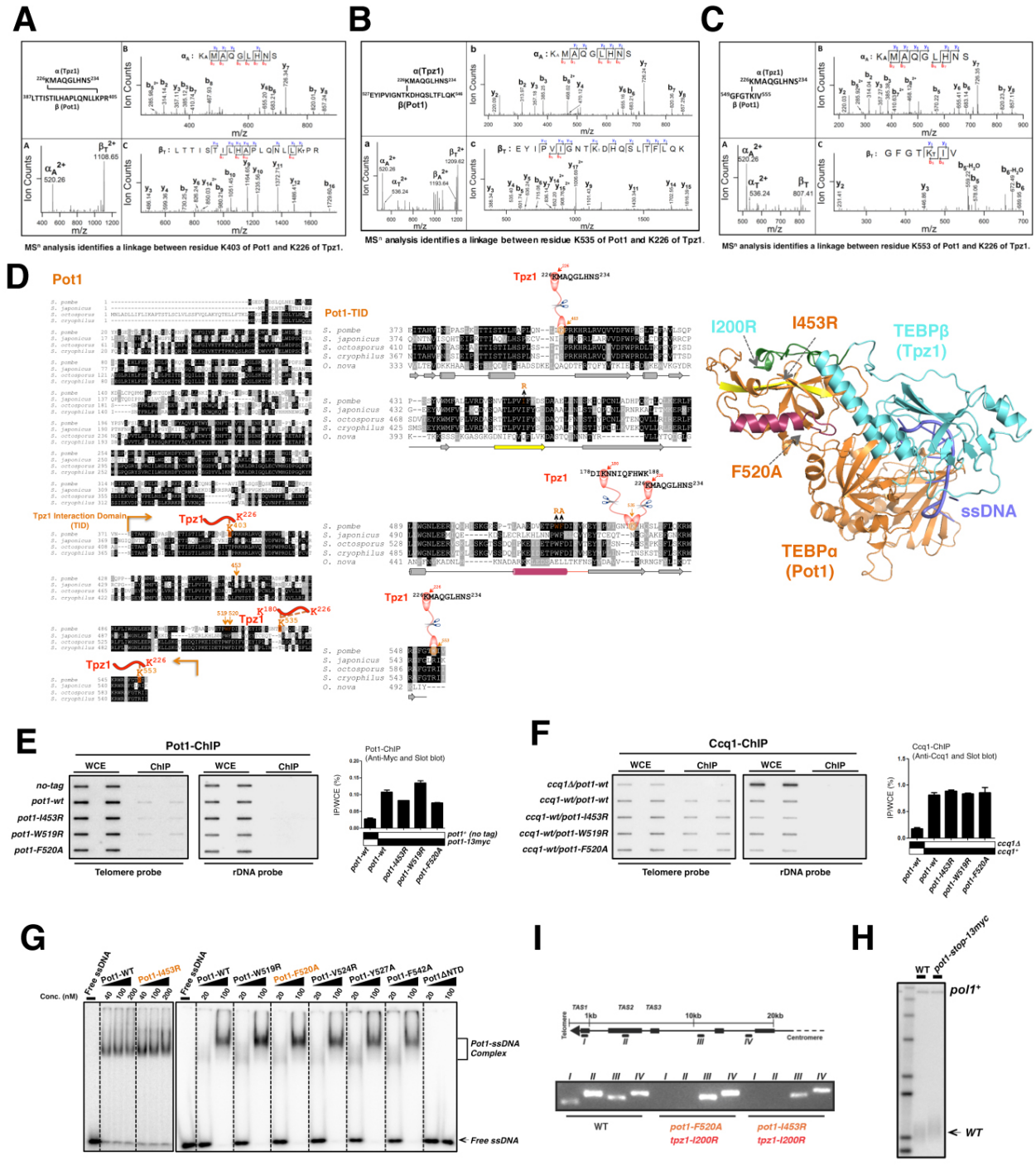

Figure S4. (Related to Figure 5) See next page for legend.

Figure S4. (Related to Figure 5) **(A)** MS^n analysis of a DSSO crosslinked representing an interaction between Pot1 and Tpz1. (a) MS^2 spectrum of a triply-charged parent ion α-β ($m/z\ 818.7060^{4+}$), in which a characteristic peptide fragment pair was detected: α_A/β_T ($m/z\ 520.26^{2+}/1108.65^{2+}$), unique to DSSO inter-linked peptides; MS^3 spectra of (b) α_A ($m/z\ 520.26^{2+}$) and (c) β_T ($m/z\ 1108.65^{2+}$) fragment ions detected in (a), which unambiguously identified their sequences as K_AMAQGLHNS of Tpz1 and LTTISTILHAPLQNLLK_TPR of Pot1, respectively, indicating a linkage between residue K403 of Pot1 and K226 of Tpz1. Note: K_A: alkene modified lysine; K_T: unsaturated thiol modified lysine. **(B)** MS^n analysis of a DSSO crosslinked peptide representing an interaction between Pot1 and Tpz1. (a) MS^2 spectrum of a quadruply-charged crosslinked parent ion α-β ($m/z\ 869.196^{4+}$), in which two characteristic peptide fragment pairs were detected: α_A/β_T ($m/z\ 520.26^{2+}/1209.62^{2+}$) and α_T/β_A ($m/z\ 536.24^{2+}/1193.64^{2+}$), unique to DSSO inter-linked peptides. MS^3 spectra of (b) α_A ($m/z\ 520.26^{2+}$) and (c) β_T ($m/z\ 1209.62^{2+}$) fragment ions unambiguously identified their sequences as K_AMAQGLHNS of Tpz1 and EYIPVIGNTK_TTDHQSLTFLQK of Pot1, respectively, indicating a linkage between residues K535 of Pot1 and K226 of Tpz1. **(C)** MS^n analysis of a DSSO crosslinked peptide representing an interaction between Pot1 and Tpz1. (a) MS^2 spectrum of the triply-charged parent ion α-β ($m/z\ 621.9794^{3+}$) in which three characteristic peptide fragments were detected: α_A/β_T ($m/z\ 520.26^{2+}/807.41^{1+}$) and α_T ($m/z\ 536.24^{2+}$) , unique to DSSO inter-linked peptides; MS^3 spectra of (b) α_A ($m/z\ 520.26^{2+}$) and (c) β_T ($m/z\ 807.41^{1+}$) fragment ions detected in (a), which unambiguously identified their sequences as K_AMAQGLHNS of Tpz1 and GFGTK_TIV of Pot1 respectively. This demonstrates a linkage between residue K553 of Pot1 and K226 of Tpz1. Note: K_A: alkene modified lysine; K_T: unsaturated thiol modified lysine. **(D)** Left: Sequence alignment of Pot1 from four different fission yeast species. The crosslinked lysines are highlighted in light brown with the corresponding Tpz1 fragment (colored in red) shown on the top. The crosslinked lysines all fall in the Tpz1-interacting region, which is indicated by two arrows colored in light brown. Middle: An enlarged view of the Tpz1-interacting region of Pot1. The selected residues of Pot1 for mutation are colored in light brown and mutated to the amino acids indicated above them. Right: Structural representation of *Oxytricha nova* TEBPα /TEBPβ complex, an ortholog of Tpz1/Pot1 complex. The loop region of TEBPβ that mediates protein-protein interaction between TEBP-α and -β is colored green and the location of a previously identified Tpz1 mutant I200R that disrupts Tpz1-Pot1 interaction is indicated. The locations two Pot1 mutants (I453R and F520A) identified in this study, based on sequence alignment, are also indicated by arrows. The structural elements in which I453R and F520A reside in are color yellow and dark red, respectively. **(E)** Telomere localization of Pot1 mutants is monitored by ChIP assay. Slot-blot was used to quantitate telomeric association of Pot1 in each genetic background. Error bars in the quantitation of the slot-blot represent standard deviations of two individual repeats. **(F)** Telomere localization of Ccq1 to telomere is monitored by ChIP assay in Pot1 mutant strains. Slotblot was used to visualize telomere association of Ccq1 in each Pot1 mutant background. Error bars in the quantitation of the slot-blot analysis represent standard deviations of two individual repeats. **(G)** Gel-shift experiments evaluating the binding ability of Pot1 mutants to a ^{32}P-labled telomeric ssDNA. The position of unbound telomeric ssDNA in the gel is indicated by an arrow. The Tpz1-binding defective mutants are colored in light brown. Pot1ΔNTD is a Pot1 truncation variant without N-terminal OB1-OB2 domains, serving as a negative control.
See next page for rest legend.

Figure S4. (Related to Figure 5) **(H)** *pot1-wt-stop-13myc* has wild-type telomere length. Therefore, selection cassette insertion does not affect telomere maintenance. **(I)** Upper: Schematic diagram of chromosome showing sub-telomeric regions. Greek numbers indicate the locations where the PCR primers are designed. Lower: *pot1-F520A/tpz1-I200R* and *pot1- I453R/tpz1-I200R* mutants lost sub-telomeric I and II regions. The PCR products (from I to IV) are amplified from corresponded regions on chromosomes (upper diagram). For pombe cells carrying circular chromosomes due to telomere deprotection, both sub-telomeric regions I and II are eroded from chromosome ends.

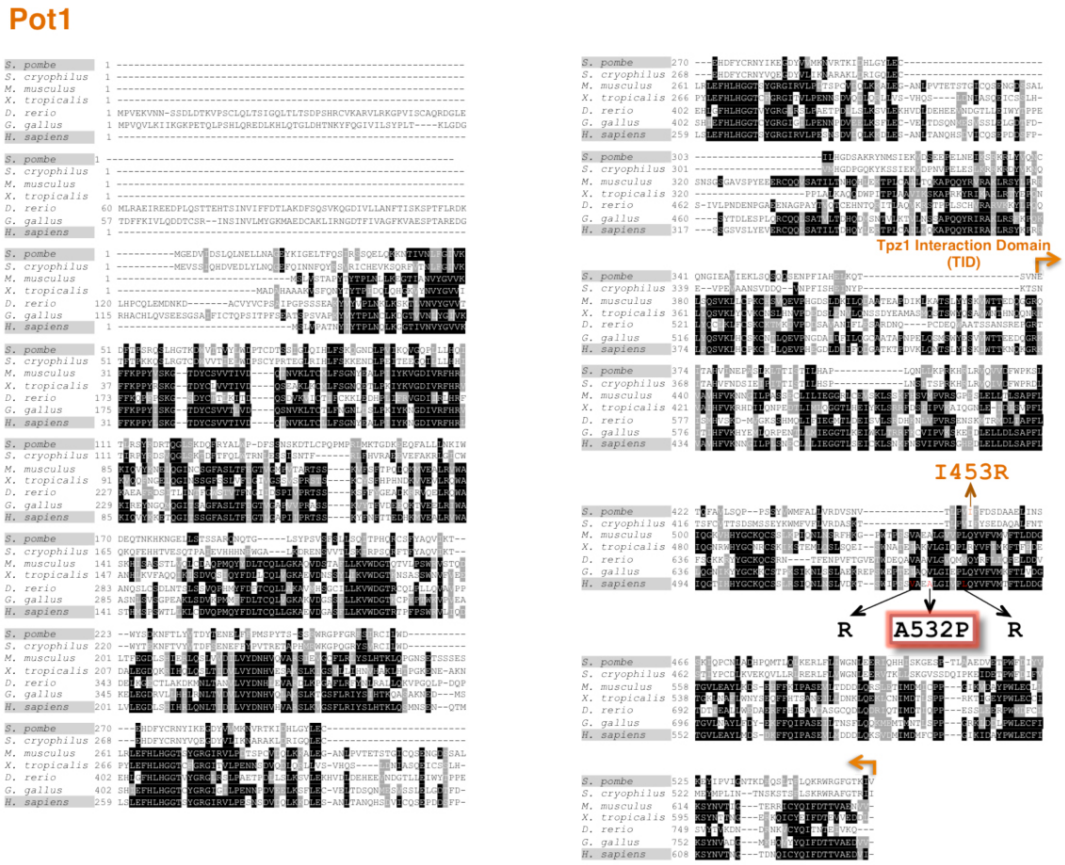

Figure S5. (Related to Figure 6) Sequence alignment of Pot1 from fission yeast to different vertebrates. The *S. pombe* Pot1 and human POT1 are highlighted in grey. Tpz1-interacting region is indicated by two arrows. In the sequence alignment, the Tpz1-binding defective mutant of *S. pombe* Pot1-I453R (colored in light brown) resides in the corresponding region of human POT1-A532P identified in familial melanoma patients (highlighted in red box).

CHAPTER 4: Multi-step coordination of telomerase recruitment in fission yeast through two coupled telomere-telomerase interfaces

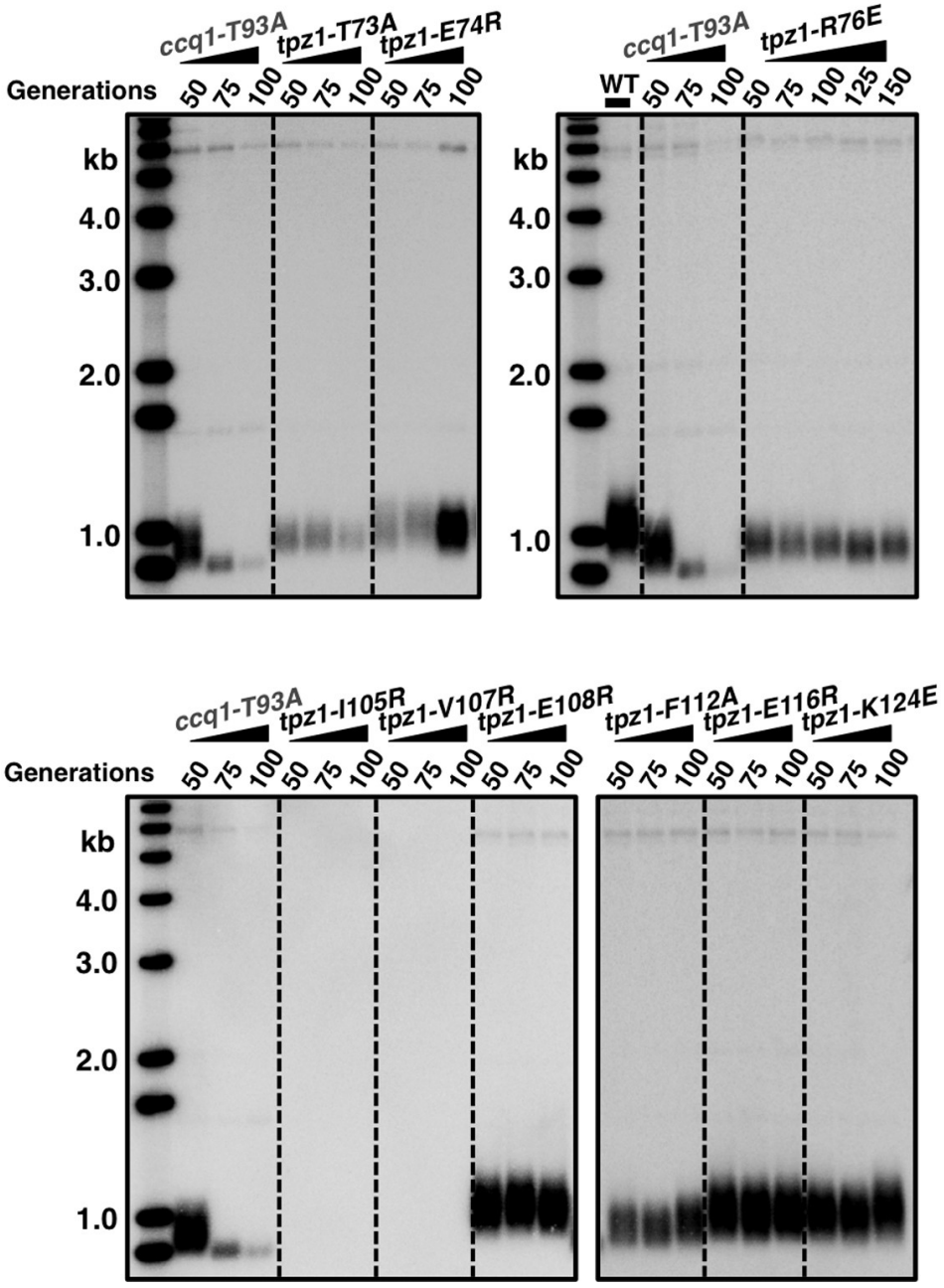

Figure 1—figure supplement 1. Telomere length measurement of tpz1 mutant strains. Southern blot analysis to measure telomere lengths using EcoRI-digested genomic DNA visualized by the telomere DNA probe for the indicated tpz1 mutant strains from successive re-streaks on agar plates.

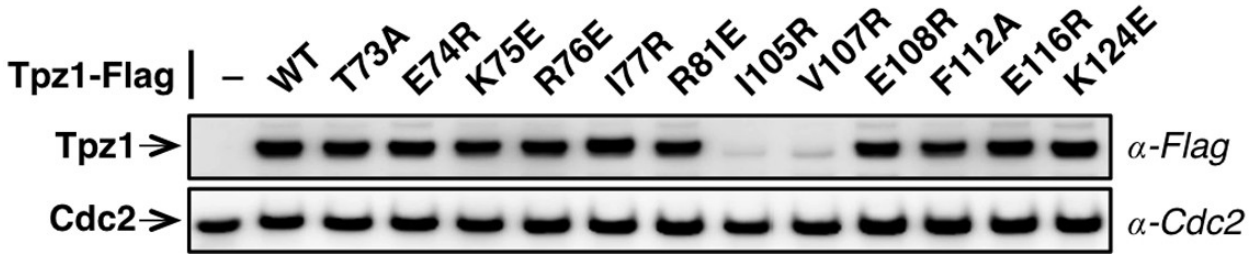

Figure 1—figure supplement 2. Evaluation of Tpz1 expression levels in tpz1 mutant strains. Western blot showing expression levels of Tpz1 protein in indicated tpz1 mutant strains.

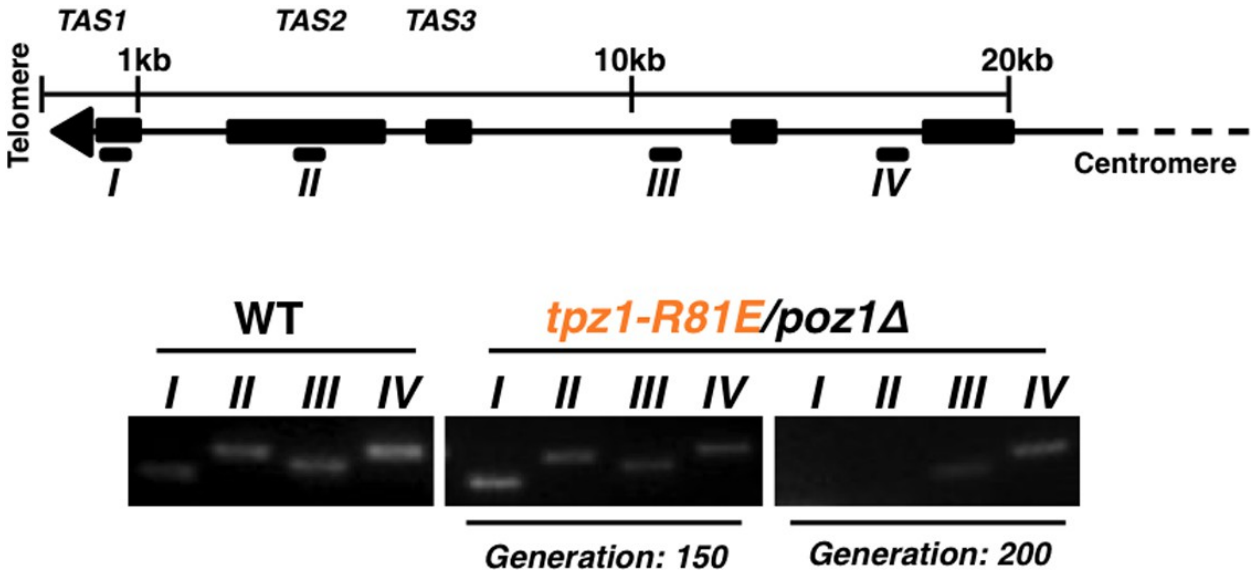

Figure 1—figure supplement 3. The later generation tpz1-R81E/poz1Δ mutant strain forms circularized chromosomes. (A) Schematic diagram of chromosome showing sub-telomeric regions. Greek numbers indicate the locations where the PCR primers are designed. **(B)** *tpz1-R81E/poz1Δ* mutant lost sub-telomeric I and II regions at generation 200. The PCR products (from I to IV) are amplified from corresponding regions on chromosomes (A). For *S. pombe* cells carrying circularized chromosomes due to telomere loss, both sub-telomeric regions I and II are eroded from chromosome ends.

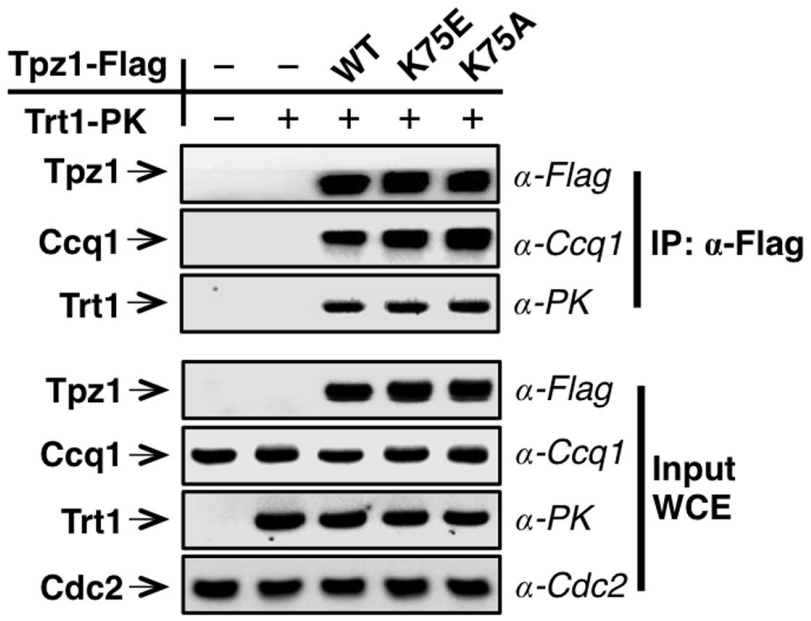

Figure 2—figure supplement 1. Trt1-Tpz1 interaction is intact in tpz1-K75E and tpz1-K75A strains. Co-immunoprecepitation (Co-IP) assays evaluating the binding between full-length Trt1 and Tpz1 mutants K75E and K75A. Cdc2 was shown as the loading control. Input: 1/30 of input WCE (whole cell extract).

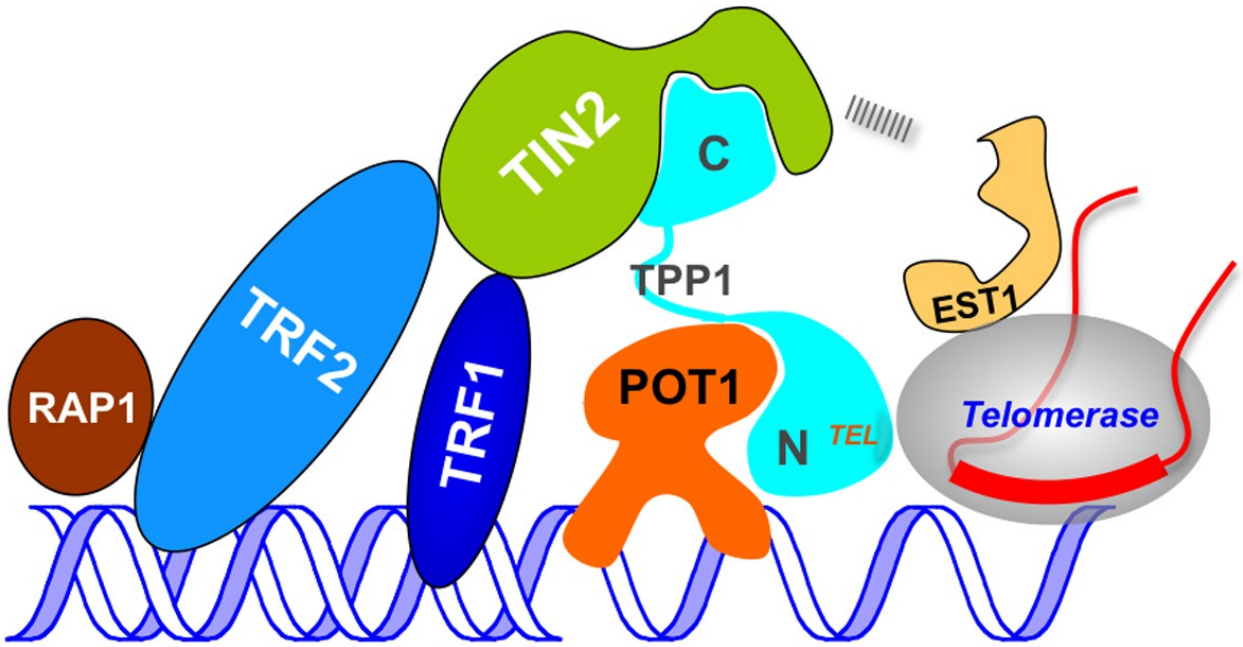

Figure 7—figure supplement 1. A speculative two-interface intermediate-state model for human telomerase recruitment. A speculative two-interface intermediate-state model for human telomerase recruitment showing that the C-terminal domain of TIN2 is likely to be the Ccq1-functional equivalent in humans and interacts either with hEST1 or the telomerase RNP directly, forming the second connection between telomeres and telomerase in addition to the TPP1 (TEL-patch)-TERT (TEN domain) interaction.

CHAPTER 5: Structural Basis for Shelterin Bridge Assembly

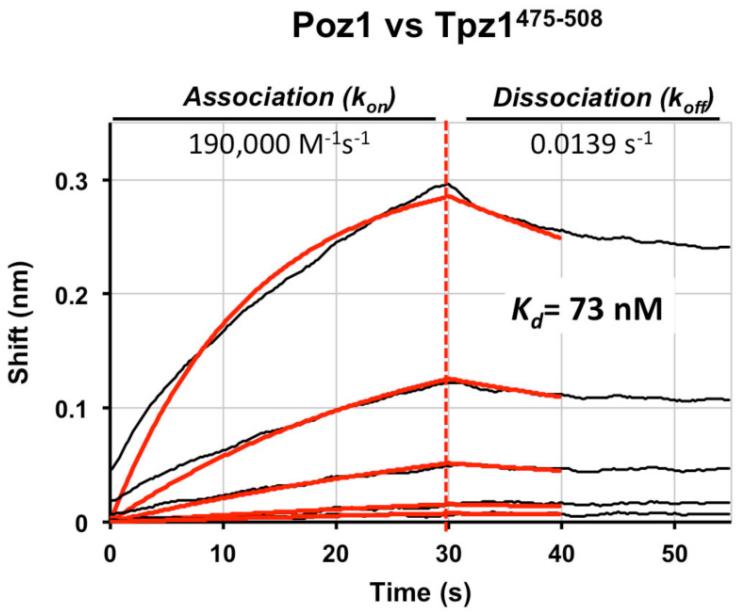

Figure S1. Measurement of the binding affinity between Poz1 and Tpz1$^{475\text{-}508}$, Related to Figure 1. Bio-Layer Interferometry (BLI) sensorgrams monitoring dissociation and association events in real time between Poz1 andTpz1$^{475\text{-}508}$ using Octet Red96 (R2=0.9938). BLI experiments were repeated twice and representative results were shown.

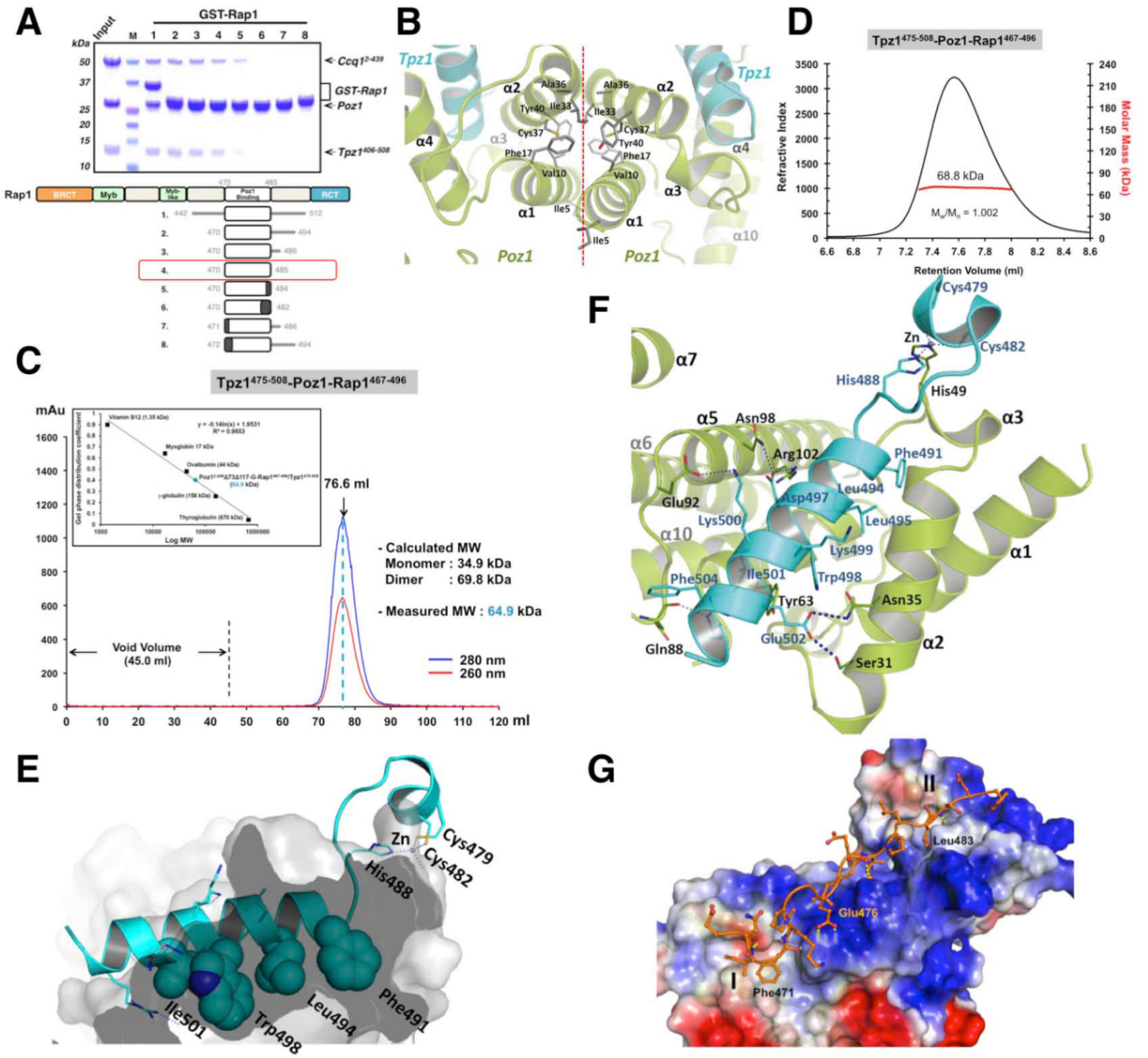

Figure S2. Characterization of Tpz1$^{475-508}$-Poz1-Rap1$^{467-496}$ complex and interfaces, Related to Figure 2.
(A) In vitro GST pull-down assays identifying the minimal Rap1 region for Poz1 interaction. Top: Poz1-Tpz1406-508-Ccq12-439 complex is used to incubate with different GST-Rap1 constructs. Rap1470-485 (#4) is the minimal construct to maintain the wild-type level Poz1-Rap1 interaction. Bottom: Domain organization of full length Rap1 and all tested Rap1 constructs. Rap1470-485 (minimal construct) is highlighted in red square. **(B)** Close-up view of the Tpz1475-508-Poz1-Rap1467-496 dimerization interface. Hydrophobic core residues that comprise the interface are labeled. **(C)** Gel filtration chromatography showing Tpz1475-508-Poz1-Rap1467-496 complex forms a dimer of the heterotrimer. Elution volume is labeled on the top of elute peak. Insert is the plot of calibration curve and the blue dot represents molecular weight determination of Tpz1475-508-Poz1-Rap1467-496 complex, which is 64.9 kDa. **(D)** SEC-MALS measurement showing Tpz1475-508-Poz1-Rap1467-496 complex has molecular mass of 68.8 kDa in solution, indicating the formation of a dimer of the heterotrimer.
See next page for rest legend.

Figure S2. Characterization of Tpz1$^{475-508}$-Poz1-Rap1$^{467-496}$ complex and interfaces, Related to Figure 2. **(E)** Overall view of the "key teeth", four hydrophobic residues of Tpz1 (Phe491, Leu494, Trp498 and Ile501 represented by cyan spheres on α-helix) inserted into Poz1 (grey surface). **(F)** Close-up views of salt bridges formed at the Tpz1-Poz1 interface. The salt bridges are shown as dashed lines between Glu502 in Tpz1 and Ser31, Asn35 in Poz1 (front side); Asp497 in Tpz1 and Asn98, Arg102 in Poz1; Lys500 in Tpz1 and Glu92 in Poz1; Arg505 in Tpz1 and Tyr63, Gln88 in Poz1. **(G)** Surface representation of the structure of Poz1-Rap1 interface. The representation was colored by surface electrostatic potential. The positively charged surface is in blue, and the negatively charged surface is in red. Two hydrophobic cores are labeled I and II, respectively. H-bonds between Rap1 and the positively charged surface on Poz1 are shown as dotted lines.

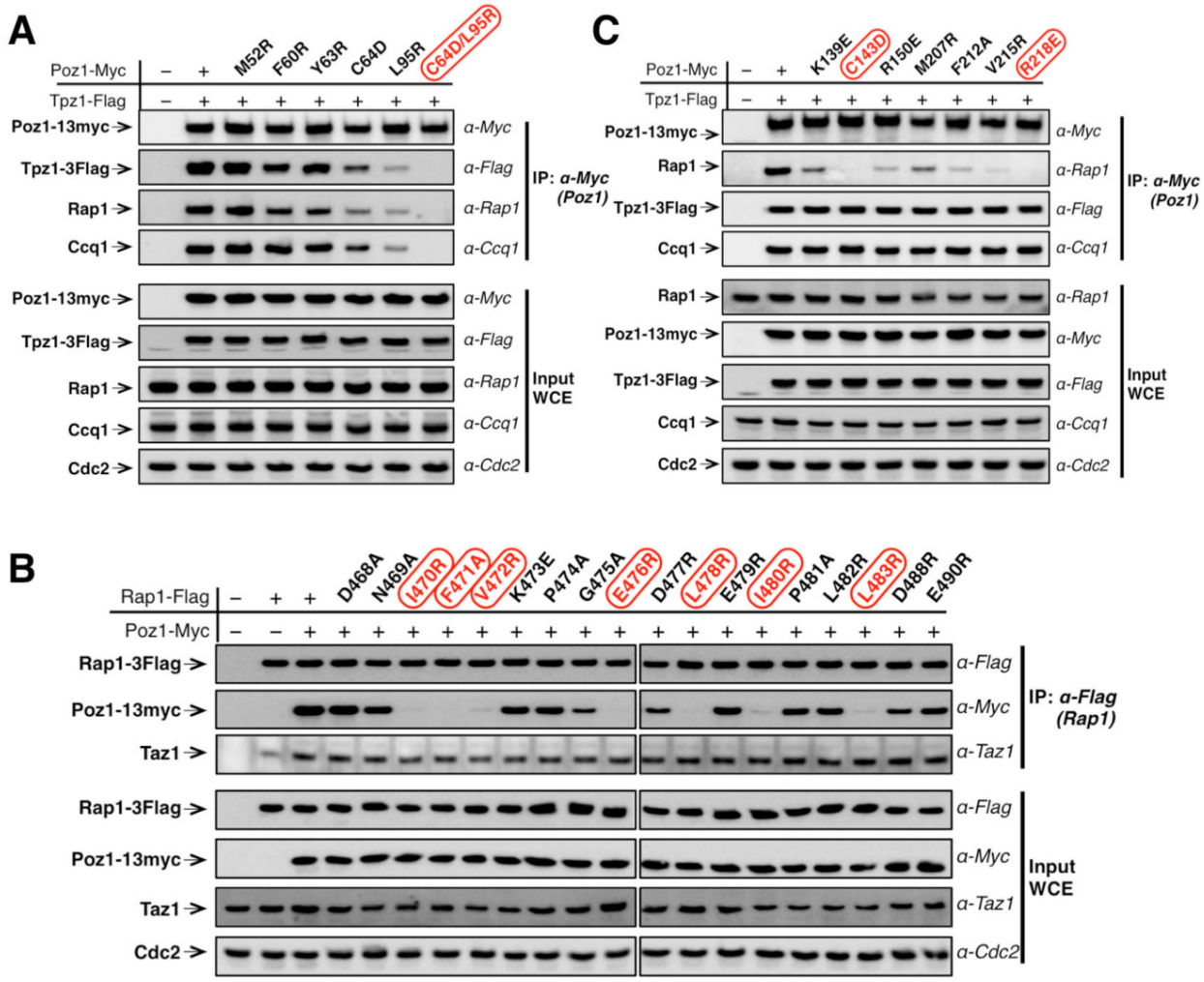

Figure S3. Mutations in interfaces of Tpz1-Poz1-Rap1 complex disrupt protein interactions in vivo, Related to Figure 3. (A) Co-immunoprecipitation (Co-IP) assay evaluating Poz1-Tpz1 interaction in indicated poz1 mutants. The binding between Poz1 mutants with Rap1 and Ccq1, respectively, are also tested. The same as the *in vitro* GST-pulldown assay, the double mutants poz1-C64D/L95R is defective in Poz1-Tpz1 binding, and consequently, Poz1-Rap1 binding (promoted by Tpz1-Poz1 interaction) and Poz1-Ccq1 binding (bridged by Tpz1) are also disrupted. Cdc2 was shown as the loading control. The binding defective mutants are colored and circled in red. Input: 1/30 of input WCE (whole-cell extract). **(B)** and **(C)** Co-IP assays evaluating the effect of Poz1-Rap1 interface mutants on the binding between Poz1 and Rap1 in vivo. Rap1-Poz1 interface mutations in both Rap1 (B) and Poz1 (C) are tested. The Rap1-Poz1 binding defective mutants are colored and circled in red. Rap1-Taz1 interaction (B) or Poz1-Tpz1, Poz1-Ccq1 (C) interactions are also tested, which all remain at the wild type level.

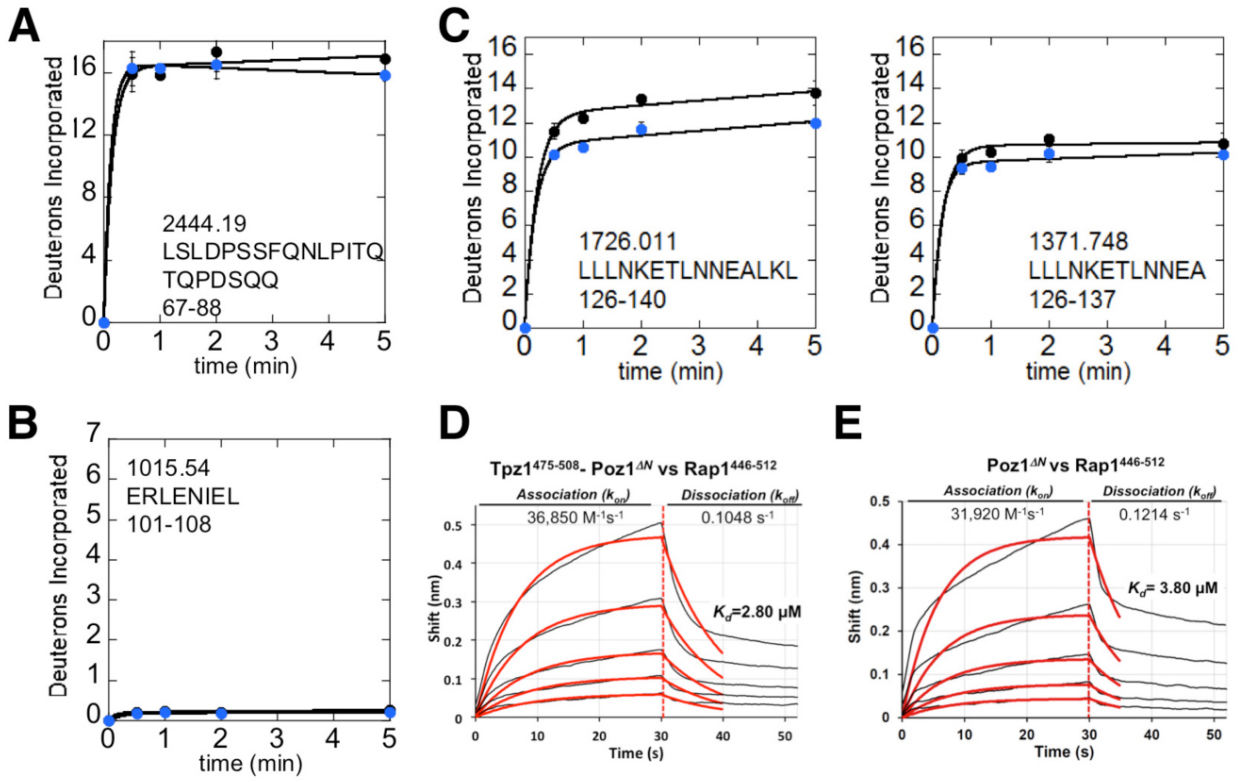

Figure S4. Tpz1 binding induces the folding of the N-terminal helix α1 of Poz1, Related to Figure 4. (A) and **(B)** Amide hydrogen-deuterium exchange in Poz1 with and without the presence of Tpz1. The graphical data of deuterium incorporation in Poz1 show that some regions of Poz1 exchanges nearly all of its amides (A), and then a few regions that exchange very little of its amides (B). **(C)** Amide hydrogen-deuterium exchange in Poz1 with and without Tpz1. The graphical data of deuterium incorporation in Poz1 show differences between free Poz1 (Black dot) and Tpz1-bound Poz1 (Blue dot). The results strongly point to the 138-140 region as being a site of strong protection upon Tpz1 binding, because the 126-137 region is not much protected but the 126-140 is, so the protection must be in the last few additional amino acids (138-140: Region IV in Figures 4B and 4C). Error bars indicate standard deviation (n = 3). **(D)** and **(E)** Bio-Layer Interferometry (BLI) sensorgrams monitoring dissociation and association events in real time between Rap1 with $Poz1^{\Delta N}$ (R2=0.9803) (A) or $Tpz1^{475\text{-}508}$-$Poz1^{\Delta N}$ complex (R2=0.9890) (B) using Octet red96. Compared with full length Poz1, $Poz1^{\Delta N}$ loses its enhanced interaction with Rap1 upon its Tpz1 binding. BLI experiments were repeated twice and representative results were shown.

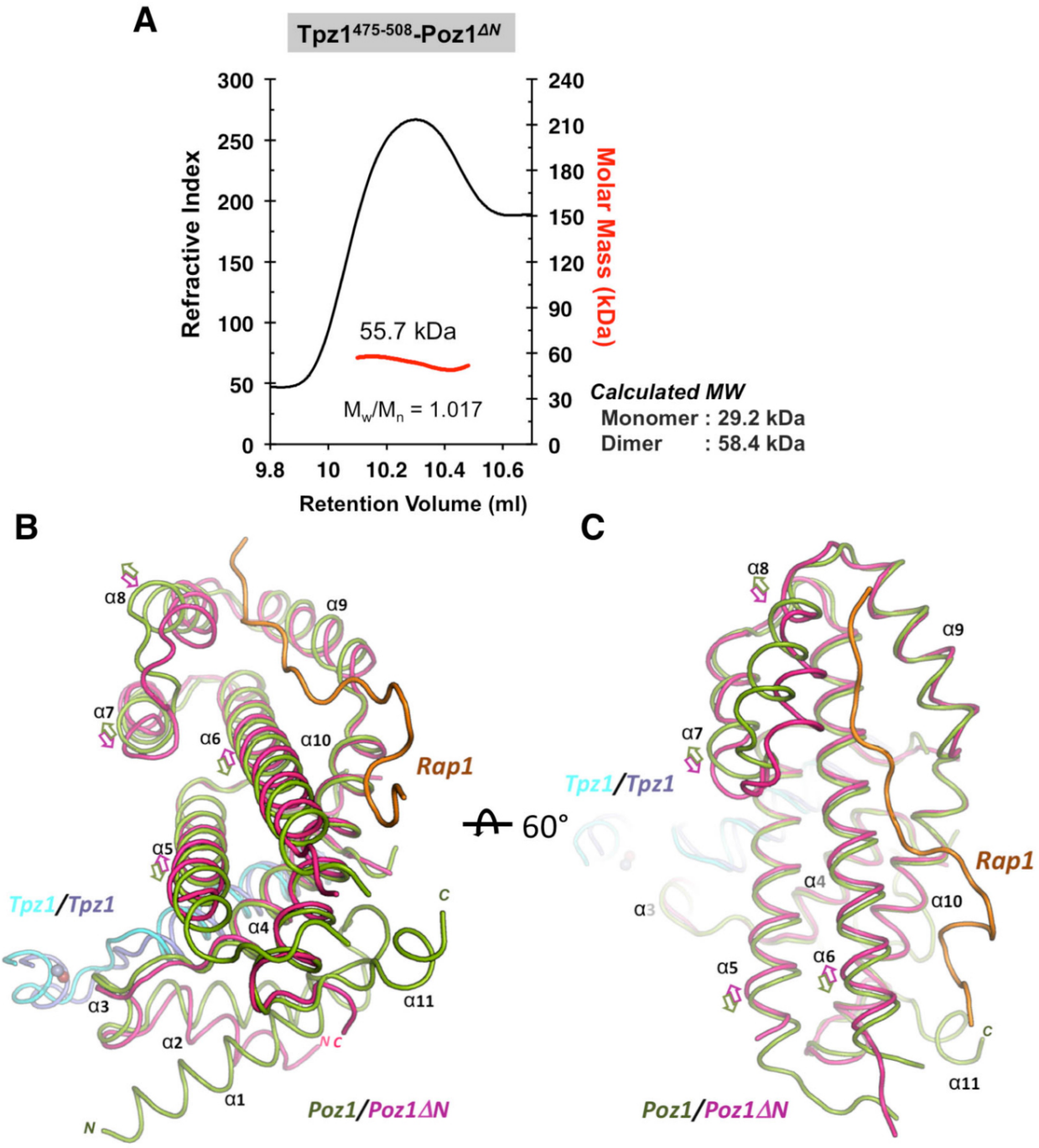

Figure S5. Characterization of Tpz1-Poz1*ΔN* complex and its structural comparison to Tpz1- Poz1 complex, Related to Figure 5. **(A)** SEC-MALS measurement showing Tpz1$^{475\text{-}508}$-Poz1$^{\Delta N}$ complex has molecular mass of 55.7 kDa in solution, indicating the formation of a dimer of Tpz1$^{475\text{-}508}$-Poz1$^{\Delta N}$ heterodimer. **(B)** and **(C)** Two close-up views of the structural changes in the Rap1 binding site of Poz1. Allosteric structural changes induced by Tpz1-binding to Poz1 result in a more open binding groove for Rap1. The arrows indicate the directions of helix movements due to the structural changes.

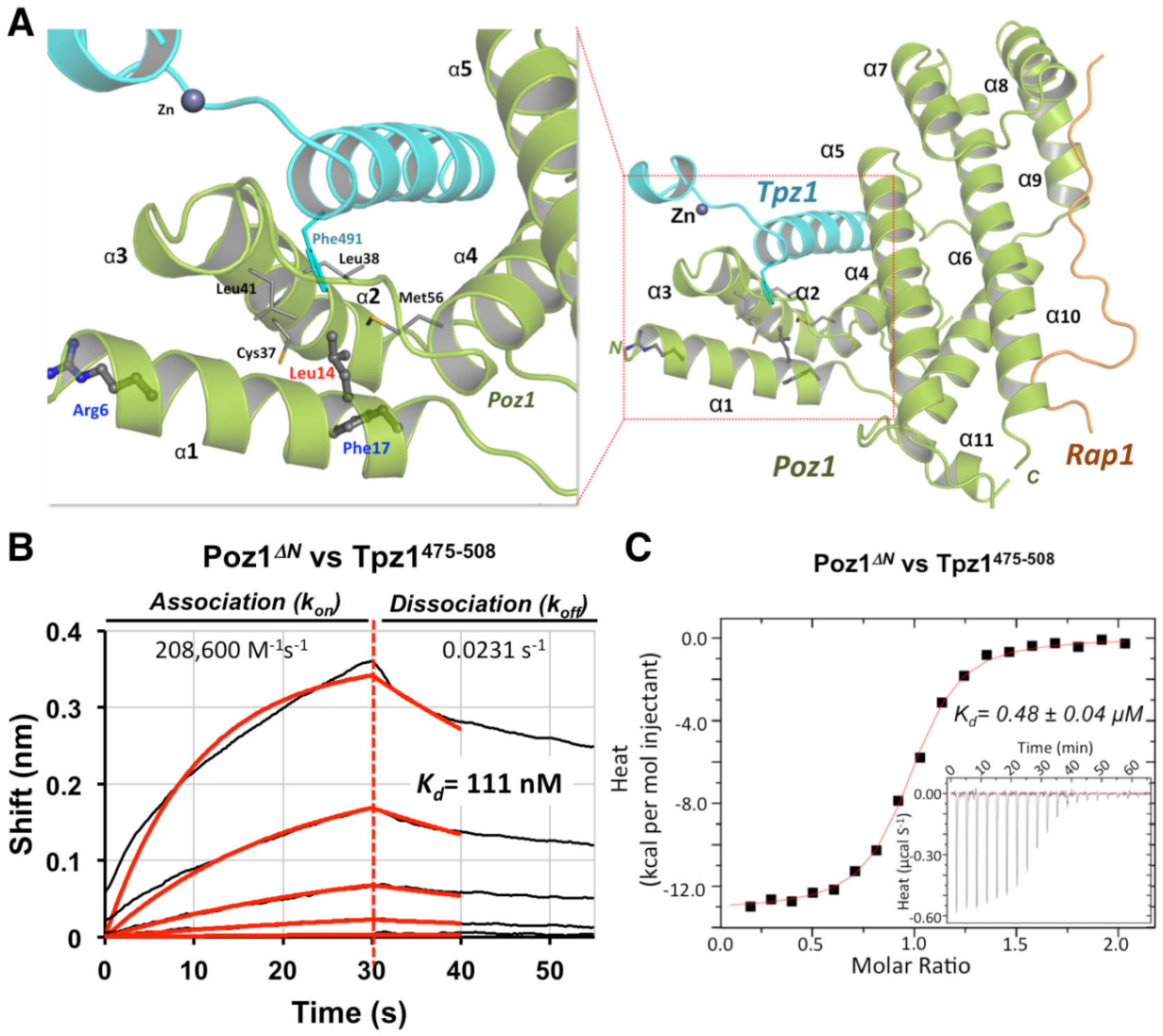

Figure S6. The "conformational trigger" N-terminal helix α1 in Poz1 is not important for Tpz1-Poz1 interaction, Related to Figure 6. (A) Close-up view of the potential allosteric pathway delivering structural changes from Tpz1-Poz1 binding site to the Rap1-binding region of Poz1 through Leu14 (colored in red). Leu14 from α1 has hydrophobic interactions with Cys37, Leu38 and Leu41 from α2, Met56 from α4, as well as Phe491 in Tpz1. Another two Poz1 residues, Arg6 and Phe17 (colored in blue), are not packed against α2, and therefore have no effect on Poz1-Rap1 interaction (as shown in Figure 6C). **(B)** Bio-Layer Interferometry (BLI) sensorgrams monitoring dissociation and association events in real time between $Poz1^{\Delta N}$ and $Tpz1^{475-508}$ using Octet red96 (R2=0.9934) are similar to those of Poz1-$Tpz1^{475-508}$ interaction. BLI experiments were repeated twice and representative results were shown. **(C)** ITC measurements of interactions between $Poz1^{\Delta N}$ and $Tpz1^{475-508}$. Error bar represent standard deviations calculated from the fit. ITC experiments were repeated twice and representative results were shown.

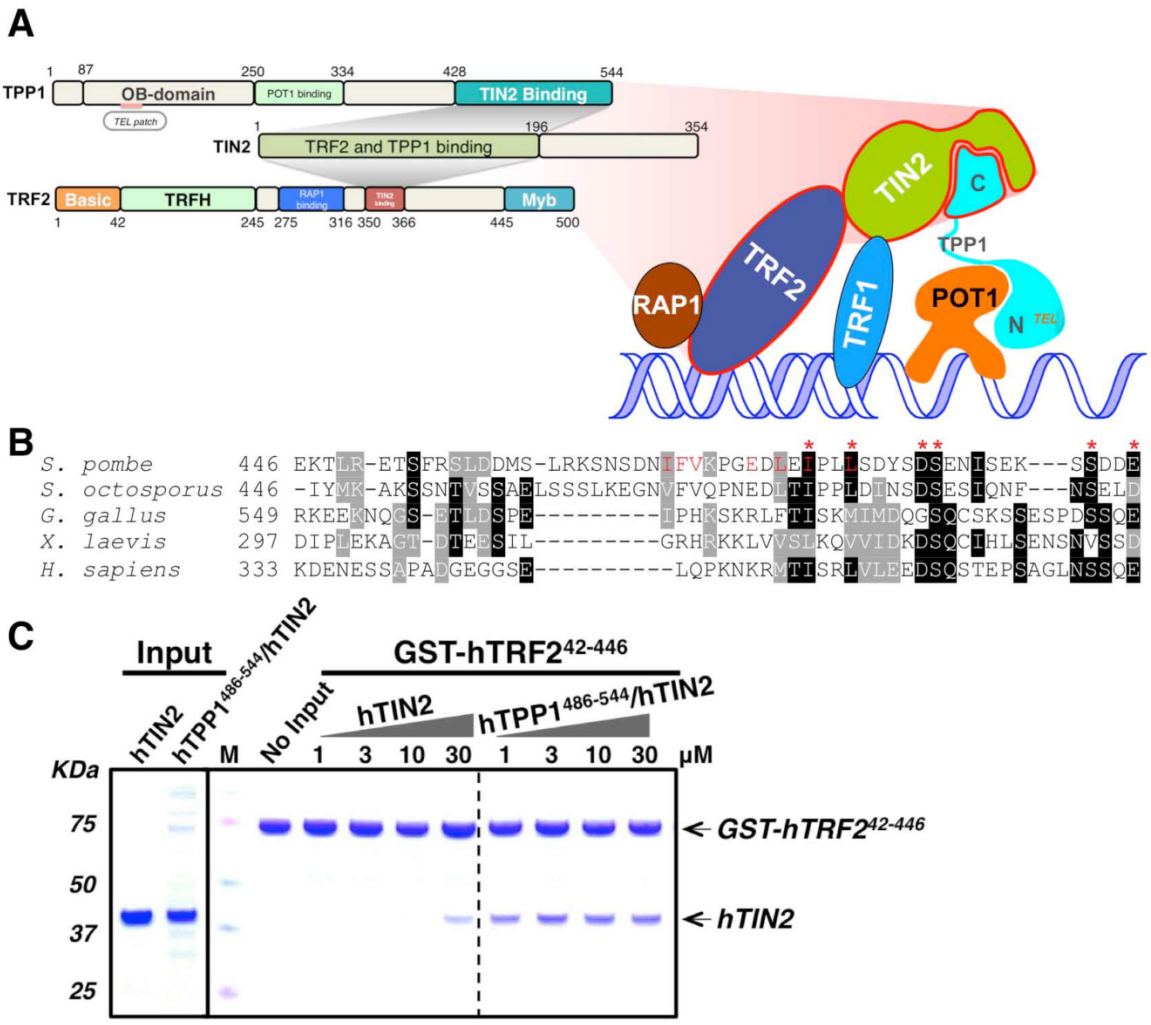

Figure S7. Cooperativity assembly is conserved in human shelterin, Related to Figure 7. (A) Schematic diagram of human TPP1-TIN2-TRF2 interaction (left) in the setting of overall shelterin complex on the telomere (right). Right: Overview of human shelterin complex. Similar to *S. pombe* shelterin, a shelterin bridge composed of TIN2 and TPP1 connects double-stranded telomeric DNA binding protein TRF1/TRF2 and single-stranded DNA binding protein POT1 by direct protein-protein interaction. The difference is that human RAP1 is not part of shelterin bridge. For clarity, the stoichiometry of each individual component is not indicated in the figure; only one copy of each component is shown. Left: Domain organization of shelterin components TPP1, TIN2, and TRF2. TIN2 interacts simultaneously with the C-terminal domain of TPP1 and a middle domain of TRF2. **(B)** Sequence alignment of the Poz1-binding domain from fission yeast Rap1 (top two lines) and the TIN2-binding domain from vertebrate TRF2 (bottom three lines) shows sequence conservation. Highly conserved residues are highlighted in black, and similar residues are highlighted in gray. The key Rap1-Poz1 interface residues in *S. pombe* Rap1 are colored in red and the conserved interface residues between *H. sapiens* TRF2 and *S. pombe* Rap1 are labeled with red asterisks. **(C)** In vitro GST pull-down assays examining TIN2-TRF2$^{42-446}$ and TPP1$^{486-544}$-TIN2 complex-TRF2$^{42-446}$ interactions. TPP1$^{486-544}$ promotes strong TIN2-TRF2$^{42-446}$ interaction (right side of the dashed line).

CHAPTER 6: Recognition of budding yeast telomerase RNA by TERT and its role in template boundary definition

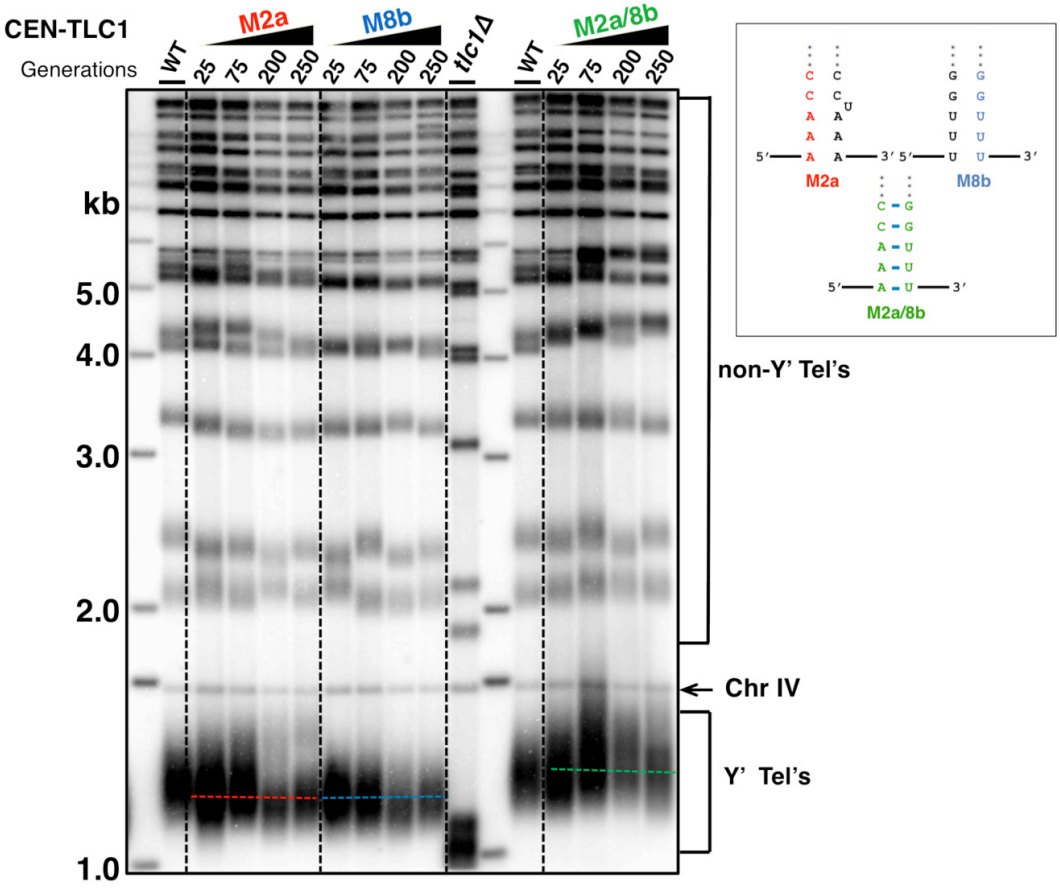

Figure S1. Functional dissection of TLC1-Est2_RBD interface. Related to Figure 3.

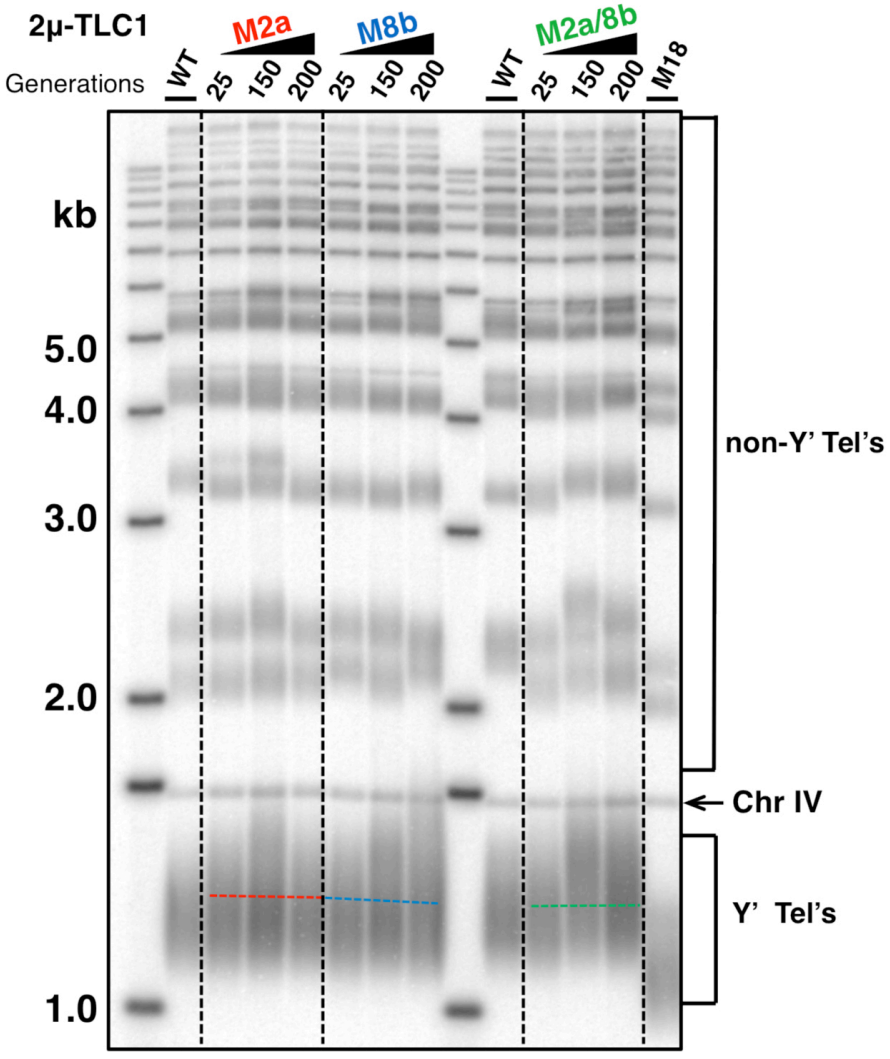

Figure S2. TLC1-Est2p interface mutants show less dominant negative effect. Related to figure 4.